VILNIUS UNIVERSITY
AND
CENTER FOR PHYSICAL SCIENCES AND
TECHNOLOGY

Donatas Majus

TRANSIENT PHENOMENA IN FEMTOSECOND FILAMENTATION

Doctoral dissertation
Physical sciences, physics (02P)

Vilnius, 2014

The research was performed in 2010-2014 at Vilnius University.

Scientific supervisor:
prof. habil. dr. Audrius Dubietis (Vilnius university, physical sciences, physics - 02P)

VILNIAUS UNIVERSITETAS
IR
FIZINIŲ IR TECHNOLOGIJOS MOKSLŲ CENTRAS

Donatas Majus

DINAMINIAI REIŠKINIAI FEMTOSEKUNDINĖSE ŠVIESOS GIJOSE

Daktaro disertacija
Fiziniai mokslai, fizika (02P)

Vilnius, 2014

Disertacija rengta 2010–2014 metais Vilniaus Universitete.

Mokslinis vadovas:
prof. habil. dr. Audrius Dubietis (Vilniaus universitetas, fiziniai mokslai, fizika - 02P)

Contents

List of symbols and abbreviations **3**

Introduction **4**

1 Ultrashort laser pulses in dielectric media: theoretical model, numerical simulations and experimental techniques **21**

1.1 Unidirectional pulse propagation equation 21

1.2 Simplified model and results of numerical simulations 26

1.2.1 Moving focus model for ultrashort pulses 27

1.2.2 Pulse splitting 28

1.2.3 Modified Marburger's law 30

1.2.4 Conclusion 32

1.3 Three-dimensional imaging of complex wave-packets 32

2 Filamentation dynamics in normal and anomalous GVD regime **36**

2.1 Evolution cycle of femtosecond filaments in the UV 37

2.1.1 Experimental setup 38

2.1.2 Dynamical spatial replenishment of the UV filaments 40

2.1.3 Numerical simulations 43

2.1.4 Measurements for tighter focusing conditions 48

2.1.5 Conclusions 49

2.2 Light bullets by the filamentation in the anomalous GVD regime 50

2.2.1 Experimental setup 51

2.2.2 Light bullets as polychromatic Bessel-like beams . . . 52

2.2.3 Conclusion 58

3 Supercontinuum generation **60**

3.1 Extreme-value statistics in ultrafast white-light continuum generation 63

3.1.1 Experimental setup 63

3.1.2 Main results and discussion 65
3.1.3 Conclusion 69
3.2 Spatio-temporal rogue events: rogue X-waves 70
3.2.1 Experimental setup 70
3.2.2 Main results 70
3.2.3 Numerical simulations 72
3.2.4 Discussion 72
3.2.5 Conclusions 76
3.3 Statistical properties of ultrafast supercontinuum 76
3.3.1 Experimental setup 77
3.3.2 Comparative study of supercontinuum generated by femtosecond Bessel and Gaussian beams 79
3.3.3 Conclusions 87
3.4 Infrared extension of NIR pumped supercontinuum 88
3.4.1 Supercontinuum generation in sapphire with variable focusing conditions 89
3.4.2 Numerical simulations 91
3.4.3 Conclusions 95

4 Filamentation of highly elliptical laser beams 98
4.1 Generation of periodic multifilament arrays 100
4.1.1 Experimental results 100
4.1.2 Numerical simulations of the multiple filamentation dynamics 102
4.1.3 Multistep four-wave mixing model 106
4.1.4 Discussion and conclusions 109
4.2 Spatiotemporal structure of multiple filament arrays 111
4.2.1 Experimental setup 111
4.2.2 Numerical model 112
4.2.3 Results and discussion 114
4.2.4 Conclusions 120

Main results and conclusions 122

Acknowledgments 125

Bibliography 126

List of symbols and abbreviations

FWHM	Full width at half maximum
FWM	Four-wave mixing
FS	Fused silica
GVD	Group velocity dispersion
MF	Multiple filaments
MIR	Middle infrared
MPA	Multiphoton absorption
NIR	Near infrared
NOPA	Noncollinear optical parametric amplifier
SC	Supercontinuum
SPM	Self-phase modulation
UV	Ultraviolet
WLC	White light continuum

Introduction

In 1995 Braun and co-workers reported the observation of self-channeling of femtosecond laser pulses over 20 m in air [1]. The observation was startling in virtue also of the amazing simplicity of the experimental setup: the input laser beam was simply collimated and allowed to propagate in free space. As the energy was increased, the beam was seen to shrink until it reached a minimum diameter of the order of 100 μm which was then maintained over many meters of propagation. Moreover, an array of beautiful colours, or conical emission, was observed that clearly indicated a rather dramatic modification of the pulse shape. This first observation of femtosecond filament triggered a series of studies, which discovered an exciting physics beyond the interaction of ultrashort laser pulses with transparent dielectric media [2–5]. Currently, there are many research groups world-wide involved in the investigation of the properties and applications of femtosecond filamentation phenomena.

Curiously, it is not easy to provide a clear-cut definition of an optical filament and one usually refers to the associated phenomena in order to define it. For example, in many experiments in gases, the filament is defined as a high-intensity peak propagating over many Rayleigh ranges without apparent diffraction spreading. **Its length may be defined as the distance over which nitrogen fluorescence (excited by multiphoton absorption from the high intensity peak) appears**. In solids and liquids a much more obvious manifestation of filament formation is the generation of colored conical emission (i.e. a strong spectral broadening with different wavelengths emitted at different angles) and supercontinuum radiation. These features either are a manifestation of a narrow high intensity peak propagating over many Rayleigh lengths. A modern definition of the filament could be formulated as in Couairon et al., [3]:

a filament is a ***dynamic*** *optical pulse structure with an intense core that*

is able to propagate over extended distances much larger than the typical diffraction length while keeping a narrow beam size without the help of any external guiding mechanism

Note the highlighted "dynamic". It is generally acknowledged that the filament is not the result of the propagation of a stationary soliton-like structure. The filament will therefore appear as a dynamic competition between self-focusing and some saturating or defocusing mechanism. This may eventually involve successive focusing and defocusing cycles that give the overall impression of a stationary-like propagation, but it is actually far more complex. Figure 1 gives a schematic representation of the evolution of the laser beam diameter as it first self-focuses, reaches a nonlinear focus and forms a filament. This initial stage is a result of the nonlinear Kerr effect: at high intensities the medium in which the laser beam is propagating, responds nonlinearly and a self-induced phase shift is imparted on the beam. The value of the phase shift depends on the local intensity and will thus be higher at the center of the beam and lower at the edges. This therefore acts like a lens which enforces the beam to self-focus. The self-focusing stage is theoretically a runaway effect in the sense that as the beam self-focuses, the intensity increases and so does the self-focusing effect. However, the beam cannot and will not contract to a singularity, but self-focusing is arrested by some higher order effect (e.g. nonlinear losses or self-created plasma defocusing). The filament that emerges from the nonlinear focus may then be characterized by one or more refocusing stages (two are shown in the figure for simplicity). During propagation the filament will continuously lose energy due to multiphoton and plasma absorption until it dies out and a linear diffraction regime is resumed.

From an experimental point of view, filamentation may manifest itself in many different ways. The interesting point is that these features appear to be common to all transparent media, input pulse wavelengths and durations (within the ultrashort pulse regime).

The nonlinear focus. Spatial self-action leads to focusing distance even for a collimated beam. In order for this to occur the beam should have a power

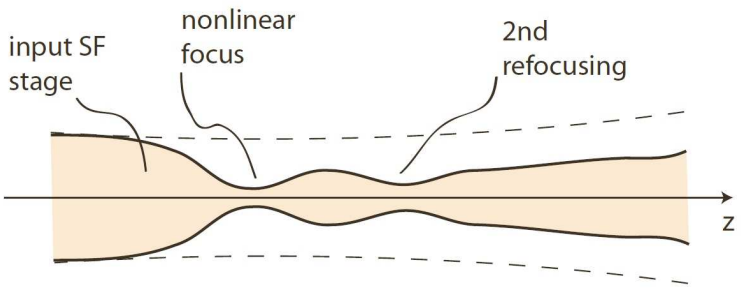

Figure 1: Schematic representation of how the transverse dimension of the laser beam varies in the linear regime (dashed line) compared to the nonlinear regime when the input power is above the critical power for self-focusing.

that is larger than a critical power defined as [6]

$$P_{\rm cr} = 3.77 \frac{\lambda^2}{8\pi n_0 n_2} \,, \tag{1}$$

where λ is laser wavelength, n_0 and n_2 are linear and nonlinear refractive indexes of the medium, respectively. A collimated beam with power $P_{\rm in} > P_{\rm cr}$ will focus (due to the nonlinearity) at a distance given by [6]

$$z_c = \frac{0.367 z_R}{\sqrt{[(P_{\rm in}/P_{\rm cr})^{1/2} - 0.852]^2 - 0.0219}} \,, \tag{2}$$

where $z_{\rm R}$ is the beam Rayleigh range.

White-light or supercontinuum (SC) emission. Filamentation is associated with generation of an extremely broadband, spatially and temporally coherent light emission with a low angular divergence. The SC radiation emerges from a complex interplay between self-focusing, self-phase modulation, four-wave mixing, multiphoton absorption and plasma generation. The width of the SC spectrum strongly depends on the linear and nonlinear optical properties of the medium and the pump wavelength [7] and may span over more than several octaves with mid-infrared pumping [8, 9]. SC emission is widely exploited in ultrafast spectroscopy and serves as a primary seeding source for broadly tunable optical parametric amplifiers.

Conical emission (CE). Broadband emission is observed also at angles with respect to the propagation axis. The emission angles are set by the dispersive properties of the medium and represent the Kerr-driven spatiotemporal

instability gain profile: the CE angles increase (or decrease) with the frequency shift with respect to the pump frequency, depending on the sign of the group velocity dispersion [10]. The shape of the CE pattern is a distinctive feature related to the spontaneous formation of the X-waves and O-waves in media with normal and anomalous group velocity dispersion, respectively.

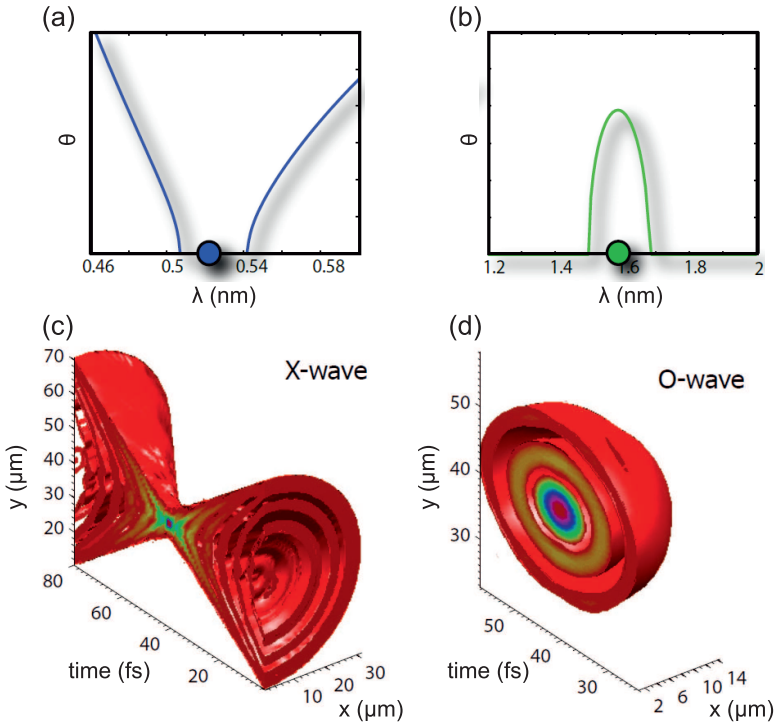

Figure 2: (a) and (b) are $\theta(\lambda)$, angular spectra support for the X- and O- type waves respectively, evaluated for propagation in water. (c) and (d) are the spatio-temporal intensity distribution corresponding to a wave with spectral support of (a) and (b) respectively. Image from [11].

Pulse splitting and temporal compression. During filament formation in the normally dispersive medium (normal group velocity dispersion regime), the pulse splits and the sub-pulses may be further temporally compressed [12]. The energy balance between the two sub-pulses may favor one or the other or a possible strong unbalance may arise due to propagation effects such as absorption of the trailing pulse due to the self-generated plasma from the leading pulse. This can lead to the isolation and survival of a single, temporally compressed, intense pulse [13]. In the media with anomalous group velocity dispersion, the entire input wave packet undergoes simultaneous compression in space and time, producing quasi-stable three-dimensional nonspreading pulses – light bullets [14]. Filamentation may therefore be

considered as a potential novel laser pulse compression technique and single cycle durations may be achieved.

Intensity clamping. The peak intensity of the input pulse may increase by some orders of magnitude during the filamentation process. The final peak intensity actually reached will depend on the material characteristics. In gaseous media, for which peak intensities of the order of hundreds of TW/cm^2 have been reported, the main limiting mechanism is related to self-generated plasma defocusing [15]. In solid or liquid media the role of plasma defocusing is usually somewhat reduced, maximum intensities up to tens of TW/cm^2 are estimated [16] and the main limiting mechanisms are related to multiphoton absorption, group velocity dispersion and beam break-up into multiple filaments. In any case it has been shown that in both gaseous and condensed media the filament reaches a maximum "clamped" intensity level.

Spatial robustness. The intensity peak associated to the central core of the filament is highly localized in space. Typical filament diameters are of the order of 100 μm in air and 10–40 μm in condensed media. However, this tightly localized peak is surrounded by a large background that acts as an energy reservoir continuously refueling the central hot core [17, 18]. This feature is at the basis of the filament robustness to spatial perturbations so that filaments may, for example, survive propagation through scattering media, such as fog and clouds [19–21]. This property is directly related to the conical (Bessel-like) nature of the filament. For example, Bessel beams are well known to exhibit the same kind of robustness and the ability to reconstruct their original profile after passing through an obstacle.

Light filaments as nonlinear X waves. X-waves, so-called due their evident "X" shape in both the near and the far-field (Fig. 2), are a specific example of conical waves that are stationary in the normal group velocity dispersion regime [22]. A very convenient description of the X waves could be given in the transverse-space and temporal Fourier domain, i.e. as a function of frequency ω and transverse wave-vector, $k_\perp = \sqrt{k^2(\omega) - k_z^2(\omega)}$ where stationarity is imposed by taking the longitudinal wave-vector k_z to be linear function of frequency,

$$k_z = k_0 + \frac{\omega - \omega_0}{v} \tag{3}$$

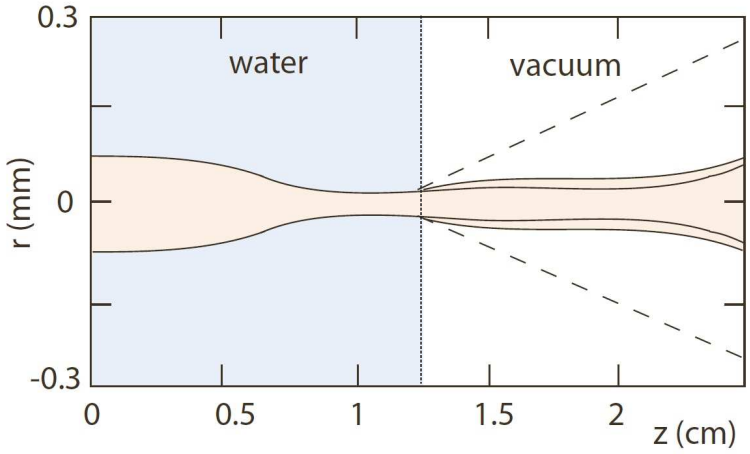

Figure 3: Numerical simulation of a filament that is formed in water but passes into vacuum at $z = 1.25$ cm. The filament continues to propagate even in the absence of nonlinearity with a diameter that is only slightly larger (outer profile) than that of the filament in the fully nonlinear regime, i.e. in water for the whole propagation distance (inner profile). The dashed lines show the expected diffraction evolution for a linear Gaussian-shaped beam.

where ω_0 is a reference frequency, e.g. the input pulse carrier frequency, $k_0 = k(\omega_0)$ and v is the group velocity along the propagation z-axis of the conical pulse. Experiments proving spatial robustness of the filament are interpreted by assuming that the filament is actually a conical wave so that the central intense peak results from an interference effect, continuously refilled by a large yet low-intensity surrounding energy reservoir [17, 18]. The same results were later reproduced also for filaments propagating in air [23]. Finally, numerical simulations by Kolesik et al. and experiments by Faccio et al., clearly proved that filamentation in condensed media may be interpreted as a dynamical interaction between X-waves that form spontaneously within the filament [24, 25].

Sub-diffractive propagation. The distinctive feature of conical waves is the energy flux that occurs along a conical surface and that leads to stationary propagation, i.e. they are characterized by a central intense peak that propagates without diffraction and without dispersion. As noted above, sub-diffractive and sub-dispersive propagation are probably the most notable features of laser pulse filaments: these are both directly related to the stationary properties of polychromatic conical wave-packets. A remarkable demonstration of this can be given by numerically simulating the propagation of a filament in free space. If the filament pulse enters vacuum, the beam continues to propagate nearly exactly as it would have done in the

presence of the nonlinear medium, i.e. it continues to propagate without diffraction over nearly the same distance. This behavior has been numerically verified both in condensed media and in air [26, 27] and an example is shown for the case of a filament passing from water to vacuum in Figure 3. Clearly the filament must be characterized by some kind of stationary or nearly stationary state and the conclusion is rather simple. The only wavepackets that are stationary in both the linear and nonlinear regime, both with and without dispersion, are conical waves. The sub-diffractive propagation of the filament is indeed therefore a very strong indication of the spontaneous formation of X-waves.

These features are natural consequences of the fact that the filament is composed of conical waves and they render femtosecond filaments extremely attractive for numerous practical applications in many fields of photonics, nonlinear optics and material processing, such as atmospheric analysis, remote sensing of pollutants and lightning control [28, 29], structural modifications of transparent solids [30], laser micromachining [31], supercontinuum generation and pulse compression to a few or even single optical-cycle limit [32] and investigations of novel fundamental aspects of light and matter interactions, such as optical event horizons [33, 34], to mention a few. However, despite growing understanding and expanding field of applications, there still remain many open questions of fundamental and practical importance related to femtosecond filamentation in transparent dielectric media. Some of these open important issues regarding complete physical understanding of the evolution cycle of femtosecond filaments in normally dispersive media, physical nature of spatiotemporal light bullets generated by filamentation in the anomalous group velocity regime, detailed statistical aspects of supercontinuum generation, and spatiotemporal characterization of multiple filaments, are addressed in present dissertational work.

The objective of the thesis

The dissertation aims at comprehensive study of transient spatiotemporal phenomena (space-time transformations, pulse splitting and compression, filament propagation dynamics, supercontinuum generation and multiple filamentation) that take place during self-focusing of intense femtosecond laser pulses in various self-action regimes in transparent dielectric media with instantaneous Kerr nonlinearity.

The main tasks of the thesis

- Four-dimensional characterization of the evolution cycle of ultraviolet femtosecond filaments in water, in the regime of normal group velocity dispersion.
- Complete characterization of spatiotemporal light bullets generated by filamentation of mid-infrared laser pulses in sapphire, in the regime of anomalous group velocity dispersion.
- Spectral, statistical and correlation analysis of ultrafast supercontinuum generated in transparent dielectric media with near-infrared laser pulses under various operating conditions.
- Spatiotemporal characterization of multiple filament arrays, generated by self-focusing of highly elliptical laser beams in fused silica.

Practical and scientific novelty

- Evolution of ultraviolet filaments in water is captured in four dimensions (x,y,z,t) for the first time and discloses missing essential links between the relevant physical processes: focusing/defocusing cycles of the beam, pulse splitting and replenishment, supercontinuum generation, conical emission and nonlinear absorption peaks, providing a complete physical picture of filament propagation and energy deposition dynamics in a transparent medium with normal group velocity dispersion.
- By combined high dynamic range measurements of spatiotemporal intensity profiles, angularly resolved spectra, energy density flux and free space propagation, the physical nature of spatiotemporal light bullets which emerge from self-focusing of mid-infrared laser pulses in bulk dielectric medium with anomalous group velocity dispersion is disclosed. It is demonstrated that these light bullets are nonsolitonic, polychromatic Bessel-like wave packets, which bear the basic properties of the nonlinear O waves, as opposed to widely-spread solitonic interpretation of their nature.
- It is demonstrated experimentally and by the numerical simulations that fluctuations of the spectral intensity of the blue-shifted supercontinuum components, which occur in the transient stage of the super-

continuum generation obey the extreme-value (heavy-tailed) statistics and are related to optical rogue waves. It is shown that these instabilities take place in space and time simultaneously, thus leading to a discovery of a new class of optical rogue waves – rogue X waves.

- A comparative study of the supercontinuum generation with ultrashort pulsed Gaussian and Bessel beams shows that ultrastable (with RMS fluctuation less than 1%), broadband and smooth supercontinuum spectra are generated, however, in the case of the Bessel beam, 10 times larger input energy is required. A peculiar development of stability and instability regions of the supercontinuum spectral intensity is discovered, which is associated with four-wave mixing-induced spectral broadening and distinct correlations of intensity fluctuations at certain wavelengths.
- Detailed experimental investigation of the supercontinuum generation in sapphire with femtosecond near infrared pulses is carried out under variable focusing conditions, which reveals that loose focusing results in strongly enhanced red-shifted spectral broadening, as due to extended nonlinear propagation of the leading sub-pulse, which preserves a steep ascending front, as verified by the numerical simulations.
- Generation of reproducible periodic one- and two-dimensional filament arrays is demonstrated by self-focusing of highly elliptical laser beams in fused silica. It is shown that the filaments are distributed along the long axis of an ellipse and their spacing could be easily varied by changing the input energy. Measurements of the spatiotemporal intensity distributions disclose a complex spatiotemporal dynamics of the individual filaments such as formation of extremely short (<5 fs) pulses at the leading edge and curved propagation paths, despite apparently regular intensity pattern observed in space.

Statements to defend

- In the regime of normal group velocity dispersion, recurrent self-focusing and defocusing cycles of a filament are unambiguously linked with temporal pulse splitting and replenishment, respectively.
- Self-focusing of ultrashort pulsed laser beams in media with anomalous group velocity dispersion leads to formation of weakly localized

spatiotemporal light bullets, which are polychromatic Bessel beams and bear the basic features of the nonlinear O waves.

- Intensity fluctuations of the blue-shifted spectral components in the supercontinuum spectra obey extreme value statistics, which are due to formation of rogue X waves.
- Gaussian and Bessel ultrashort pulsed beams undergo very similar self-focusing dynamics, leading to generation of ultrastable, broadband and spectrally smooth supercontinuum.
- By choosing loose focusing conditions, it is possible to achieve a marked enhancement of the red-shifted spectral broadening of the supercontinuum generated in a dielectric media with near infrared laser pulses.
- Self-focusing of highly elliptical beams leads to generation of regular and reproducible one- and two dimensional filament arrays.

Approbation

Scientific papers related to the topic of this thesis

[A1] **D. Majus**, V. Jukna, G. Valiulis, and A. Dubietis, Generation of periodic filament arrays by self-focusing of highly elliptical ultrashort pulsed laser beams, Phys. Rev. A **79**, 033843 (2009).

[A2] **D. Majus**, V. Jukna, G. Tamošauskas, G. Valiulis, and A. Dubietis, Three-dimensional mapping of multiple filament arrays, Phys. Rev. A **81**, 043811 (2010).

[A3] **D. Majus**, V. Jukna, G. Valiulis, D. Faccio, and A. Dubietis, Spatio-temporal Rogue Events in Femtosecond Filamentation, Phys. Rev. A **83**, 025802 (2011).

[A4] **D. Majus**, V. Jukna, E. Pileckis, G. Valiulis, and A. Dubietis, Rogue-wave-like statistics in ultrafast white-light continuum generation in sapphire, Opt. Express **19**, 16317 – 16323 (2011).

[A5] A. Couairon, E. Brambilla, T. Corti, **D. Majus**, O. de J. Ramírez-Gongora, and M. Kolesik, Practitioner's guide to laser pulse propagation models and simulation, Eur. Phys. J. Special Topics **199**, 5 – 76 (2011).

[A6] **D. Majus** and A. Dubietis, Statistical properties of ultrafast supercontinuum generated by femtosecond Gaussian and Bessel beams: a comparative study, J. Opt. Soc. Am. B **30**, 994 – 999 (2013).

[A7] V. Jukna, J. Galinis, G. Tamošauskas, **D. Majus**, and A. Dubietis, Infrared extension of femtosecond supercontinuum generated by filamentation in solid-state media, accepted to Appl. Phys. B., DOI 10.1007/s00340-013-5723-8.

[A8] A. Jarnac, G. Tamosauskas, **D. Majus**, A. Houard, A. Mysyrowicz, A. Couairon, and A. Dubietis, Whole life cycle of femtosecond ultravioled filaments in water, Phys. Rev. A **89**, 033809 (2014).

[A9] **D. Majus**, G. Tamošauskas, I. Gražulevičiūtė, N. Garejev, A. Lotti, A. Couairon, D. Faccio, and A. Dubietis, Nature of Spatiotemporal Light Bullets in Bulk Kerr Media, Phys. Rev. Lett. **112**, 193901 (2014).

Other scientific papers

[A10] P. Bogdanovich, **D. Majus**, and T. Pakhomova, Investigation of accuracy of configuration interaction for the oxygen isoelectronic sequence, Phys. Scr. **74**, 558–562 (2006).

[A11] V. Kudriasov, **D. Majus**, V. Sirutkaitis, S. A. Slattery, and D. N. Nikogosyan, Comparative study of UV absorption changes induced in germanosilicate glass by high-intensity femtosecond pulses at 267, 400 and 800 nm, Opt. Commun. **271**, 408–412 (2007).

[A12] H. Valtna, A. Dubietis, G. Tamošauskas, P. Polesana, J. Galinis, **D. Majus**, G. Valiulis, D. Faccio, P. Di Trapani, and A. Piskarskas, Efficient four-wave parametric amplification and spatial soliton generation in transparent isotropic medium with kerr nonlinearity, Lithuanian J. Phys. **47**, 403–410 (2007).

[A13] J. Darginavičius, **D. Majus**, G. Tamošauskas, and A. Dubietis, Highly efficient third harmonic generation by means of four-wave difference-frequency mixing in fused silica, Lithuanian J. Phys. **49**, 171 – 174 (2009).

[A14] **D. Majus**, O. Jedrkiewicz, M. Molteni, P. Ragazzi, P. Di Trapani, and G. Tamošauskas, Spatio-temporal characterization of self-formed hollow light pulses in the pump depletion regime of second harmonic generation, Eur. Phys. J. Special Topics **199**, 77 – 87 (2011).

[A15] V. Jukna, **D. Majus**, G. Valiulis, A. Dubietis, Transformation of the probability density function in an optical parametric amplifier: application to rogue-wave-like statistics, Opt. Commun. **285**, 3654 – 3658 (2012).

[A16] J. Darginavičius, **D. Majus**, V. Jukna, N. Garejev, G. Valiulis, A. Couairon, and A. Dubietis, Ultrabroadband supercontinuum and third-harmonic generation in bulk solids with two optical-cycle carrier-envelop phase-stable pulses at 2 µm, Opt. Express **21**, 25211 (2013).

[A17] N. Garejev, I. Gražulevičiūtė, **D. Majus**, G. Tamošauskas, V. Jukna, A. Couairon, and A. Dubietis, Third- and fifth-harmonic generation in transparent solids with few-optical-cyclie midinfrared pulses, Phys. Rev. A **89**, 033846 (2014).

[A18] S. Minardi, D. Majus, A. Gopal, G. Tamošauskas, C. Miliàn, A. Couairon, T. Pertsch, and A. Dubietis, Energy deposition dynamics of femtosecond pulses propagating in water, submitted to Appl. Phys. Lett.

[A19] T. Roger, D. Majus, G. Tamošauskas, P. Panagiotopulous, M. Kolesik, G. Genty, A. Dubietis and D. Faccio, Extreme Events in Resonant Radiation from Three-dimensional Light Bullets, submitted to Phys. Rev. Lett.

Conference presentations

Presented by Donatas Majus

[C1] D. Majus, A. Dubietis, V. Jukna, G. Valiulis, G. Tamošauskas, A. Piskarskas, Highly efficient four-wave parametric amplification in condensed bulk media without filamentation, 2nd International Symposium on Filamentation, Paris, France (2008).

[C2] V. Jukna, D. Majus, G. Valiulis, A. Dubietis, Generation of periodic filament arrays by self-focusing of highly elliptical ultrashort pulsed laser beams , Northern Optics, Vilnius, Lithuania (2009).

[C3] D. Majus, V. Jukna, G. Tamošauskas, G. Valiulis, A. Dubietis, Three-Dimensional Mapping of Multiple Filament Arrays, tarptautinis forumas „Mokslas ir visuomenė modernioje Europoje“, Vilnius, Lithuania (2010).

[C4] D. Majus, V. Jukna, G. Valiulis, D. Faccio, A. Dubietis, Spatiotemporal Rogue Events in Femtosecond, CLEO/EUROPE – EQEC 2011, Munich, Germany (2011).

[C5] D. Majus, V. Jukna, G. Valiulis, D. Faccio, A. Dubietis, Rogue-wave-like statistics in femtosecond filamentation and white-light continuum generation in transparent dielectrics, International Workshop on Rogue Waves, Dresden, Germany (2011).

[C6] D. Majus, V. Jukna, G. Valiulis, A. Dubietis, Statistical properties of supercontinuum spectra in femtosecond filaments, 4th International Symposium on Filamentation COFIL 2012, Book of abstracts 140-141, Tucson, USA (2012).

[C7] D. Majus, V. Jukna, J. Galinis, G. Tamošauskas, and A. Dubietis, Ultrafast supercontinuum in solid media: statistical properties and infrared extension, 2nd TLL-COLIMA_FOTONIKA Joint Workshop, Vilnius, Lithuania (2013).

[C8] D. Majus, G. Tamošauskas, I. Gražulevičiūtė, N. Garejev, A. Lotti, A. Couairon, D. Faccio and A. Dubietis, Spatiotemporal light bullets as polychromatic Bessel beams, Photonics North 2014, Montreal, Canada (May 2014).

[C9] D. Majus, N. Garejev, I. Gražulevičiūtė, G. Tamošauskas, V. Jukna, A. Couairon, A. Dubietis, Third and fifth harmonic generation in transparent solids with few optical cycle mid-infrared pulses, CLEO:2014, San Jose, USA (June 2014).

[C10] D. Majus, G. Tamošauskas, I. Gražulevičiūtė, N. Garejev, A. Lotti, D. Faccio, A. Dubietis, Observation of non-solitary spatiotemporal light bullets in bulk dielectric media with Kerr nonlinearity, CLEO:2014, San Jose, USA (June 2014).

Co-author of the presentation

[C11] P. Bogdanovich and D. Majus, Investigation of accuracy of configuration interaction for the oxygen isoelectronic sequence, 36-oji Lietuvos nacionalinė fizikos konferencija, Vilnius, Lithuania (2005).

[C12] H. Valtna, A. Dubietis, G. Tamošauskas, P. Polesana, J. Galinis, D. Majus, G. Valiulis, D. Faccio, P. Trapani, and A. Piskarskas, Efficient four-wave parametric amplification and spatial soliton generation in transparent isotropic medium with kerr nonlinearity, 37-oji Lietuvos nacionalinė fizikos konferencija, Vilnius, Lithuania (2007).

[C13] V. Jukna, D. Majus, G. Valiulis, A. Dubietis, Periodinio šviesos giju skirstinio generavimas impulsiniu elipsiniu pluoštu, 38-oji Lietuvos nacionalinė fizikos konferencija, Vilnius, Lithuania (2009).

[C14] V. Jukna, D. Majus, G. Valiulis, A. Dubietis, Generation of periodic filament arrays by self-focusing of highly elliptical ultrashort pulsed laser beams, European Conference on Lasers and Electro-Optics (CLEO), Munich, Germany (2009).

[C15] D. Majus, V. Jukna, G. Tamošauskas, G. Valiulis, A. Dubietis, Three-Dimensional Mapping of Multiple Filament Arrays, 3rd International Symposium on Filamentation, Crete, Greece (2010).

[C16] A. Dubietis, D. Majus, V. Jukna, E. Pileckis, G. Valiulis, Ekstremaliųjų bangų statistika femtosekundinėse baltos šviesos gijos, 39-oji Lietuvos nacionalinė fizikos konferecija, Vilnius, Lithuania (2011).

[C17] A. Jarnac, D. Majus, G. Tamošauskas, A. Couairon, A. Houard, A. Mysyrowicz, A. Dubietis, Four-dimensional imaging of ultraviolet filaments in water, 4th International Symposium on Filamentation COFIL 2012, Tucson, USA (2012).

[C18] A. Couairon, A. Jarnac, G. Tamošauskas, D. Majus, A. Houard, A. Mysyrowicz, A. Dubietis, The whole life cycle of femtosecond filaments in water at 400 nm, , 4th International Symposium on Filamentation COFIL 2012, Tucson, USA (2012).

[C19] J. Darginavičius, D. Majus, V. Jukna, N. Garejev, T. Vasiliauskas, A. Dubietis, Ultrabroadband supercontinuum generation in bulk solids with few-optical-cycle CEP-stable pulses at 2 μm, Norhtern Optics 2012, Snekkersten, Denmark (2012).

[C20] A. Dubietis, J. Darginavičius, D. Majus, N. Garejev, V. Jukna, G. Valiulis, Supercontinuum generation in wide bandgap dielectrics with two optical-cycle infrared pulses, Lietuvos nacionalinė fizikos konferencija LNFK 40, Vilnius, Lithuania (2013).

[C21] A.Couairon, G.Tamosauskas, D.Majus, A.Dubietis, A.Jarnac, A.Houard, A.Mysyrowicz, Femtosecond ultraviolet filamentation in water, ICONO/LAT:2013, Moscow, Russia (2013).

[C22] A. Couairon, V. Jukna, F. Silva, D.R. Austin, M. Hemmer, M. Baudisch, A. Thai, J. Biegert, D. Faccio, A. Jarnac, A. Houard, Y. Liu, A. Mysyrowicz, S. Grabielle, N. Forget, A. Durecu, M. Durand, K. Lim, E. McKee, M. Baudelet, M. Richardson, Filamentation third harmonic and supercontinuum generation, conical emission in the anomalius dispersion region of transparent solids, Workshop on "Mathematical Methods and Models in Laser Filamentation", Montreal, Canada (2014)

[C23] A. Dubietis, N. Garejev, V. Jukna, G. Tamošauskas, I. Gražulevičiūtė, D. Majus, G. Valiulis, A. Couairon, Nonlinear optical phenomena in bulk dielectric media with few optical cycle mid-IR pulses, Nonlinear Photonics 2014, Barcelona, Spain (2014).

[C24] S. Minardi, D. Majus, A. Gopal, G. Tamošauskas, C. Miliàn, A. Couairon, T. Pertsch, A. Dubietis, Imaging Ultrafast Light-Matter Interaction with Inverse Raman Scattering, Nonlinear Photonics 2014, Barcelona, Spain (2014).

[C25] D. Faccio, T. Roger, F. Biancalana, M. Petev, M. Clerici, R. Morandotti, F. Legare, D. Majus, G. Tamošauskas, A. Dubietis, A. Couairon, P. Panagiotopoulos, M. Kolesik, G. Genty, Resonant Radiation Physics in Collapsing Light Pulses, Advanced Laser Technologies ALT14, Cassis, France (October 2014).

Co-authors contribution

All the experiments described in this thesis were performed in Vilnius University, Department of Quantum Electronics during the period 2010–2014 by the author himself, paper [A5] was prepared in Stella Summer School. It is important to specify the significant contribution of these co-authors:

- Prof. **A. Dubietis** [A1-A4, A5-A9] formulated the general tasks. He initiated multiple filament, supercontinuum statistics and MIR light bullets experiments. He helped to interpret the results and present them to scientific community;
- Dr. **G. Tamošauskas** [A2, A7, A8, A9] together performed the 3D mapping experiments and assisted during all other experiments. He should be credited for invaluable advices, ideas and discussions related to experimental laser physics;
- Graduate student **I. Gražulevičiūtė** [A9] assisted in 3D mapping measurements and helped to process the data;
- Graduate student **N. Garejev** [A9] assisted in 3D mapping measurements;
- Ph. D. **A. Lotti** [A9] performed energy flux calculations and helped to interpret and publish the results;
- Prof. **A. Couairon** initiated Practitioner's guide to laser pulse propagation models and simulation [A5], initiated experiment on whole life-cycle measurements of UV femtosecond filament [A8], helped to interpret and publish the results [A9];
- Prof. **D. Faccio** [A3, A9] helped to interpret and publish the results;
- Dr. **V. Jukna** [A1-A4, A7] performed numerical simulations, helped to interpret and publish the results;
- Prof. **G. Valiulis** [A1-A4] formulated a theoretical description of the multiple filamentation as four-wave mixing, provided a theoretical basis for many nonlinear optics phenomena;
- Ph. D. student **J. Galinis** [A7] performed supercontinuum infrared extension measurements;
- Ph. D. **A. Jarnac** [A8] together performed complete life-cycle measurements of the UV femtosecond filament, processed the data.

The structure of the thesis

The thesis is organized as follows:

- In Chapter 1 theoretical models and numerical simulations used to back-up experimental research are described. An example with femtosecond chirped pulse propagation is provided which shows that phenomenological model (Marburger's law) could be extended and used for beam focusing as well as pulse splitting analysis. In addition three-dimensional mapping technique which was extensively employed through the thesis research is described.
- Chapter 2 analyzes single femtosecond filament dynamics under two vastly different conditions - normal and anomalous GVD regime. Full life-cycle of the UV femtosecond filament and spatiotemporal light bullets in the MIR were analyzed.
- Chapter 3 is devoted for femtosecond supercontinuum – spectral intensity stability and extreme event statistics, infrared extension is analyzed and explained through spatiotemporal evolution of the filament.
- In Chapter 4 generation of periodic multifilamentary beams is analyzed. Period between the filaments and temporal multifilamentary beam structure are explained through four-wave mixing and X-wave models.

1 Ultrashort laser pulses in dielectric media: theoretical model, numerical simulations and experimental techniques

As it is obviously demonstrated in this thesis, ultra-short pulse experiments can barely exist without the support from modeling and simulation in order to understand and interpret measured data, especially as nonlinear optics continues to explore ever more extreme regimes. Simulation in ultrafast nonlinear optics has reached a degree of maturity, several simulation approaches are becoming as standard tools that help researchers working in a field understand (and use) numerical simulations without being experts of it. Recent paper by Couairon et al. [35] provides a didactic and instruction motivated text which includes detailed derivation from Maxwell's to pulse envelope propagation equations and comprehensive discussion on influence of various assumptions and simplifications as well as practical issues.

1.1 Unidirectional pulse propagation equation

All numerical simulations presented in this thesis except the one described in Sec. 2.1 were done according to the model described below.

The propagation dynamics of the ultrashort-pulsed elliptical light beams in the nonlinear medium with cubic nonlinearity was studied using one-directional propagation equation for the linearly polarized wave with the complex envelope $A(t, x, y, z)$, which is described in detail in [36]:

$$\frac{\partial A}{\partial z} + \int\int\int_{+\infty}^{-\infty} T(t', x', y') A(t - t', x - x', y - y', z) dx' dy' dt' = \frac{i\omega_0 n_2}{c}|A|^2 A - \frac{\beta^{(K)}}{2}|A|^{2K-2}A - \frac{\sigma}{2}(1 - i\omega_0\tau_c)\rho A, \tag{1.1.1}$$

where z is the propagation variable, t is the temporal coordinate corresponding to the frame of reference moving with the group velocity of the pulse $v_g = \frac{\partial\omega}{\partial k}\Big|_{\omega_0}$, ω_0 is the carrier frequency, $k(\omega) = \omega n(\omega)/c$ is the wave number, $k_0 = k(\omega_0)$, n and n_2 are the linear and nonlinear refractive indexe, respectively, c is the speed of light in vacuum, K is the order of the multiphoton absorption, $\beta^{(K)}$ is the multiphoton absorption coefficient, ρ is the free electron density, σ is the cross-section for electron-neutral inverse bremsstrahlung and τ_c is the electronic collision time in the conduction band. The evolution of the wave envelope due to diffraction and material dispersion was accounted via "medium response" function:

$$T(t, x, y) = \int\int\int_{+\infty}^{-\infty} D(\Omega, k_x, k_y) \exp\Big[-i(\Omega t - k_x x - k_y y)\Big] d\Omega dk_x dk_y, \tag{1.1.2}$$

where $\Omega = \omega - \omega_0$ is the frequency detuning from the carrier frequency, and k_x and k_y are the transverse components of the wavevector. Treating transverse components of the wavevector separately allows to study non-cylindrical beams and was successfully used in simulations of elliptical beams. Eq.1.1.1 was solved using the split step method, accounting for full material dispersion and diffraction in the non-paraxial case through a parameter

$$D(\Omega, k_x, k_y) = \sqrt{k(\omega_0 + \Omega)^2 - k_x^2 - k_y^2} - k_0 - \frac{\Omega}{v_g}, \tag{1.1.3}$$

which describes the spectral phase shift. We assumed that the dynamics of the free electron density is contributed by the multiphoton and avalanche

ionization only, neglecting electron diffusion and recombination terms owing to a sufficiently long lifetime of the electron plasma (e.g. 170 fs in fused silica[37]), which exceeds the input-pulse duration in all experimetal setups in this thesis. The evolution equation for the electron density is then given by

$$\frac{\partial \rho}{\partial t} = \frac{\beta^{(K)}}{K\hbar\omega_0}|A|^{2K} + \frac{\sigma}{E_g}\rho|A|^2, \tag{1.1.4}$$

where E_g denotes the medium bandgap. The cross-section for inverse bremsstrahlung reads as

$$\sigma = \frac{e^2\tau_c}{cn_0\epsilon_0 m(1+\omega_0^2\tau_c^2)}, \tag{1.1.5}$$

where $m = 0.635m_e$ is the reduced electron-hole mass. Specific medium parameters used and input pulse definitions are provided for each simulation in respective sections.

Alternatively, the extended nonlinear Schroedinger equation could be written in spectral domain:

$$\frac{\partial S(\Omega, k_\perp)}{\partial z} + iD(\Omega, k_\perp)S(\Omega, k_\perp) = S_N(\Omega, k_\perp), \tag{1.1.6}$$

where z is the longitudinal coordinate, $\Omega = \omega - \omega_0$ is the frequency detuning from the carrier frequency ω_0, and $k_\perp$ is the transverse wave number. The function $D(\Omega, k_\perp)$ describes linear propagation and accounts for diffraction in the non-paraxial case, full dispersion, and additionally compared to 1.1.3 linear absorption:

$$D(\Omega, k_\perp) = \sqrt{k(\omega_0+\Omega)^2 - k_\perp^2} - k_0 - \frac{\Omega}{\nu_g} - i\alpha(\Omega), \tag{1.1.7}$$

where $\nu_g = \frac{\partial\omega}{\partial k}|_{\omega_0}$ is the group velocity of the pulse, $k(\omega) = \omega n(\omega)/c$ is the wave number, with $k_0 = k(\omega_0)$ and $\alpha(\Omega)$ is the absorption coefficient, whose values in the visible and infrared were combined using data from [38] and

[39]. The complex amplitude of the pulse $A(t, r, z)$ and $S(\Omega, k_\perp)$ are related via Fourier and Hankel transforms:

$$A(t, r, z) = \int_{-\infty}^{+\infty} \int_{0}^{+\infty} S(\Omega, k_\perp) e^{i\Omega t} J_0(k_\perp r) k_\perp \, \mathrm{d}k_\perp \, \frac{\mathrm{d}\Omega}{2\pi}, \tag{1.1.8}$$

where t is the temporal coordinate corresponding to the frame of reference moving with the group velocity of the pulse and r is the radial coordinate. $S_N(\Omega, k_\perp)$ is the spectral representation of the nonlinear terms:

$$S_N(\Omega, k_\perp) = \int_{-\infty}^{+\infty} \int_{0}^{+\infty} N(t, r) e^{-i\Omega t} J_0(k_\perp r) r \, \mathrm{d}r\mathrm{d}t \tag{1.1.9}$$

where

$$N(t, r) = \frac{i\omega_0 n_2}{c} |A|^2 A - \frac{n_2}{c} \frac{\partial}{\partial t} (|A|^2 A) - \frac{\beta^{(K)}}{2} |A|^{2K-2} - \frac{\sigma}{2} (1 - i\omega_0 \tau_c) \rho A. \tag{1.1.10}$$

The terms on the right hand side describe the instantaneous Kerr effect, self-steepening, multiple photon absorption, and the effect of free electron plasma. K is the order of the multiphoton absorption, calculated according to band-gap of the medium E_g and a single photon energy $\hbar\omega_0$. $\beta^{(K)}$ is the multiphoton absorption coefficient, is the free electron density, σ is the cross section for electron-neutral inverse bremsstrahlung, and τ_c is the electronic collision time in the conduction band.

In 2.1 a little bit different approach to numerical simulations was used. While 1.1.1 is written for pulse envelope is temporal and spatial domains, 1.1.6 is written in purely frequency domain (temporal frequency and spatial frequency), an approach in between is possible. The model used for numerical simulations consists of a 3D unidirectional propagation equation with cylindrical symmetry for the nonlinear envelope $E(t, r, z)$ coupled with an evolution equation for the electron density $\rho(t, r, z)$ generated by the high-intensity pulse. The variables t, r, and z denote the pulse local time, the radial coordinate, and the propagation distance, respectively. Dis-

persive medium is characterized by a frequency-dependent refractive index $n(\omega)$ and a dispersion relation $k(\omega) \equiv n(\omega)\omega/c$. We use conventional notations for the refractive index $n_0 \equiv n(\omega_0)$, wave number $k_0 \equiv k(\omega_0)$, and inverse group velocity $k_0' \equiv (\partial k/\partial\omega)_{\omega_0}$ at the central laser frequency ω_0. We define the dispersion function $\mathcal{K}(\omega) \equiv k(\omega) - k_0 - k_0'(\omega - \omega_0)$ and the nonlinear dispersion function $\mathcal{Q}(\omega) = \omega^2/k(\omega)c^2$. One of the most convenient ways to implement dispersion functions in the pulse propagation equation is in the frequency domain. We consider the frequency components $\mathcal{E}(\omega, r, z) \equiv \mathcal{F}[E(t, r, z)]$ for the electric-field envelope, where $\mathcal{F}$ denotes Fourier transform from the temporal to the spectral domain. The propagation equation takes the canonical form [35]:

$$\frac{\partial\mathcal{E}}{\partial z} = i\mathcal{K}(\omega)\mathcal{E} + \frac{i}{2k(\omega)}\nabla_\perp\mathcal{E} + i\mathcal{Q}(\omega)\frac{\mathcal{P}}{2\epsilon_0} - \frac{\mathcal{J}}{n(\omega)2\epsilon_0 c}, \tag{1.1.11}$$

where the nonlinear polarization $\mathcal{P}(\omega, r, z) \equiv \mathcal{F}[P(t, r, z)]$, with $P \equiv 2\epsilon_0 n_0 n_2 IE$, describes the response of a Kerr medium with nonlinear index coefficient n_2 for a pulse of intensity $I \equiv (1/2)\epsilon_0 c n_0 |E|^2$. The current $\mathcal{J}(\omega, r, z) \equiv \mathcal{F}[J(t, r, z)]$, where $J \equiv J_{MPA} + J_{PL}$ comprises two contributions due to multiphoton absorption (MPA) and plasma-induced effects (PL). The current describing MPA reads $J_{MPA} = \epsilon_0 c n_0 \beta_K I^{K-1} E$, with coefficient β_K and number of photons K. Plasma-induced effects, i.e., plasma absorption and plasma defocusing are included in a single expression for the current $\mathcal{J}_{PL} = \epsilon_0 c\sigma(\omega)\mathcal{F}[\rho E]$ with complex-valued coefficient $\sigma(\omega)$, the real part of which, σ_r, corresponds to the cross section for inverse Bremsstrahlung in the Drude model:

$$\sigma(\omega) \equiv \frac{\omega_0^2\tau_c}{c\rho_c}\frac{1}{1 - i\omega\tau_c}, \tag{1.1.12}$$

where τ_c denotes the collision time in medium and ρ_c, the critical plasma density beyond which the medium is no longer transparent. The quantity $\omega_0^2/c\rho_c$ is a constant ($q_e^2/c\epsilon_0 m \sim 0.1\text{cm}^2/\text{s}$) which does not depend on the laser central frequency. The evolution of the electron plasma density is modeled by a rate equation modeling multiphoton and avalanche ionization,

as well as recombination with rate η_r:

$$\frac{\partial \rho}{\partial t} = \left(\frac{\beta_K}{K\hbar\omega_0} I^K + \frac{\sigma_r(\omega_0)\rho I}{U_i} \right) \left(1 - \frac{\rho}{\rho_{nt}} \right) - \eta_r \rho^2, \tag{1.1.13}$$

1.2 Simplified model and results of numerical simulations

Material related to this section was published in [A5]

Extensive numerical simulations are not always necessary since understanding concepts of the most important effect sometimes can be simplified to certain models. As it is shown in section 4.1 and the following pages simple models let us grasp essential information about the filamentation.

Marburger's formula [6]:

$$z_c = \frac{0.367 z_R}{\sqrt{[(P_{in}/P_{cr})^{1/2} - 0.852]^2 - 0.0219}} \tag{1.2.1}$$

where $z_R = k_0\omega_0^2/2$ denotes the Rayleigh (typical diffraction) length is known to reproduce well the power threshold for catastrophic behavior and position of the collapse when a non-chirped powerful pulse propagates in a pure Kerr medium. The filamentation threshold for non-chirped pulses is known to exceed P_{cr} and lead to pulse-splitting [26, 40]. By monitoring the position of the nonlinear focus and the chirped pulse-splitting dynamics, we extended Marburger's formulation coupled with the so-called moving focus picture [41–44] to fit our numerical results for the splitting velocity. This extends the moving-focus model to media where intense laser pulses also undergo nonlinear losses and dispersion. Numerical experiments on nonlinear propagation in water were performed by solving the nonlinear Schroedinger equation, which accounts for diffraction, dispersion (second order), self-focusing and multiphoton absorption and compared to theoretical model in 1.1 does not account for non-paraxial and generated plasma effects:

$$\frac{\partial \mathcal{E}}{\partial z} = \frac{i}{2k_0}\Delta_\perp \mathcal{E} - i\frac{k_0''}{2}\frac{\partial \mathcal{E}}{\partial t^2} + i\frac{\omega_0}{c} n_2 \mathcal{I}\mathcal{E} - \frac{\beta_K}{2}\mathcal{I}^{K-1}\mathcal{E}, \tag{1.2.2}$$

where $\mathcal{I}$ denotes the pulse intensity. Equation (1.2.2) includes a limited number of physical effects, namely diffraction, second order group velocity dispersion, optical Kerr effects and multiphoton absorption. A split step scheme was used, treating dispersion in the Fourier domain for the first half-step, and other effects in the temporal domain for the second half-step. The simulation of Eq. (1.2.2) aims at interpreting the pulse splitting phenomenon, a standard effect in the physics of femtosecond filamentation [45, 46], in the framework of the moving focus model. Strictly speaking, the moving focus model does not accurately reproduce filamentation physics in dispersive media [47] but we will show that relaxing its underlying assumptions allows for the derivation of scaling laws that predict rather accurately the pulse-splitting velocities obtained by simulations of the propagation of chirped intense pulses described by Eq. (1.2.2).

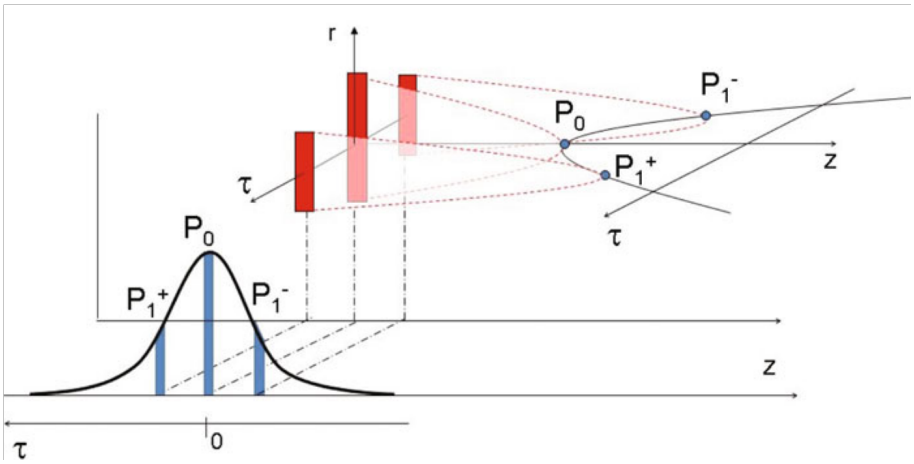

Figure 1.2.1: Prediction of the moving focus model for the nonlinear beam foci associated with given power for each time slice within the pulse. The time slice with peak power P_0 collapses at the shortest distance from the laser. Time slices with smaller power collapse farther on the propagation axis while the central time slices undergo nonlinear absorption. The simultaneous collapse of two time slices P_{1-} and P_{1+} on the ascending and descending edges of the pulse lead to pulse splitting.

1.2.1 Moving focus model for ultrashort pulses

The moving focus model consists of a slice by slice pulse selffocusing in the sense that the pulse is viewed as a collection of independent thin time slices undergoing self-focusing [44, 48]. This assumption is valid when the physical effects coupling the various time slices together can be neglected. Each time slice contains a given power. In an ideal Kerr medium, all central

slices with power above critical would collapse at distances that become larger as the corresponding power is closer to P_{cr}. The slices with power below P_{cr} diffract. In a real medium, several physical effects can arrest collapse, e.g., nonlinear losses reduce power of collapsing time slices once intensity exceeds a certain threshold. In this process, an intensity maximum (nonlinear focus) is reached and the propagation continues. The nonlinear foci corresponding to the different temporal slices of the pulse with power above critical do not appear simultaneously in the laboratory frame, and can be viewed as a moving focus. Figure 1.2.1 shows the locations of the nonlinear foci corresponding to the peak power P_0 of the pulse, and those corresponding to a smaller power P_1- in the leading or in the trailing part of the pulse. In a pure Kerr medium, these beam collapse positions are predicted by the Marburger formula (Eq. 1.2.1). In the presence of nonlinear losses, the slices with larger power collapse faster and lose at least part of their power, thereby leading to the occurrence of pulse splitting beyond the nonlinear focus. It manifests itself in the form of two intensity peaks departing from each other, each corresponding to the nonlinear focus of a given time slice [49]. In a dispersive medium, the assumption of independent time slices no longer holds, however, we still expect the moving focus model to accurately predict the positions of nonlinear foci and pulse splitting over distances shorter than the typical dispersive length. When the distance to the nonlinear focus and the dispersive length have the same order of magnitude, we will show that the moving focus picture and Marburger's formulation for beam collapse can be extended so as to fit the splitting velocities obtained from simulation results.

1.2.2 Pulse splitting

The collimated input pulse had Gaussian intensity distribution in both space and time, with pulse duration of 50 fs at full width at half maximum (FWHM), beam width $\omega_0 = 100\,\mu$m, wavelength 800 nm. Medium parameters corresponded to water: refractive index $n_0 = 1.328$, nonlinear refractive index coefficient $n_2 = 1.6 \times 10^{-16}\,\mathrm{cm}^2/\mathrm{W}$, dispersion coefficient $k_0^{(2)} = 241\,\mathrm{fs}^2/\mathrm{cm}$, cross-section for fifth-order multi-photon absorption $\beta_5 = 8 \times 10^{-50}\,\mathrm{cm}^7/\mathrm{W}^4$ [45, 46]. The effects of input peak power and initial pulse chirp were investigated. The input power varied from $1.5P_{cr}$ to $50P_{cr}$ and the pulse chirp parameter from -10 to 10. Simulations were performed

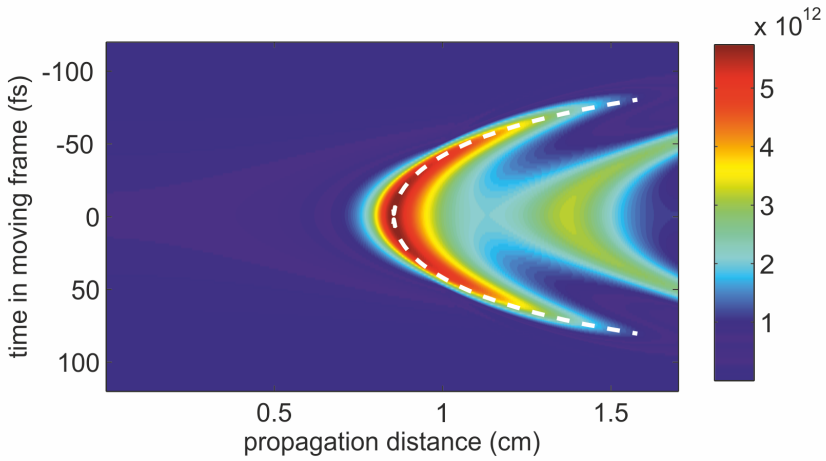

Figure 1.2.2: Pulse intensity profile as a function of propagation distance. The input pulse power is $P_0 = 10P_{cr}$, and the input chirp is $C = -1$. The colorbar shows intensity in W/cm^2. The white dashed curve represents the best fit, by using the modified Marburger law, of the peak positions of each sub-pulse resulting from pulse splitting beyond the nonlinear focus. A second nonlinear focus followed by another pulse splitting phenomenon can be observed about 1cm beyond the main collapse.

by setting the time window to $T = 400\,\text{fs}$ with $N_T = 2^8$ sampling points, and the propagation distance was divided into $N_z = 1000$ steps. These parameters closely correspond to those determined in [35] to achieve the minimal relative error. To optimally use the computing time at a given resolution, the propagation length was adjusted from 1 to 3 cm so as to exceed 2.5 times the position of nonlinear focus roughly estimated with the original Marburger law. Fig. 1.2.2 shows the evolution of the intensity profile of the pulse along the propagation distance for an input pulse power of $10P_{cr}$ and chirp $C = -1$. Around $z = 0.8\,\text{cm}$, the intensity starts to increase, and beyond the nonlinear focus at $z \sim 0.9\,\text{cm}$ a splitting event is observed with the formation of two sub-pulses in the leading and trailing edges of the input pulse. Fig. 1.2.2 shows peak intensities of the leading and trailing pulses. The velocity of a given peak is given by $v_p = (v_g^{-1} + dt/dz)^{-1}$, where v_g denotes the moving frame or pulse group velocity and dt/dz, the inverse of the peak velocity in the local frame. The latter quantity is obtained from the slope of the curve in Fig. 1.2.2 representing the temporal position of the peak intensity in the pulse frame as a function of propagation distance.

1.2.3 Modified Marburger's law

We expect that Marburger's law (Eq. 1.2.1), originally derived for the continuous wave regime from a fit of numerical simulation results, requires modifications to match the collapse position of chirped pulses. We will therefore fit our numerical results for the nonlinear foci by assuming a slice by slice self-focusing following a modified Marburger's law:

$$z_c(t) = \Delta z_c + \frac{b_M z_R}{\sqrt{[(P_{in}(t)/P_{cr})^{1/2} - a_M]^2 - (1 - a_M)^2}} \tag{1.2.3}$$

$$P_{in}(t) = P_0 \exp(-2t^2/r^2 t_p^2) \tag{1.2.4}$$

where a_M, b_M, Δz_c, and r are free parameters to be determined by fitting numerical results. The original Marburger law (Eq. 1.2.1) for slice-by-slice self-focusing is recovered for $a_M = 0.852$, $b_M = 0.367$ and $\Delta z_c = 0$, $r = 1$. The parameter Δz_c represents a shift along the z-axis of the nonlinear focus related to the most intense time slice, whereas the parameter r accounts for pulse lengthening or pulse shortening induced by dispersion and input chirp before the nonlinear focus. We searched for parameters of the modified Marburger's law (Eq. 1.2.3, 1.2.4) realizing the best fit for each simulation performed with a given input chirp and input power P_0. First, we allowed all parameters a_M, b_M, Δz_c, and r to vary as a function of P_0 in the fitting procedure. However, best fits were obtained for nearly constant values of parameters $a_M = 0.7823$ and $b_M = 0.405$, close to original Marburger's coefficients. We therefore decreased the number of free parameters from four to two by keeping constant a_M and b_M and by allowing only Δz_c, and r to vary as functions of P_0 and chirp C. The dashed curve in Fig. 1.2.2 shows an example of best fit to numerical results. For a given input power P_0, pulse splitting does only appear within a range of input chirps since dispersion induced pulse lengthening leads to a decrease of the pulse power below critical for strong chirp and low pulse power. Fits were therefore calculated for parameters that led to a clear splitting event. Furthermore, for the highest powers ($50P_{cr}$), pulse reshaping into a flat-top pulse occurs before the nonlinear focus due to multiphoton absorption. In that case, a proper fit could not be obtained due to the assumption of a Gaussian pulse

shape in the model [see Eq. 1.2.4]. This restricts the validity of out fits to chirp coefficients between -5 and 5 and pulse powers up to $40P_{cr}$.

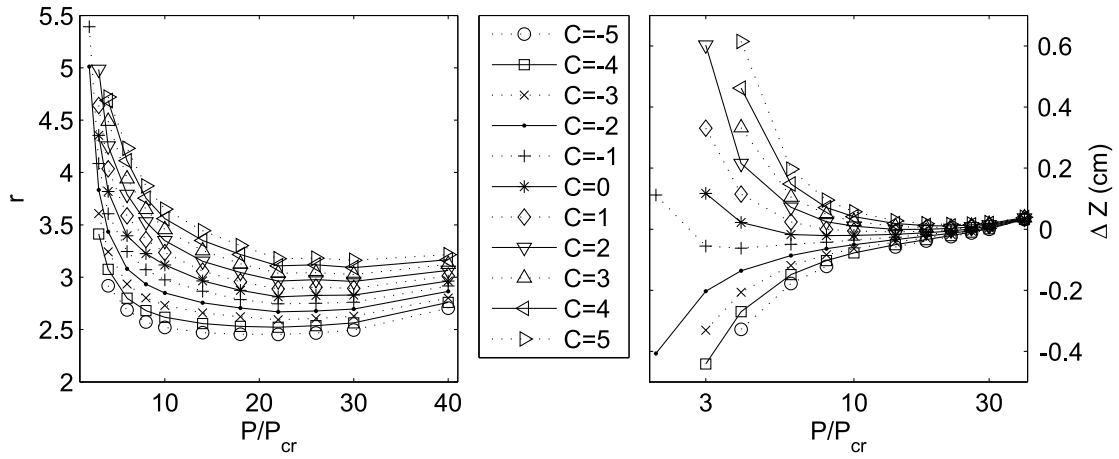

Figure 1.2.3: Modified Marburger's law coefficient dependence on power for different pulse chirps.

Figure 1.2.3 summarizes curve fitting results. The parameter r takes into account pulse lengthening during the propagation toward the nonlinear focus and therefore naturally depends on both input chirp and power, which affects pulse reshaping through pulse dispersion and beam self-focusing. At a given input power, both r and Δz_c are quasi linearly dependent on the chirp parameter. However, a larger region of chirp parameter and pulse power needs to be investigated to confirm this linear dependence. Our data cover chirp coefficients between -5 and 5. Larger absolute values for the chirp coefficient led to more complicated dynamics during pulse propagation, for which pulse splitting was either absent or too short-lived to allow for an accurate fit. Powers between 1.5 and $40P_{cr}$ and chirp coefficients between -5 and 5 led to clear pulse splitting events, and excellent agreement between numerical results and the modified Marburger's law for the splitting velocities. Positive chirp values lead to pulse lengthening and thus tend to shift the nonlinear focus toward larger distances with respect to the nonlinear focus of non-chirped pulses position of the collapse ($\Delta z_c > 0$ and increases with increasing C). In contrast, negative chirps lead to pulse compression and an increase of the peak power during the self-focusing stage, resulting in a shift of the nonlinear focus toward the laser ($\Delta z_c < 0$). All numerical results shown in Fig. 1.2.3 can be approximated with phenomenological scaling laws that depend on the chirp parameter C and ratio

$p \equiv P/P_{cr}$:

$$r = 1.58 + 0.0188(p-1) + \frac{3.94 - 0.348C}{\sqrt{p-1}} \tag{1.2.5}$$

$$\Delta z_c = -0.0259 + 4.14 \times 10^{-5}(p-1)^5 + \frac{5.49}{p^3} + \frac{0.536C}{(p-1)^{1.63}} \tag{1.2.6}$$

We found in particular an excellent R-square of 0.9998 by fitting numerical results of Fig. 1.2.3a with Eq. 1.2.5 whereas the error in fitting numerical results in Fig. 1.2.3b with Eq. 1.2.6 does not exceed 10%.

1.2.4 Conclusion

We expect that two-parameter modification of Marburger's law (Eq. 1.2.3-1.2.6) accompanied by the moving focus picture is generic enough to apply to other media and laser wavelengths. Scaling laws (Eq. 1.2.5) and (Eq. 1.2.6) have to be confirmed or adapted for different media and laser wavelength; in particular the exact value of the fitting parameters is expected to depend on medium dependent parameter such as the cross-section for nonlinear absorption and the GVD coefficient. This dependence has to be determined by fitting additional numerical results extending the results of this project/research. The method allows us to predict in a large parameter range the position in local time and the velocity of split-pulses formed by the filamentation dynamics in an ideal medium representing water. Extension of this moving focus picture to realistic condensed media that include high-order dispersion, plasma generation and Raman-Kerr effects, is an open question which may be answered to by relaxing the assumption of a frozen Gaussian profile for the pulse power in the moving focus picture, as proposed in e.g., Ref. [3, 49].

1.3 Three-dimensional imaging of complex wave-packets

In five experiments described in this thesis three-dimensional mapping technique [50, 51] was used to investigate spatio-temporal properties of the

wave-packets in interest. 3D mapping enables precise reconstruction the spatiotemporal intensity profiles of the light pulses within the entire wave-packet. In all the cases experiment is based on the commonly used design characterized by a short gate pulse shifted in time with respect to the pulse under investigation. The resulting slice of the pulse, generated as cross-correlation signal, is recorded by a CCD camera for spatial information.

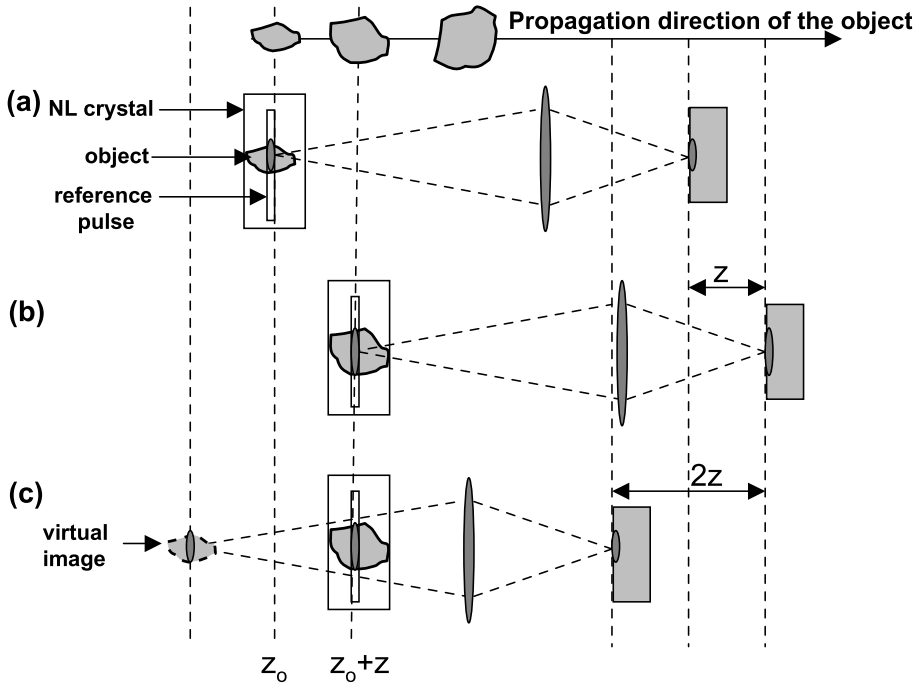

Figure 1.3.1: Three reconstruction schemes of a slice obtained from an object wave packet. In (a) the slice is reconstructed as a real image (confocal configuration); in (b) the slice is reconstructed after the object propagated a distance z; in (c) the slice corresponding to the one imaged in (b) is used to reconstruct the virtual image of the one imaged in (a). Image from [50].

Three dimensional mapping relies on investigated wave packet and probe pulse interaction in nonlinear medium (Fig. 1.3.1). Typically wave packet directly after nonlinear propagation is the most interesting therefore imaging of investigated wave packed (WP) with $4f$ optical system to nonlinear medium or holographic imaging was employed. The later setup allows avoiding $4f$ optical system which could introduce additional dispersion. However it requires placing nonlinear gating crystal as close to origin of the wave packet in interest as possible. In practice this leads to non-collinear interaction between WP and the probe pulse which raise additional constrains to gating crystal if proper spatial and temporal resolution is required.

Intensity distribution is measured in the reference system of a wave packet

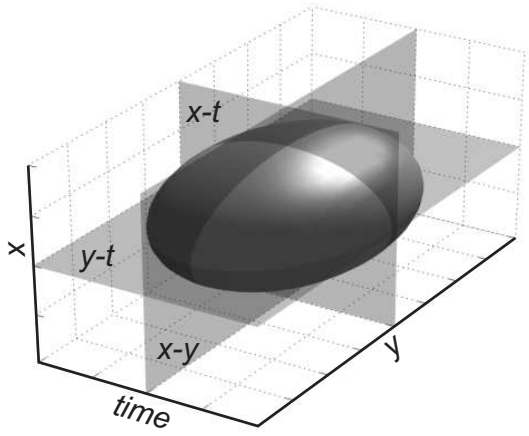

Figure 1.3.2: Iso-intensity surface of an ideal elliptical Gaussian pulsed beam and three perpendicular planes, used to slice the three-dimensional intensity profile.

$(x, y, t - z/c)$. Lets assume linearly polarized wave packet and the probe pulse with slowly varying amplitudes $\bar{E}_0$ and $\bar{E}_R$ respectively:

$$\bar{E}_0 = E_0(x, y, z, t)e^{i[\omega_1 t - k_{1z}z - k_{1x}x]} + \text{c.c.}, \tag{1.3.1}$$

$$\bar{E}_R = E_R(x, y, z, t)e^{i[\omega_2 t - k_{2z}z + k_{2x}x]} + \text{c.c.}, \tag{1.3.2}$$

ω_1, ω_2 - central frequency, both pulses are propagating in the positive z direction and colliding at the angle in the $x - y$ plane. In case nonlinear gating is realized as sum-frequency generation nonlinear polarization reads as:

$$P_{SF} \propto 2E_0E_Re^{i[\omega_3 t - k_z\omega_3 z]} + \text{c.c.} \tag{1.3.3}$$

where the phase and energy matching conditions $k_{3z} = k_{1z} + k_{2z}$, $k_{1x} = k_{2x}$ and $\omega_3 = \omega_1 + \omega_2$ have been used. The sum frequency field propagates in along positive z-axis. Lets assume: (i) depletion from the $\bar{E}_0$ and $\bar{E}_R$ is small; (ii) diffraction and dispersion in the nonlinear crystal is negligible; (iii) the wave packet, probe pulse and generated signal pulses have equal group velocities u. These assumptions hold on as long as the nonlinear crystal thickness is small compared to characteristic lengths of the system: non-linear length, dispersion and diffraction lengths, pulse walk-off length. If we introduce probe pulse time delay τ_i in the traveling reference frame $\tau = t - z/u$, equation for sum-frequency pulse slowly varying amplitude

E_{SF} takes form:

$$\frac{\mathrm{d}E_{SF}}{\mathrm{d}z} = 2i\sigma E_0(x,y,\tau,z)E_R(x,y,\tau-\tau_i,z), \tag{1.3.4}$$

where σ is non-linear coupling term. This equation could be integrated:

$$E_{SF}(x,y,\tau,z_0) = 2i\sigma E_0(x,y,\tau,z_0)E_R(x,y,\tau-\tau_i,z_0)\Delta z, \tag{1.3.5}$$

where Δz is nonlinear mixing crystal thickness, z_0 - its position. For a given time delay τ_i, sum-frequency signal:

$$I(x,y,\tau_i,z_0) \simeq (\sigma\Delta z)^2 \int_{-\infty}^{+\infty} |E_0(x,y,\tau,z_0)|^2 |E_R(x,y,\tau-\tau_i,z_0)|^2 \mathrm{d}\tau, \tag{1.3.6}$$

In case probe pulse is spatially homogeneous in the transverse $x-y$ plane and temporally much shorter than the investigated wave packet, previous expression could be simplified to:

$$I(x,y,\tau_i,z_0) \propto (\sigma\Delta z)^2 |E_R|^2 I_0(x,y,\tau_i,z_0), \tag{1.3.7}$$

where $I_0 = |E_0|^2$.

By changing the time delay between the tested WP and probe pulse, a collection of the cross-correlation images can be acquired which is used to reconstruct the spatiotemporal intensity profile of the test WP. The reconstructed spatiotemporal intensity profile of the WP can be studied in detail, providing the two-dimensional spatiotemporal slices in the x-t and y-t planes, as well as the time-integrated images in the x-y plane, that is an intensity distribution of the WP in the direction perpendicular to the propagation direction, as schematically illustrated in Fig. 1.3.2. Complementary, the low intensity input test pulse propagating without the onset of self-action effects in the sample could be used to obtain the absolute calibration of spatial and temporal coordinates in the three-dimensional images and their corresponding cross-sections.

2 Filamentation dynamics in normal and anomalous GVD regime

Material related to this chapter was published in [A8,A9]

Femtosecond light filaments have distinct spatiotemporal intensity localization which is very favourable for applications requiring energy deposition in transparent (semi-transparent) solids. Ideally one would require propagation invariant electromagnetic wave-packets – light bullets, that are long sought in many areas of modern optics and attract a great deal of interest in fundamental and applied research [52]. Generation of three-dimensional light bullets, which propagate in the medium without natural dispersive broadening and diffractive spreading, is a non-trivial task from the analytical and numerical points of view, and even more complicated to achieve in real experimental settings [53–55].

Apart from the goal to achieve invariant propagation, understanding the propagation dynamics is also relevant topic in femtosecond filament research. While there are numerous works on femtosecond filaments at 800 nm (popular femtosecond laser central wavelength of Ti:sapphire system), there were very few at wavelengths other than this. In the UV, material dispersion is much higher, multiphoton absorption starts earlier and supercontinuum expansion is limited to the red side shift because of the absorption edge in the UV. In the MIR range, GVD is negative which totally changes the dynamics of the filamentation. In this Chapter measurements that fully characterize the whole life cycle of femtosecond pulses undergoing filamentation in water at 400 nm and detailed experimental investigation, which uncovers the nature of light bullets generated from self-focusing in a bulk dielectric medium with Kerr nonlinearity in the anomalous group velocity dispersion regime are presented.

2.1 Evolution cycle of femtosecond filaments in the UV

Laser energy deposition in liquids is the first stage of numerous applications, from bond breaking in chemical engineering and multiphoton induced chemistry to biomedical sciences [56, 57]. In particular, safe noninvasive eye or brain laser surgery, lithotripsy, and laser-based cancer radiotherapy require high energies to be deposited in a narrow focal region by avoiding collateral damage [58–62]. Many investigations of laser energy deposition have been conducted with long (nanosecond) laser pulses or ultrashort (femtosecond) laser pulses with a low energy per pulse but tightly focused so as to reach high intensities in the focal region [63–66]. Laser energy deposition may be accompanied by several desired or unwanted physical phenomena such as propagation effects, ionization, single-shot or cumulative heating, generation of shock waves, and cavitation bubbles. Laser parameters, such as the central wavelength, pulse duration and energy, repetition rate, and focusing geometry, may allow for certain control of these phenomena, which is highly desirable for applications. Accurate control, however, requires a deep understanding of propagation dynamics to avoid undesirable effects, especially when the target is located in the bulk of living tissues or aqueous media. With low numerical apertures, ultrashort laser pulses propagating in transparent media are now recognized to undergo strong pulse reshaping due to nonlinear effects[67, 68]. A striking manifestation of this reshaping is supercontinuum generation, as reported with visible [69] and near-infrared (IR) femtosecond pulse propagation in water [70]. The first detailed observations of femtosecond filaments in water were performed with a laser pulse at wavelengths of 527 and 800 nm [71, 72] and further investigated in [73] and [10]. Light-matter interaction during filamentation in water at 800 nm was accessed by time-resolved shadowgraphy [45, 46]. In the visible and near-IR spectral range, laser energy deposition is initiated by multiphoton ionization and the subsequent propagation in the form of a filament involves nonlinear absorption, pulse splitting, supercontinuum generation, conical emission, and beam breakup, among other self-action effects revealed by numerical simulations [24, 74] and experiments [25]. Ultraviolet (UV) light-matter interaction in transparent solids has indicated unexpected filamentation effects [75] including efficient deposition of laser energy to the medium. In the regime of two-photon absorption, this process is sustained

by the quenching of pulse reshaping effects and the formation of a Bessel-like diffraction-free beam [76]. Although many promising applications are foreseen [56, 57, 59–62] , the propagation of intense light pulses in living tissues and in water as a prototypical liquid, as far as medical and industrial applications are concerned, has not been investigated in the UV range, close to the minimum of water absorption.

In this Section, the first detailed experimental and numerical investigation of femtosecond UV laser pulses propagating in water is reported. Measurements, based on a time-resolved imaging technique [three-dimensional (3D) mapping], see Sec. 1.3, not only allow us to characterize the pulse in three dimensions, whatever the complexity of the pulse structure, but also provide us the possibility of following the pulse during its nonlinear propagation, thus giving access to its full 4D (spatiotemporal) evolution. This shows the intimate links between complex propagation effects: pulse splitting into subpulses, conical emission, supercontinuum generation, and transmittance and laser energy deposition for different focusing geometries and submicrojoule pulse energies, backed up by theoretical interpretation guided by numerical simulations.

2.1.1 Experimental setup

The experimental setup is shown in Fig. 2.1.1. An amplified Ti:sapphire laser system (Spitfire PRO; Newport-Spectra Physics), which provides few-milijoule 800 nm with a duration of 130 fs was used. The laser output was divided into two parts by means of a beam splitter. The first part of the split beam was used for filament generation. A suitably attenuated laser pulse (by means of a half-wave plate $\lambda/2$ and a polarizer P) was frequency doubled via second-harmonic generation in a 1-mm-thick β-barium borate crystal (BBO1), which produced an input UV 400-nm, 100-fs pulse with an FWHM beam diameter of 1 mm. Thereafter the input beam was focused on the front window of a water-filled cuvette of tunable length. The front window of the cuvette and the focusing lens L1 were fixed together on the translation stage, thus allowing us to change the length of the cuvette, at the same time, preserving a fixed focal position, while the output window remained unmovable. The energy of the input pulse was varied from 70 nJ to 1 μJ, which corresponded to an input power range from 0.6 to $9P_{cr}$ for which no beam breakup into several hot spots or multiple filamentation was

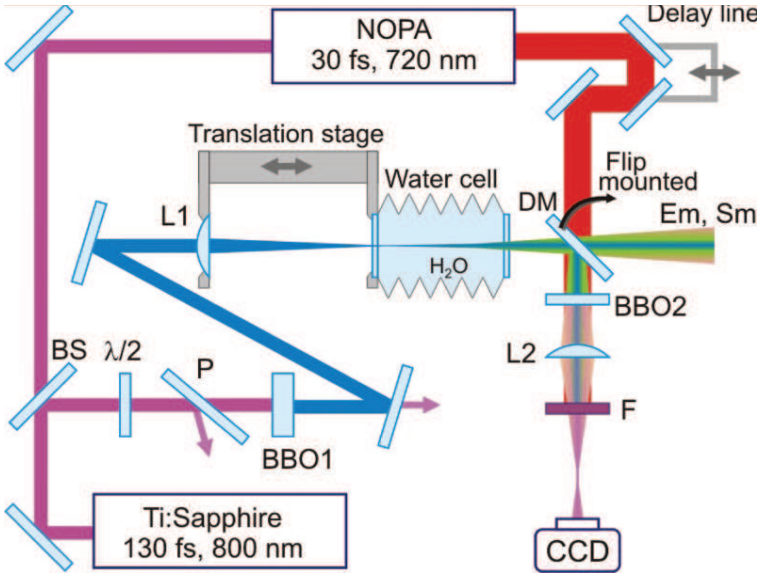

Figure 2.1.1: Experimental setup. BS, beam splitter; P, polarizer; L1, focusing lens (focal length: 50, 200, or 300 mm). BBO1 and BBO2 are β-barium borate crystals used for second harmonic generation producing an input pulse at 400 nm and for difference frequency generation between the filament and the 30-fs reference pulse from the noncollinear optical parametric amplifier (NOPA), respectively. The length of the water-filled cell is variable between 4 and 40 mm. DM, dichroic mirror; Em, energy meter; Sm, spectrometer; F, filter.

observed. The spatiotemporal profile of the pulse at the cuvette output was recorded by means of the 3D mapping technique, see Sec. 1.3. Gate pulse - 30-fs duration, 720 nm central wavelength pulse, generated in a noncollinear optical parametric amplifier (NOPA; Topas-White; Light Conversion Ltd.), which was pumped by the rest of the laser energy. The filament was superimposed with the reference beam by the use of a dichroic mirror, which was mounted on a flipping stage. Specifically, the 3D images of the filament were retrieved by sampling the filament with a short reference pulse by means of difference-frequency generation in a 20-μm-thick β-barium borate crystal (BBO2) cut for type I phase matching. Filter F (RG850) was used to transmit only the difference-frequency signal with a center wavelength of 900 nm, and lens L2 was positioned so as to form a back-image of the difference frequency signal on the CCD camera (JAI A-1). Time delay of the gate (reference) pulse was changed in 10-fs step. Changing the length of the cuvette from 4.5 to 40 mm, i.e., the length of nonlinear propagation z, allowed us to follow the evolution of the pulse along the propagation direction and reconstruct its intensity distribution $I(x, y, t, z)$ in four di-

mensions. The formation of filaments and pulse-splitting events for three focusing geometries (focal lengths of L1: 50, 200, and 300 mm) was characterized, which corresponded to numerical apertures of 0.017, 0.0043, and 0.0028, respectively. In the same setup, by flipping the dichroic mirror, transmission, supercontinuum emission, and conical emission were recorded as functions of the length of the cuvette using a calibrated photodiode with a wavelength sensitivity correcting filter, which served as an energy meter, fiber spectrometer (Sm; QE65000; Ocean Optics), and digital photocamera, respectively. The combined measurements uncover the whole life cycle of ultrashort pulses undergoing filamentation in water at 400 nm.

2.1.2 Dynamical spatial replenishment of the UV filaments

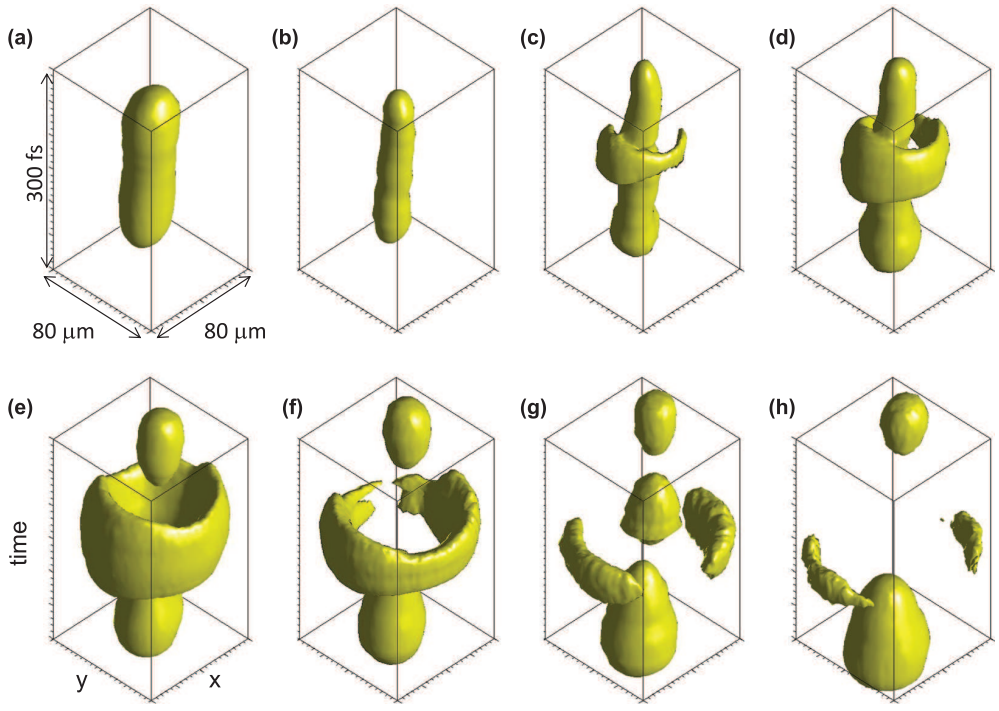

Figure 2.1.2: Measured intensity distributions for a 400-nm, 100-fs laser pulse undergoing filamentation and pulse-splitting events in water. E_{in} = 100 nJ, L1 = 300 mm. Plots show surfaces at intensity levels 20% of the peak intensity for propagation distances of (a) 19 mm, (b) 21 mm, (c) 23 mm, (d) 24 mm, (e) 26 mm, (f) 28 mm, (g) 30 mm, and (h) 32 mm in water. Box size: 80 µm × 80 µm × 300 fs. Propagation direction: from top to bottom.

The first panel in Fig. 2.1.2 shows the 4D reconstruction of the intensity distribution of a 100-nJ pulse propagating in water under loose focusing conditions (L1: 300 mm). The initially ovoid intensity distribution un-

dergoes pulse splitting after propagation over 23–24 mm in water. During the splitting event, a ring is formed in the center of the pulse. The split pulses move away from the center, while the ring rebuilds the axial pulse at $t = 0$ [Figs. 2.1.2(e)–(g)]. Thereafter the whole spatiotemporal formation increases in dimension as a result of diffraction.

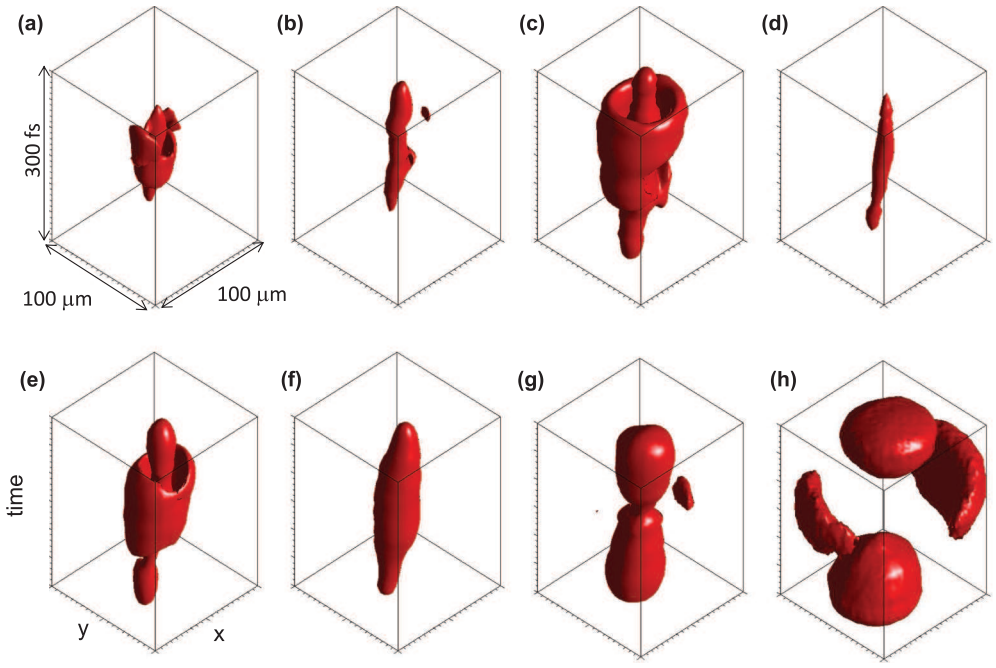

Figure 2.1.3: Measured intensity distributions for a 400-nm, 100-fs, 400-nJ laser pulse undergoing filamentation and pulse-splitting events in water. Focusing geometry L1: 300 mm. Plots show surfaces at intensity levels 20% of the peak intensity for propagation distances of (a) 9 mm, (b) 11 mm, (c) 14 mm, (d) 15 mm, (e) 17 mm, (f) 21 mm, (g) 31 mm, and (h) 33 mm. Box size: 100 µm × 100 µm × 300. Propagation direction: from top to bottom. fs.

Successive multiple splitting events separated by refocusing stages were observed by increasing the input pulse energy. For instance, a 400-nJ pulse under the same focusing conditions undergoes pulse splitting at $z \sim 8\,\text{mm}$, $z \sim 11\,\text{mm}$ and $z \sim 16\,\text{mm}$. The splitting events are best monitored by the presence of a ring-like structure in the central part of the pulse. The split pulses are clearly visible when the leading and trailing pulses separate before the light contained in the ring refocuses on the axis. Figures 2.1.3(a), 2.1.3(c), 2.1.3(e), and 2.1.3(h) clearly show the ring structure, while split pulses are clearly visible in Figs. 2.1.3(e), 2.1.3(g), and 2.1.3(h). Refocusing processes are also clearly monitored in Figs. 2.1.3(b), 2.1.3(d), and 2.1.3(f) between splitting events. Three successive pulse-splitting events were also observed for a pulse with an input energy of 450

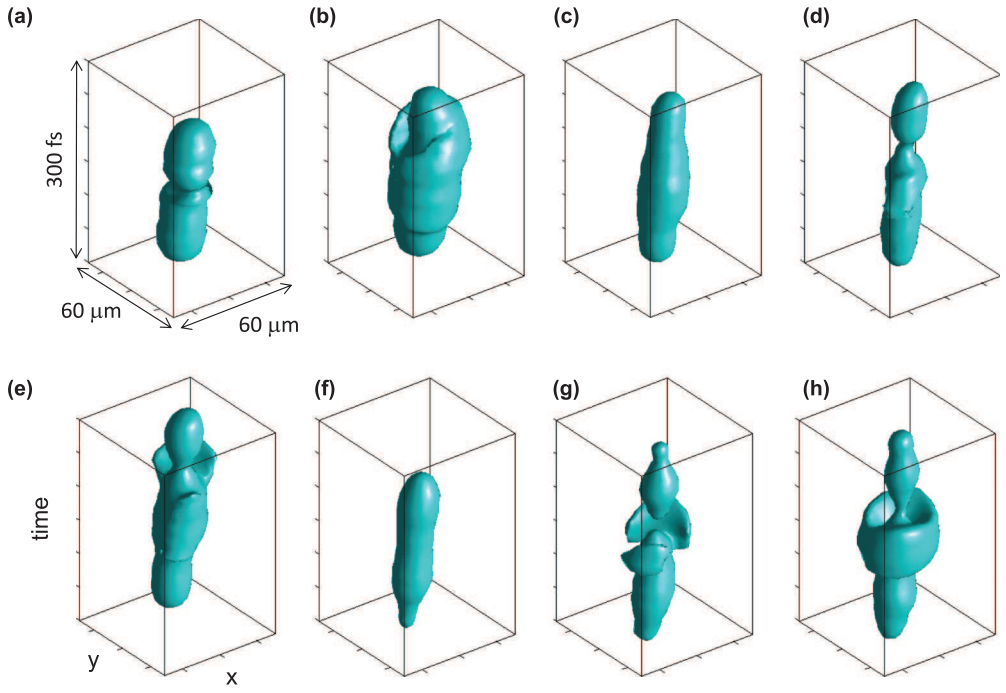

Figure 2.1.4: Measured intensity distributions for a 400-nm, 100-fs laser pulse undergoing filamentation and pulse-splitting events in water. $E_{in} = 450$ nJ; L1, 200 mm; and propagation distances of (a) 8 mm, (b) 9 mm, (c) 10 mm, (d) 12 mm, (e) 13 mm, (f) 16 mm, (g) 17 mm, and (h) 18 mm. Box size: 60 µm × 60 µm × 300 fs. Propagation direction: from top to bottom.

nJ by using a tighter focusing geometry (L1: 200 mm), as shown in Figs. 2.1.4(a), 2.1.4(d), and 2.1.4(g). This temporal dynamics is associated with changes in supercontinuum emission and in conical emission. Splitting events are associated with signatures in the axial spectra, presented in Figs. 2.1.5(A)-(C). After the first splitting event is detected for a length of 8 mm, a strongly red-shifted supercontinuum is generated [Fig. 2.1.5(A)], in contrast with all previous measurements of supercontinuum generation induced by a pulse in the IR or the visible region [3, 69, 70]. After the second splitting event (length of 11 mm), the supercontinuum spectrum becomes modulated and the modulation is particularly pronounced on the red side [Fig. 2.1.5(B)]. The periodic modulation occurs as a result of interference between the primary and the secondary split pulses. After the third splitting event (length of 17 mm), the modulation in the supercontinuum spectrum has beatings contributed by the occurrence of a tertiary split pulse [Fig. 2.1.5(C)]. Figure 2.1.5(D) shows the transitions in the measured supercontinuum for a 450-nJ pulse undergoing filamentation in water. Discontinuities are marked by red-shifted spectral broadening and the appearance

of modulations and beatings, which coincide with splitting events. Very similar, almost-identical spectral features were recorded for pulse energies exceeding the threshold for multiple splitting and for all focusing geometries. They were observed in the far field as well. Figures 2.1.5(a)–(c) show conical emission for a 450-nJ initial pulse loosely focused in water (L1: 200 mm). Figure 2.1.5(a) shows a smooth conical emission pattern after the first splitting event. Previous works reported a self cleaning effect during filamentation in air [77, 78]. Observation of a similar phenomenon in water not only indicates its universality, independently of the medium, but also reveals a nice signature of the elusive temporal dynamics within the filament: conical emission becomes regularly modulated after two splitting events [Fig. 2.1.5(b)] and exhibits irregularly spaced rings after three splitting events [Fig. 2.1.5(c)]. The best visibility of these features was obtained for the smallest numerical aperture of 1/300 and an input energy of 400 nJ.

The 4D mapping of the pulse intensity $I(x, y, z, t)$ enabled us to reconstruct the fluence profile $F(r, \theta, z) \equiv \int I(r\cos\theta, r\sin\theta, z, t)dt$. From this quantity, the beam diameter $D(z) \equiv \langle 2R_\theta(z)\rangle$, defined as the ϑ-averaged FWHM of the fluence distribution, where $R_\theta(z)$ is defined as $F(R_\theta(z), \theta, z) = 0.5F_{\max}(z)$, with $F_{\max}(z) \equiv max_{r,\theta}[F(r, \theta, z)]$, was calculated. Figure 2.1.6 *s*hows the evolution of the beam diameter, output spectrum, and transmitted energy as functions of the propagation distance in water (cuvette length) in the case of loose focusing. These diagnostics exhibit a striking coincidence between beam pinching [transition between focusing and defocusing cycles; see Fig. 2.1.6(a)], the appearance of significant spectral broadening or spectral modulations [Fig. 2.1.6(b)] following the splitting events monitored by the 3D mapping technique, and the sudden decrease in the transmittance [lower (blue)] curve marked by the dips in the absorption rate [upper (red) curve] in Fig. 2.1.6(c). These diagnostics all constitute signatures of pulse-splitting events.

2.1.3 Numerical simulations

In this Subsection only the summary of numerical simulations is provided, detailed results can be found in [79]. The model used for numerical simulations consists of a 3D unidirectional propagation equation with cylindrical symmetry for the nonlinear envelope $E(t, r, z)$ coupled with an evolution equation for the electron density $\rho(t, r, z)$ generated by the high-intensity

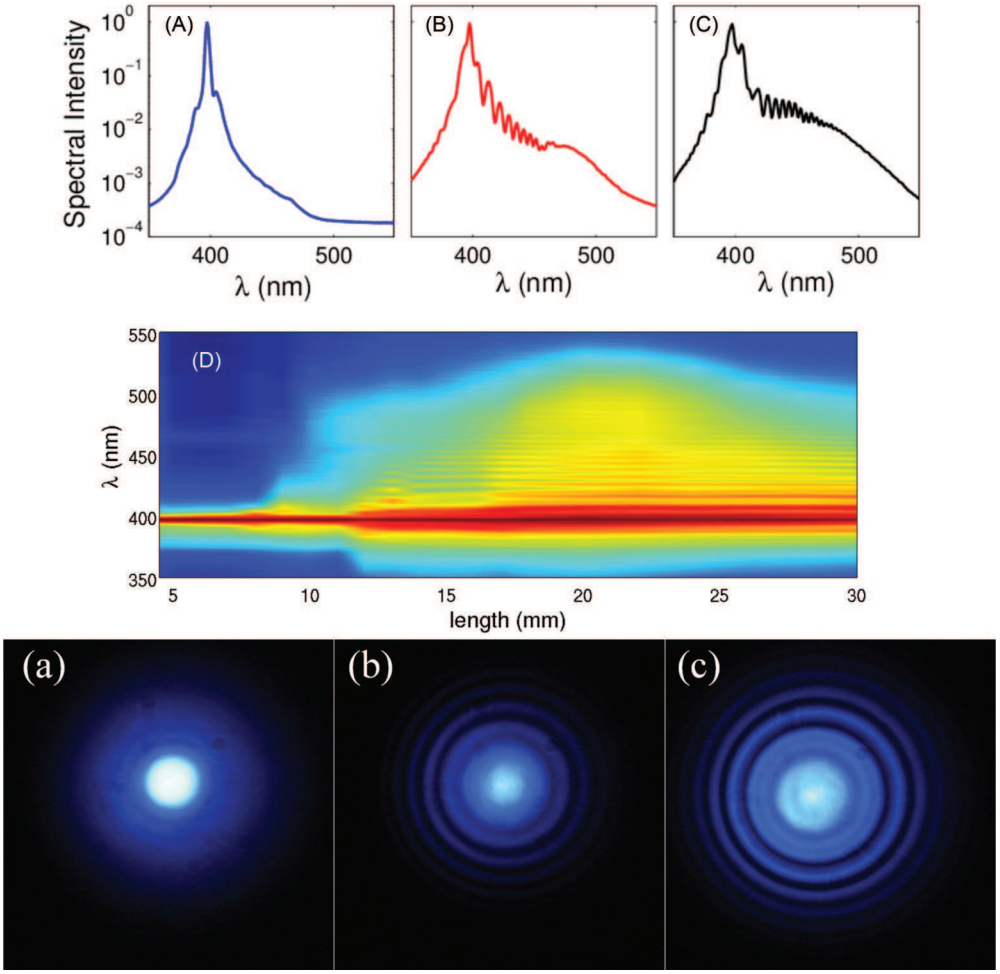

Figure 2.1.5: Supercontinuum spectra (A–C) as a function of propagation distance (D) and conical emission patterns (a–c) for a 450-nJ initial pulse focused in water (L1: 200 mm), showing modulations that appear after splitting events. Propagation distances in water are (A) z = 9 mm, (B) z = 13 mm, (C) z = 17 mm, (a) 12 mm, (b) 14 mm, and (c) 16 mm.

pulse, additionally see Sec. 1.1. The dispersion relation of water is Eq. (3) from Ref. [80]. It must be noted that recent measurements of the Kerr index coefficient in water provided values different from those in Ref. [81], namely, $n_2 = 2.7 \times 10^{-16}\,\mathrm{cm}^2/\mathrm{W}$ at 532 nm in Ref. [82] and $n_2 = 1.7 \times 10^{-16}\,\mathrm{cm}^2/\mathrm{W}$ at 407 nm in Ref. [83]. The best comparison of numerical results with the experiments was obtained for $n_2 = 4.1 \times 10^{-16}\,\mathrm{cm}^2/\mathrm{W}$ [81].

We, finally, justify the use of multiphoton ionization rates rather than the Keldysh formulation, which is considered to be more accurate. The complete Keldysh formulation, represented as the thick black curve, has two distinct asymptotes: the multiphoton limit at low intensity and the tunnel limit at high intensity. The multiphoton limit takes a simple form, $W(I) = \sigma_3 I^3$, which remains indistinguishable from Keldysh's ionization

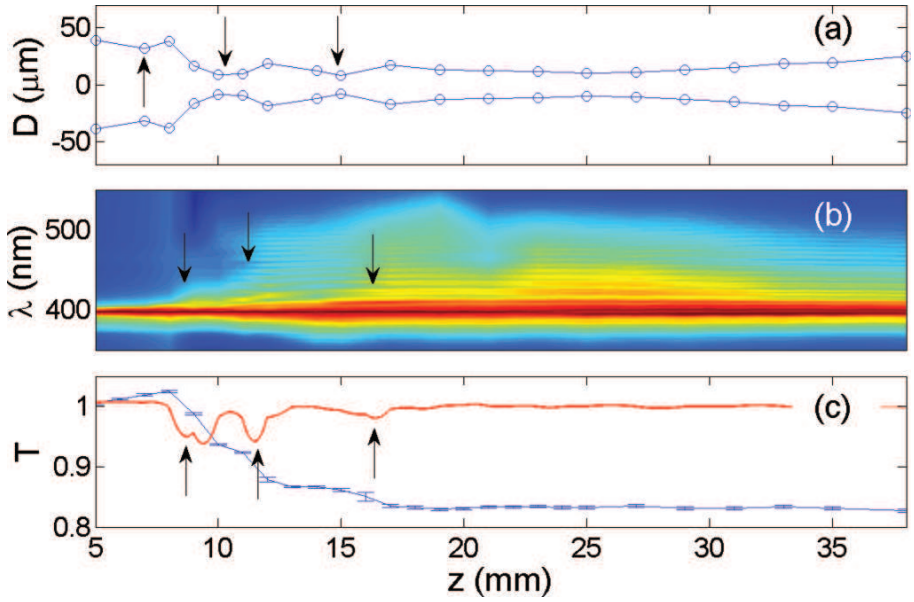

Figure 2.1.6: Typical signatures of pulse splitting for filaments generated in water for loose focusing conditions (L1: 300 mm), a pulse of 400 nm and 100 fs, and $E_{in} = 400\,\mathrm{nJ}$. (a) Beam diameter, (b) supercontinuum, and (c) transmittance as functions of the propagation distance. Arrows indicate a pinching of the beam diameter, significant spectral broadening or the appearance of modulations in the spectrum, and an increase in nonlinear losses (see text for details) that coincide with each pulse-splitting event (z = 8, 11, and 16 mm).

rates for intensities up to $7 \times 10^{13}\,\mathrm{W/cm^2}$. This intensity level is not reached in any of our simulations, therefore, the use of multiphoton ionization rates in our model is fully equivalent to the use of Keldysh's ionization rates.

Under loose focusing conditions (L1: 300 mm) an increasing number of pulse-splitting events is obtained for increasing input energies. The number of pulse-splitting events is in good agreement with the measurements. A striking feature of the splitting dynamics is the quasisymmetric pattern obtained for each splitting event. As in the measurements, splitting events always lead to two split pulses. The leading intensity peak is a superluminal split pulse (it propagates toward negative times) and the trailing peak is a subluminal split pulse (it propagates toward positive times). This quasisymmetry suggests that the main effect responsible for the splitting event is MPA. If plasma defocusing played a stronger role in this dynamics, it would lead to an asymmetry in the splitting process: the leading split pulse would first appear and propagate superluminally. The trailing pulse would appear later, only once the leading pulse decays due to MPA, eventually followed by a refocusing process of a central pulse undergoing the same dy-

namics. This would result in successive splitting events leading to a single pulse rather than two coexisting split pulses at a given distance. The main role of MPA is further confirmed by the fact that spectra were essentially red-shifted after splitting events, whereas plasma defocusing would be responsible for the generation of new frequencies on the blue side of the laser spectrum.

The maximum intensity of the pulses does not exceed $6 \times 10^{12}\,\mathrm{W/cm^2}$, justifying that multiphoton ionization rates coincide with the complete Keldysh formulation. The maximum electron density always remains below $10^{19}\,\mathrm{cm^{-3}}$ and exceeds $10^{18}\,\mathrm{cm^{-3}}$ only in very localized regions. Although the lowest local refractive index change due to this plasma density is approximately -5×10^{-4}, a value nearly opposite to the refractive index change induced by the Kerr effect at the highest intensity, the defocusing effect of the plasma is delayed with respect to the peak intensity and therefore can only affect the trailing part of the pulse. In contrast, MPA is an instantaneous effect acting on the intense part of the pulse and leads to quasisymmetric splitting events when it is the key player.

In order to find the difference in the pulse dynamics induced by plasma defocusing versus by MPA, simulations for the same parameters were performed but with the value of the nonlinear index coefficient corresponding to the latest measurement [83] and the pulse energies increased to obtain roughly the same number of splitting events as in the measurements. The first important difference is that the energy range necessary to reproduce these splitting events is significantly higher than that of the measurements. The second difference concerns the asymmetry in the splitting events. Except for the lowest energy of 1 μJ, higher energy pulses do not exhibit two split pulses at a given propagation distance, but a single leading or trailing pulse with a possible pedestal. Such extreme situations were not found in our measurements. In these asymmetric cases, plasma defocusing is interpreted as playing a more important role in the splitting events, as also suggested by the longer plasma channels. In summary, the number of pulse-splitting events, the shape of the split pulses, and their quasisymmetry are best reproduced by our numerical simulations performed with the nonlinear index coefficient $n_2 = 4.1 \times 10^{-16}\,\mathrm{cm^2/W}$ [81]. The good matching of the positions of simulated and measured symmetric splitting events indicates that the plasma does not play an important role in the splitting dynam-

ics, in keeping with the fact that plasma-induced self-phase modulation would have led to a blue-shifted supercontinuum, whereas measurements have shown a marked red shift.

From the observations and guided by the simulation results, we interpret the respective roles of MPA and plasma defocusing in the pulse-splitting dynamics. In addition to the good agreement for the propagation distances between splitting events, a striking feature of the splitting dynamics is the systematic presence of two split pulses, both in measurements and in simulations. At IR wavelengths, plasma defocusing quickly quenches the trailing pulse and its visibility ceases at longer propagation distances [84]. For UV wavelengths, our results suggest that the main effect responsible for a splitting event is MPA, which acts as a distributed stopper along the propagation axis, both reducing the intense peak in the central part of the beam and generating a ring-like diffraction pattern, as observed in our measurements. The prevailing role of MPA is compatible with the spatial replenishment of the pulse central part [85], since the effect of a stopper is followed by a beam reconstruction similar to that occurring in the Arago spot experiment [17, 18]. Transmittance measurements in Fig. 2.1.6 also confirm the crucial role of MPA. The plasma generated by the leading split pulse induces defocusing and could also lead to ring formation. However, the systematic observation of coexisting split pulses with nearly the same peak intensity indicates that plasma defocusing does not induce any delay in the formation of the trailing split pulse and therefore plays only a secondary role in the pulse-splitting mechanism. It was also established that the combined effects of plasma defocusing and pulse self-steepening induce a significant spectral broadening toward shorter wavelengths [12]. Our measurements show the opposite, i.e., spectral broadening toward the longer wavelengths in the visible region,interpreted as resulting from a steep pulse leading edge, in keeping with a dominant role of MPA [86]. The main role of MPA is further confirmed by the the fact that spectra were essentially red-shifted after splitting events, whereas plasma defocusing, in conjunction with self-steepening, would be responsible for the generation of new frequencies on the blue side of the laser spectrum.

2.1.4 Measurements for tighter focusing conditions

Splitting events were also observed for tighter focusing conditions (L1: 50 mm), although with clearly different and more complex reshaping features (Fig. 2.1.7). For the same pulse energy, after a splitting event, bright rings with a nice revolution symmetry are more visible at loose focusing. With the shortest focal length (50 mm), the generic spectral broadening, spectral modulations, and submodulations are retrieved by increasing the pulse energy [see Figs. 2.1.7(a)– (c)]. The temporal and spectral pulse dynamics is therefore not quenched for tighter focusing conditions, leading to similar signatures of laser energy deposition and pulse splitting (see intensity distributions in Fig. 2.1.7) as in the case of loose focusing conditions.

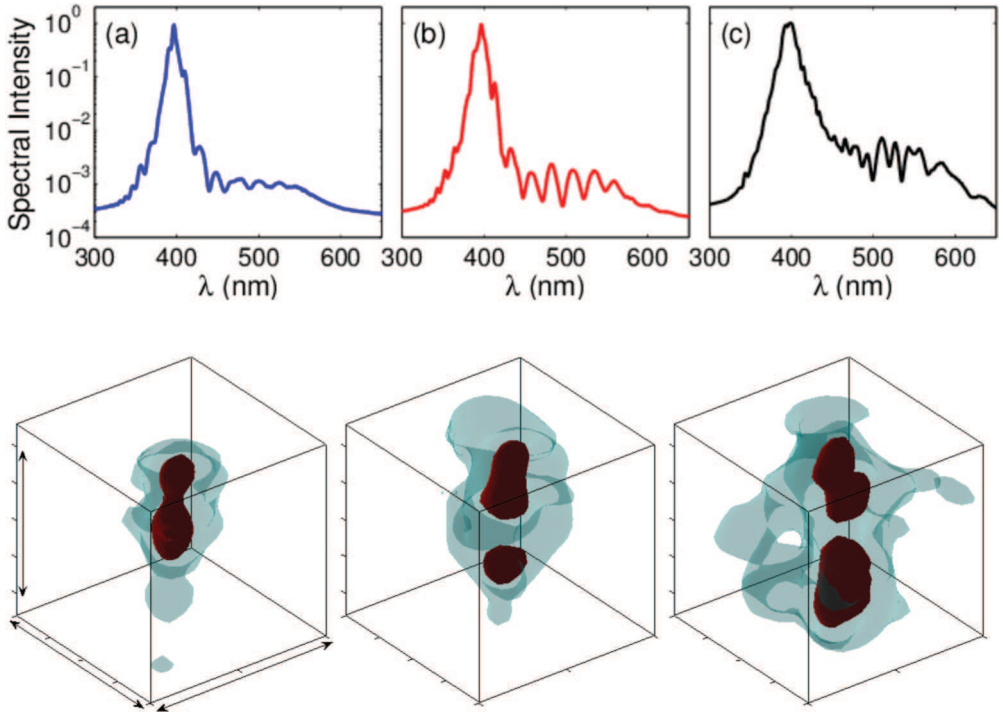

Figure 2.1.7: Comparison of supercontinuum spectra (first row) and 3D mapping of the pulse intensity distribution (second row) after propagation in water over 12 mm of a 400-nm pulse focused with L1 = 50 mm. Pulse energy: (a) 300 nJ; (b) 400 nJ; (c) 900 nJ. Lighter (blue) and darker (red) isosurfaces correspond to isointensities equal to 30% and 50% of the maximum intensity, respectively. Propagation direction: from top to bottom. Scales indicated by arrow lengths: 40 μm × 40 μm × 200 fs.

2.1.5 Conclusions

In conclusion, the complete dynamics of ultrashort laser pulses undergoing filamentation in water at 400 nm was carefully characterized. The transitions in the complex filamentation dynamics were monitored involving space-time couplings with recurrent pulse splitting when the focusing geometry is changed from loose to tighter focusing. Filaments were observed at focusing geometries from $NA \sim 3 \times 10^{-3}$ to $NA \sim 2 \times 10^{-2}$. Intensity maps in space and time at different pulse energies were recorded, for a range of propagation distances where relevant nonlinear events occur. Transmission, conical emission, and spectral broadening data were simultaneously recorded and the observed space-time transformations of the pulse were connected to specific signatures in transmission curves and spectra. From a solely practical point of view, the supercontinuum spectra and conical emission patterns allow us to easily identify pulse-splitting events without employing a complex experimental apparatus and could be readily used for online monitoring of filamentation dynamics. Pulse splitting was observed in all cases. Low numerical apertures lead to deposition of laser energy in localized nonlinear foci over an elongated focal region, associated with the occurrence of one or several pulse-splitting events depending on the pulse energy. The first event follows a significant nonlinear absorption and is associated with the generation of a smooth, red-shifted supercontinuum and smooth conical emission pattern. Subsequent splitting events consume less energy and induce modulations in supercontinuum spectra and conical emission. Tighter focusing geometries lead to shorter focal regions. Measurements compare favorably with predictions of the dynamic spatial replenishment model [85] and simulation results, indicating a transition in the nature of pulse splitting featuring a prevailing role of MPA when the laser wavelength is changed from the IR to the UV region. These results disclose the missing links between a wealth of nonlinear phenomena, which govern the complex space-time dynamics of intense laser pulses propagating in water (and, more generally, in transparent dielectric media) and provide a substantial advance in our understanding of femtosecond laser energy deposition in liquid media. This knowledge is of critical importance for a range of practical applications relying on laser-induced cavitation and its control and constitutes a cornerstone in the general development of non-intrusive methods for femtosecond laser surgery, in particular.

2.2 Light bullets by the filamentation in the anomalous GVD regime

The pursuit for three-dimensional light bullets considers two essentially different physical concepts. The first is based on the generation of spatiotemporal solitons, which could be regarded as ideal light bullets with rapidly (exponentially) decaying tails, constituting a high degree of energy localization. Formation of the spatiotemporal soliton relies on simultaneous balancing of diffraction and dispersion by nonlinear effects, such as self-focusing and self-phase modulation [87]. In the first approximation, these conditions could be met in media with Kerr nonlinearity in the anomalous group velocity dispersion (GVD) range [87]. However, the proposed light bullet is a three dimensional extension of the universal Townes profile, therefore possessing similar properties: it forms only at the nonlinear focus [88], and is modulationally unstable [89]. Therefore, for achieving a spatiotemporal invariant propagation, linear and nonlinear optical properties of the medium must be suitably tailored, see e.g. [90–94], thus raising difficult technological challenges. So far, to the best of our knowledge, experimental demonstration of truly three dimensional light bullets was reported only in a two-dimensional array of coupled waveguides featuring quasi-instantaneous cubic nonlinearity and a periodic, transversally modulated refractive index [95].

The second concept for achieving light bullets is based on the precise tailoring of the input wave packet so as to match the material properties, without the need for optical nonlinearities, i.e. defeating the natural diffractive spreading and dispersive broadening in the linear propagation regime. Linear light bullets are non-solitary, weakly localized wave packets, whose stationary propagation is achieved due to Bessel-like profile of the beam, whose spectral components are distributed over certain propagation cones, so as to continuously refill the axial part, which contains an ultrashort pulse. Moreover, this approach is equally effective in media with normal, as well as anomalous GVD. To this end, non-solitary, weakly localized spatiotemporal linear light bullets have been experimentally demonstrated in the form of the X-waves [96], Airy bullets [97, 98] and ultrashort-pulsed Bessel-like beams [99]. However, practical realizations of the linear light bullets require precise control of propagation angles and phases of the spectral components,

and therefore intricate experimental techniques.

A much more straightforward route for achieving nonsolitary, weakly localized light bullets is based on self-reshaping of the entire wave-packet (ultrashort pulsed laser beam) by means of nonlinear effects, producing the nonlinear analogs of the X-waves [22, 100] and Airy bullets [101]. In particular, spontaneous formation of the nonlinear X-waves was demonstrated by means of femtosecond filamentation in transparent dielectric media, where the input Gaussian-shaped wave packet self-adjusts its spatiotemporal shape via nonlinear effects into a specific spatiotemporal X shape, which maintains its stationarity even in the presence of the nonlinear losses [24, 25, 84]. However, pulse splitting which occurs during filamentation of intense femtosecond pulses in the normal GVD regime [3], prevents formation of a single X wave.

Conversely, studies of filamentation in the conditions of anomalous GVD predicted the generation of isolated spatially and temporally compressed pulses [102–107]. Recent investigations have uncovered a filamentation regime, in which quasi-stable three-dimensional non-spreading pulses are generated [108]. However, there remain relevant unanswered questions regarding the interpretation of these light bullets. In this Section it is explicitly demonstrated that the light bullets generated by self-focusing of femtosecond-pulsed beams in bulk dielectric media with instantaneous Kerr nonlinearity and anomalous group velocity dispersion are polychromatic Bessel-like wavepackets, which bear the basic properties of the nonlinear O-waves [109], as verified by simultaneous measurements of spatiotemporal profiles, frequency-resolved angular spectra, near field intensity distributions, linear and nonlinear propagation features and energy density flux.

2.2.1 Experimental setup

The experiment was performed using 90 fs Gaussian pulses with center wavelength of 1.8 µm from a commercial, Ti:sapphire laser system-pumped optical parametric amplifier (Topas C, Light Conversion Ltd.). Its output beam (an idler wave, in present case) was suitably attenuated, spatially filtered and focused by an $f = +100\,\mathrm{mm}$ lens into 45-µm (FWHM) spot size which was located on the front face of the nonlinear medium (sapphire sample). The input pulse energy of 3.1 µJ (corresponding to $3.4P_{cr}$, where

P_{cr} = 10 MW is the critical power for self-focusing in sapphire) was set so as to induce a light filament, which formed after 4 mm of propagation, as verified by the supercontinuum emission in the visible spectral range. The spatiotemporal intensity distribution at the output of sapphire sample was measured by three-dimensional imaging technique, see Sec. 1.3s. More specifically, the output beam was imaged (with 5× magnification) onto a 20-µm-thick beta-barium borate crystal and gated by means of broadband sum-frequency generation with a short, 25-fs pulse with central wavelength of 720 nm from a noncollinear optical parametric amplifier (Topas-White, Light Conversion Ltd.), which was pumped by the second harmonic of Ti:sapphire laser system. The cross-correlation signal with center wavelength of 515 nm was then imaged (with 1.8× magnification) onto the CCD camera (Grasshopper 2, Point Grey) with a pixel size of 4.4 µm and 14-bit dynamic range. By changing the time delay of the gating pulse in a 8-fs step, a sequence of cross-correlation images was acquired, which afterward were merged together to reproduce the entire spatiotemporal intensity distribution of the light bullet. For simplified experiment setup see Fig. 2.2.1

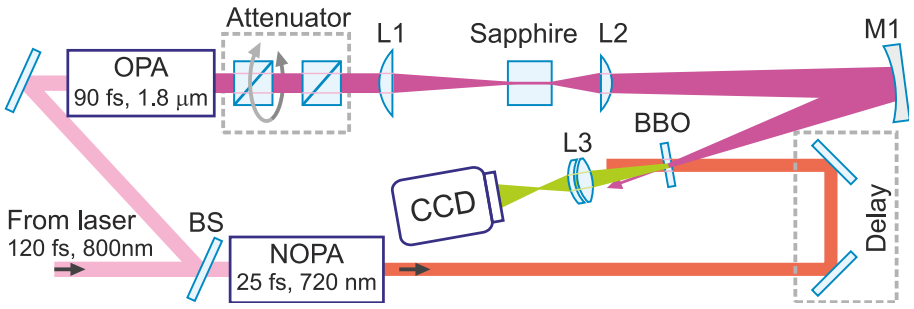

Figure 2.2.1: Experimental setup.

2.2.2 Light bullets as polychromatic Bessel-like beams

Evolution of the spatiotemporal intensity distribution over propagation distance z was captured by placing sapphire samples of different lengths in such a way, that the output face of the sample was always kept at the same fixed position, while moving the focusing lens accordingly, to ensure the location of the input focal plane at the front face of the sample. Figure 2.2.2 presents the spatiotemporal intensity profiles of the wave-packet as measured at various propagation distances in sapphire, showing how the input Gaussian wave-packet transforms into a spatially and temporally compressed three-

dimensional light bullet. Over the first few mm of propagation, the input Gaussian beam shrinks due to self-focusing and the input Gaussian pulse experiences self-compression due to the interplay between self-phase modulation and anomalous GVD. After the nonlinear focus ($z = 4.2\,\mathrm{mm}$), the wave-packet transforms into a spatially and temporally compressed three-dimensional light bullet, which has FWHM diameter of 15 μm and pulse duration of 40 fs, as evaluated from the deconvolution of the on-axis cross-correlation function. High dynamic range measurements reveal that the light bullet consists of a sharply localized high-intensity core, which carries the self-compressed pulse and a low-intensity, ring shaped spatiotemporal periphery, and propagates without an apparent change of its spatiotemporal shape. Propagation dynamics of the light bullet are summarized in Fig. 2.2.3, where full circles show the beam width and pulse duration versus propagation distance, demonstrating that high intensity core maintains its localization over more than 10 mm of propagation, that exceeds 25 Rayleigh ranges, as calculated for the Gaussian beam of equivalent dimensions.

In a further experiment, where the light bullet after 6 mm of propagation in sapphire was thereafter let to propagate in free space (air), interesting and very important propagation features were recorded. Gradual increase of both, spatial and, more importantly, temporal dimensions of the central core was observed, as the propagation distance in free space increases, as shown by open circles in Fig. 2.2.3. These data are compared with the calculated linear evolution of a strongly localized Gaussian wavepacket with identical spatial and temporal dimensions (shown by the dashed curves), which represent the expected spreading of a soliton-like object in free space. The distinctive differences in free space propagation between the present light bullet and a soliton-like object are immediately clear: the diffraction spreading of the bullet is almost 5 times less than that of a Gaussian-shaped beam, and its temporal width increases by a factor of 1.3, just after 3 mm of propagation, in the absence of dispersion, while for a soliton-like object it is expected to remain constant. These results demonstrate that the light bullets, as they exit the nonlinear medium, exhibit sub-diffractive and dispersive propagation in free space, that is incompatible with the behavior of highly localized spatiotemporal soliton-like objects. The linear and nonlinear propagation features of the light bullets arise from dramatic spatiotemporal reshaping of the input Gaussian wave-packet and resulting strong space-time coupling,

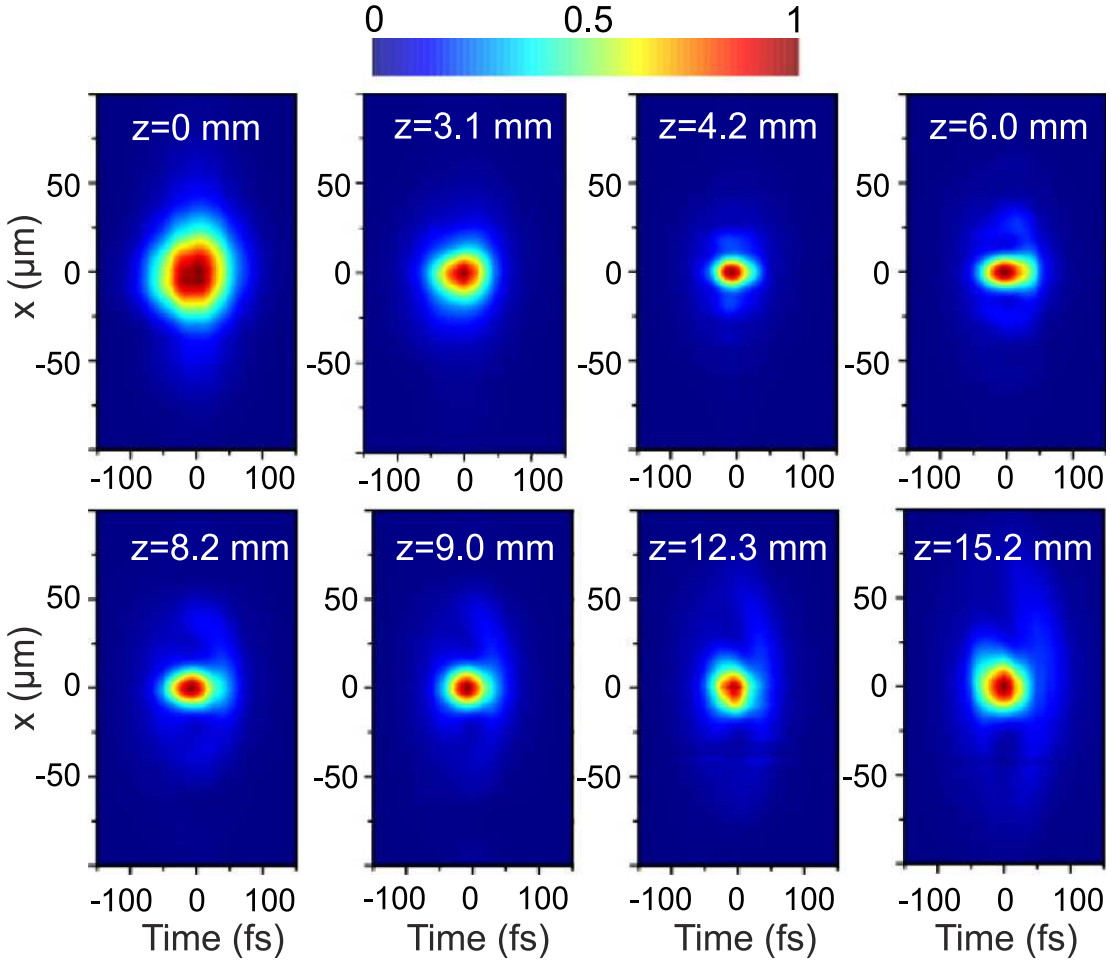

Figure 2.2.2: Spatiotemporal intensity distributions of self-focusing Gaussian wave-packet, which transforms into a light bullet, as measured at various propagation lengths z in sapphire: (a) z = 0 mm, (b) z = 3.1 mm, (c) z = 4.2 mm, (d) z = 6.0 mm, (e) z = 8.2 mm, (f) z = 9.0 mm, (g) z = 12.3 mm, (h) z = 15.2 mm.

which is a distinctive property of conically-shaped wave packets [26].

In the support of this claim, the relevant characteristics of the light bullet in more detail were studied. Figure 2.2.4 illustrates the spatial profiles of the input Gaussian beam and the light bullet, as recorded at different propagation distances in sapphire, and obtained by time integration of spatiotemporal profiles presented in Fig. 2.2.2. The spatial profiles are presented in logarithmic intensity scale and reveal an intense central core, which contains approximately 25% of the total energy and is surrounded by a low-intensity concentric ring-shaped periphery, thus resembling a distinct Bessel-like intensity distribution, which emerges from the interplay of self-focusing, nonlinear absorption and diffraction [17]. A Bessel-like intensity distribution of the light bullet explains the spatial features of the central

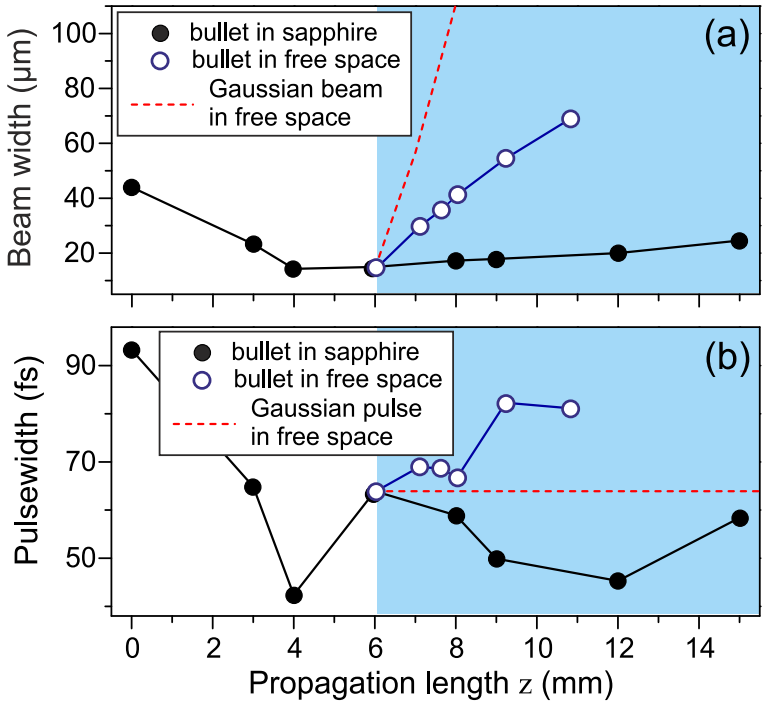

Figure 2.2.3: Evolution of (a) beam FWHM diameter and (b) pulsewidth versus propagation distance. Full circles show formation and propagation dynamics of the light bullet in sapphire, as summarized from Fig. 2.2.2. Open circles show propagation of the light bullet in free space (air), which starts at z = 6 mm. Dashed curves indicate the expected free-space propagation features of a strongly localized Gaussian wave packet.

core observed in the experiment: its robustness during the nonlinear propagation in sapphire, as well as sub-diffractive propagation in free space, which are achieved via energy refilling from the beam periphery [17, 18].

Figure 2.2.5 highlights the characteristic spatiotemporal properties of the input wave packet and the light bullet. Figs. 2.2.5(a)-(c) compare the near-field (r,t) spatiotemporal intensity profiles in logarithmic intensity scale, so as to better visualize the entire spatiotemporal structure of the light bullet. Figures 2.2.5(d)-(f) present the corresponding angularly resolved (θ, λ) spectra, as measured by scanning the far-field (at 25 cm distance from the exit face of sapphire sample) with a 200-μm fiber tip of a fiber spectrometer (AvaSpec-NIR256-2.5, Avantes). The angularly resolved spectra suggest the occurrence of an elliptical, or O-shaped, pattern of conical emission, that is expected from Kerr-driven spatiotemporal instability gain profile in the case of anomalous GVD [10, 110].

The near and far field intensity profiles are combined together to obtain

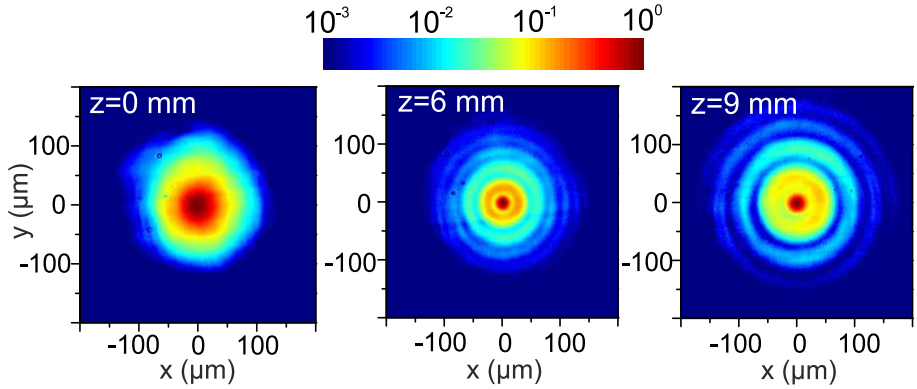

Figure 2.2.4: Spatial profiles of (a) the input beam at z = 0 mm and the light bullet at (c) z = 4.2 mm, (d) z = 6.0 mm, (e) z = 9.0 mm.

the full spatio-temporal phase profile of the light bullets by means of an iterative Gerchberg-Saxton retrieval algorithm, see [111] for details. The gradient of the retrieved phase profile is used to explicitly visualize the transverse energy density flux in the full spatial and temporal coordinates, as shown normalized in Figs. 2.2.5(g), (h) and (i), along with overlayed contour plot of the retrieved intensity profiles. Here the color coding is the same as in [112], where blue and red colors indicate downward and upward fluxes with respect to the vertical axis, respectively.

The transverse energy density flux of the light bullet [Fig. 2.2.5(h), (i)] indicates a radially symmetric pulse front tilt resulting from strong space-time coupling, and the spatiotemporal distribution of the currents is almost identical to that of a stationary, polychromatic Bessel beam with subluminally propagating envelope peak [112], as schematically depicted in Fig. 2.2.6. The established subluminal propagation of the envelope peak is very much in line with the results of numerical simulations in fused silica [14, 108], where the position of the peak is shown to continuously shift toward positive times with propagation. The radially symmetric pulse-front tilt, which owes to angular dispersion [113], explains the observed features of temporal behavior of the light bullet in the nonlinear and linear (free space) propagation regimes, as illustrated Fig. 2.2.3(b). The propagation angles of the spectral components comprising the light bullet compensate for material dispersion in dispersive medium, whereas such angular distribution causes the dispersive spreading of the pulse, as the bullet exits the dispersive medium and propagates in free space. In addition, presence of the pulse-front tilt may readily explain the reported pulsewidth dependence on

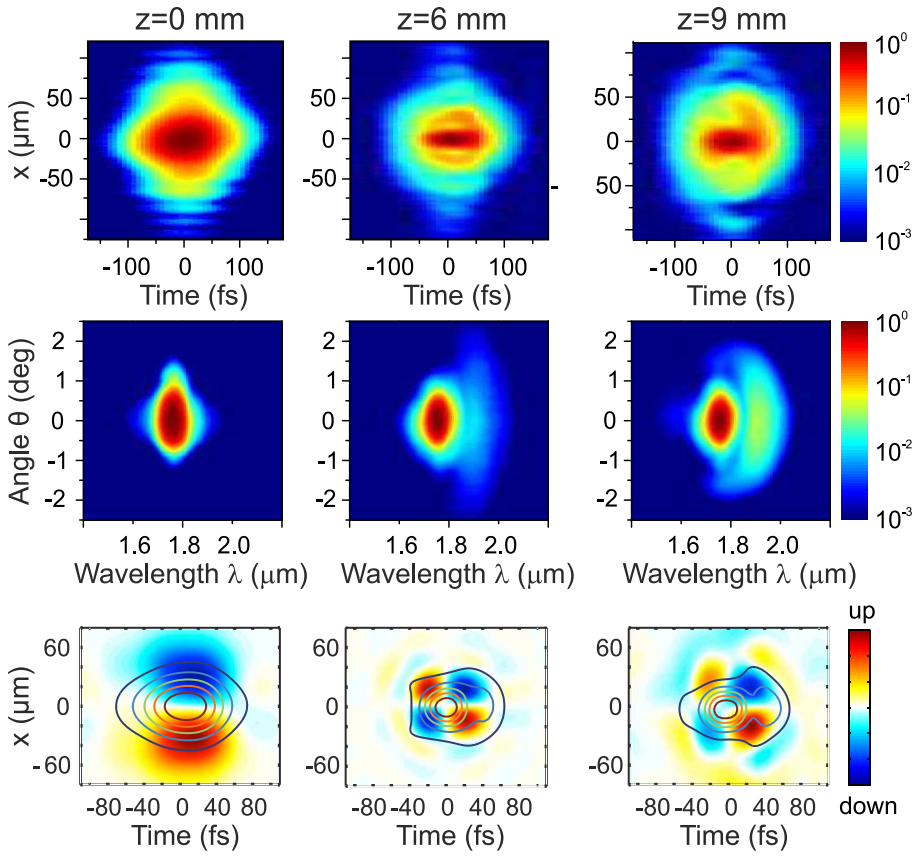

Figure 2.2.5: Spatiotemporal intensity profiles (shown in logarithmic intensity scale) of (a) the input wave packet, and the light bullet at (b) z = 6.0 mm, (c) z = 9.0 mm. (d), (e) and (f) show the corresponding angularly resolved spectra. (g), (h) and (i) show the corresponding retrieved transverse energy fluxes, see text for details.

the aperture size in the autocorrelation measurements [107]. It must be underlined that a soliton or soliton-like wavepacket would be expected to exhibit a flat phase and hence no transverse energy density flow in the spatiotemporal domain. Conversely, the conical flux unveiled here is inherent to polychromatic Bessel-like pulses and hence serves as unambiguous demonstration of the nature of the light bullets generated by self-focusing in a bulk dielectric media with anomalous GVD. More precisely, the entirety of established properties of the bullet: quasistationary O-shaped spatiotemporal intensity profile and characteristic angularly-resolved spectrum, Bessel-like spatial intensity distribution and transverse energy flux along with nonlinear and linear (free-space) propagation features closely resemble those of the nonlinear O-waves featuring weak losses and subluminally propagating envelope peak [109].

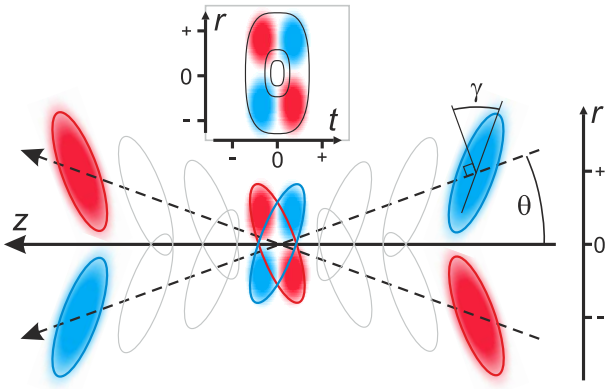

Figure 2.2.6: Schematic representation of transverse energy flux in ultrashort-pulsed (polychromatic) Bessel beam with subluminally propagating envelope peak. ϑ and γ are arbitrary cone and pulse-font tilt angles, respectively.

2.2.3 Conclusion

In conclusion, the nature of three-dimensional light bullets generated from self-focusing of intense femtosecond pulses in bulk dielectric media with anomalous GVD was uncovered. Self-focusing dynamics of 100 fs pulses at center wavelength of 1.8 µm in sapphire was experimentally captured in detail in full four-dimensional (x,y,z,t) space by means of three-dimensional imaging technique. It was demonstrated that the emerging three-dimensional light bullets consist of a sharply localized high-intensity core, which carries the self-compressed pulse and a weak, delocalized low-intensity periphery, comprising a Bessel-like beam. Also it was demonstrated that the seemingly weak periphery as viewed in linear intensity scale, is nonetheless an important integral part of the overall wave packet, as it continuously balances energy losses in the central core and prevents it from spreading during its linear and nonlinear propagation. It was disclosed that spatiotemporal reshaping of the input Gaussian wave packet results in development of a very distinct spatiotemporal flow of the energy that is not compatible with a spatiotemporal soliton, but rather finds a natural explanation in terms of a polychromatic Bessel beam, which could be qualified as a nonlinear O-wave which has weak losses and subluminally propagating envelope peak [109]. As a consequence of this, the light bullets exhibit a rather remarkable behavior as they exit the sample and propagate in free space (air), i.e. in the absence of any nonlinear or dispersive effects: the bullets disperse temporally, yet continue to propagate with strongly suppressed diffraction. It is expected that these important features are characteristic to an entire

family of spatiotemporal light bullets, which are generated by femtosecond filamentation in bulk dielectric media with anomalous GVD and should be carefully accounted for building the basis for diverse future applications that may require a simple setup for creating intense, temporally compressed and sub-diffractive wave packets [32].

3 Supercontinuum generation

Material related to this chapter was published in [A3, A4, A6, A7]

Ever since the first observation in 1970 [114], supercontinuum (SC) generation in bulk dielectric media has been explored and has proved to be an indispensable tool in ultrafast spectroscopy, laser physics, and nonlinear optics [115, 116]. An extremely broad spectrum and high spatial and temporal coherence and thus compressibility and focusability are the basic defining properties of ultrafast SC. These features along with excellent shot-to-shot reproducibility, which is achieved under proper pumping conditions, make femtosecond SC an attractive source for seeding the ultrashort pulse optical parametric amplifiers [117, 118] and small to-medium scale OPCPA systems [119]. With the advent of femtosecond lasers, extensive numerical and experimental studies of SC generation were carried out in liquid- and solid-state dielectric media [7, 69, 120–128]. These studies revealed wide bandgap solids, such as fused silica, fluorides, sapphire, and other laser host materials, as the most attractive media for SC generation. A typical setup for SC generation in a bulk medium is amazingly simple; it consists of an optional attenuator for input-pulse energy control, a short focal distance lens, and a thin (typically of few millimeters thickness) nonlinear medium. When choosing proper focusing of the input Gaussian beam, which establishes an operating condition below the optical damage threshold [129, 130], that simple setup produces broadband and coherent radiation with smooth spectral intensity and high shot-to-shot reproducibility. Despite the experimental simplicity, the physics behind SC generation remains one of the most disputed topics in modern ultrafast nonlinear optics. The threshold for SC generation nearly coincides with that for self-focusing and filamentation [3]; in most operating conditions, the occurrence of the SC justifies the occurrence of a light filament, and vice versa. The broadband radiation emerges from a complex interplay among a number of relevant physical effects: self-phase modulation [120], four-wave mixing [69], pulse splitting [131, 132],

pulse-front steepening and generation of optical shocks [12], multiphoton absorption, and free electron plasma generation [7, 70].

In the regime of normal group velocity dispersion, these effects lead to dramatic reshaping of the intense input pulse, which undergoes temporal compression, pulse-front steepening and eventually splits into two, leading and trailing subpulses, which are responsible for red- and blueshifted spectral broadening, respectively [12]. For instance, in sapphire, which is one of the most popular nonlinear medium for SC generation, under typical operating conditions (with $\sim 100\,\mathrm{fs}$, $800\,\mathrm{nm}$ input pulses provided by commercial Ti:sapphire laser systems and tight focusing into short, few millimeter-long samples of the nonlinear media), the SC spectrum exhibits a marked asymmetry with respect to carrier wavelength, with dominating blueshifted spectral components, see, e.g., [117, 128, 133, 134]. It is well known that in general, the maximum attainable blueshift scales approximately as $E_g/\hbar\omega_0$, where E_g is the medium bandgap, $\hbar\omega_0$ is the pump photon energy and ω_0 is the carrier frequency of the pump [70] . The bandgap dependence is explained in terms of the intensity clamping of the intense trailing sub-pulse imposed by the multiphoton absorption and electron plasma defocusing [7, 16], and chromatic dispersion of the material [74, 125]. While strong blueshifted spectral broadening is associated with the development of an intense trailing subpulse, a much weaker leading subpulse is responsible for the occurrence of the redshifted spectral components.

Filamentation phenomena find a broad spectrum of applications, ranging from atmospheric analysis [29] to laser micromachining [31], and therefore the stability issues of the filaments are of primary importance. However SC does not always exhibit good shot-to-shot reproducibility and in some cases the statistics of SC intensity obey to extreme-value statistics. Rogue or extreme events (frequently termed rogue waves) are rare high-amplitude events, observed in various physical systems, where nonlinear wave interactions take place, see [135] for a review. The occurrence probability of rogue events is described by so-called extreme-value or heavy-tailed (L-shaped) statistical distribution, which suggests that events with very high amplitude (as compared to the mean value) occur much more frequently than could be expected from normal-value (Gaussian) statistics. A considerable progress in understanding the rogue waves in hydrodynamics and optics has been achieved thanks to close analogy between the underlying physical

mechanisms that initiate rogue wave formation [136, 137]. Optical rogue waves [138] are extensively studied in one-dimensional optical systems, i.e. photonic crystal fibers, where nonlinear light propagation gives rise to complex temporal behavior and spectral superbroadening. Here optical rogue waves manifest themselves as high amplitude red-shifted soliton pulses [138] and blue-shifted dispersive waves [139] that emerge from noise-seeded modulation instability, with soliton collisions identified as the main mechanism responsible for rogue wave formation [140]. The rogue-wave-like behavior in optical fibers was observed with different pulsewidths, ranging from continuous wave to picosecond and femtosecond pulses [141–143], and under a variety of operating conditions [144–146].

Rogue or freak waves are well known in hydrodynamics, referring to statistically rare giant waves that occur on the surface oceans and seas, see for instance [147] for a review. From a general point of view, rogue waves, or more generally, rogue (extreme) events represent an extreme sensitivity of the nonlinear system to the initial conditions. Indeed, recently rogue-wave-like behavior was shown to be inherent to diverse nonlinear physical environments: propagation of acoustic waves in superfluid helium [148], variation of local atomic density in Bose-Einstein condensates [149], ion-acoustic and Alfvén wave propagation in plasmas [150], and propagation of acoustic-gravity waves in the atmosphere [151].

Optical rogue waves, recently discovered by Solli et al. [138] constitute a fascinating topic in modern nonlinear optics [152, 153].. At present, most of the knowledge on optical rogue waves is brought by the studies of the supercontinuum generation in optical fibers, under a variety of operating conditions and propagation regimes, ranging from CW to femtosecond pulses [139–142, 144, 154, 155] and had been shown to share a great similarity with their hydrodynamical counterparts [137]. In fibers, rogue waves represent rare soliton pulses, whose statistics are characterized by extreme-value (non-Gaussian or, more specifically, L-shaped) distributions. It is generally accepted that optical rogue waves emerge as a result of the nonlinear wave interactions and soliton collisions, although the precise underlying physical mechanisms leading to their formation are still under debate [156]. More recently, rogue wave-like behavior was observed in bulk media, in the femtosecond filamentation regime in gasses (air) [157] and liquids (water) [158] and predicted to occur in even more complex regimes of propagation,

such as multiple filamentation [25] and in various nonlinear optical systems, where dimensionality and nonlinear wave dynamics is more complex as compared to optical fibers: nonlinear optical cavities [159], nonlinear optical lattices[160], nonlinear waveguides [161] In contrast to optical fibers, where nonlinear dynamics takes place only in one (temporal) dimension, in the filamentation regime, the nonlinear wave interaction occurs in full three-dimensional space. Optical rogue waves in bulk media are therefore not linked to soliton dynamics and formation of particular soliton pulses with extreme characteristics; here, due to space-time coupling, they emerge from modulational instability-mediated pulse splitting and energy redistribution in space and time, taking a form of the X waves [158], which are weakly localized nondiffractive and nondispersive wave packets spontaneously occurring in media with normal group velocity dispersion [22, 128].

3.1 Extreme-value statistics in ultrafast white-light continuum generation

In this section we experimentally study the statistics of the white-light continuum generated by focusing of 130-fs, 800 nm pulses in a sapphire plate and show that the statistical distributions of the spectral intensity of the blue-shifted continuum components exhibit large shot-to-shot intensity variations that obey the extreme value statistics. This rogue-wave-like behaviour is detected only within a narrow input-pulse energy interval. By the use of numerical simulations, we show that the observed rogue-wave-like behaviour is associated with pulse splitting and build-up of intense trailing pulse. The extreme events are thereafter suppressed by the intensity clamping.

3.1.1 Experimental setup

The white-light continuum was generated by tightly focusing 130 fs, 800 nm central wavelength pulses from an amplified Ti:sapphire laser system (Spitfire PRO, Newport-Spectra Physics) into 3-mm thick synthetic sapphire crystal, a wide-bandgap material, which is widely used for WLC generation in the visible and near infrared [128] and possesses excellent characteristics for SC generation with near-infrared pumping: high cubic nonlinearity

($n_2 = 3.1 \times 10^{-20}\,\mathrm{m^2/W}$ [162]) and high optical damage threshold (up to 11 J/cm for 100 fs pulses [163]), and it shows no optical degradation effects under irradiation by intense ultrashort laser pulses at a kilohertz repetition rate. We used a typical scheme for WLC generation : a collimated laser beam with 1.6 mm FWHM diameter was focused by an $f = +50\,\mathrm{mm}$ lens onto the input face of 3-mm-thick sapphire plate. The input-pulse energy was varied in $0.1 \div 1\,\mu$J range by a halfwave plate and thin-film polarizer. A small fraction of the laser pulse energy was directed to a pyroelectric detector (Pulsar-2, Ophir Optronics) for energy monitoring. The WLC radiation was then re-collimated by an $f = +30\,\mathrm{mm}$ lens and after passing several neutrally scattering layers of thin teflon-film, was recorded by a fiber spectrometer with thermo-electrically cooled 16-bit detector (QE65000, Ocean Optics), which has a spectral detection range from 200 to 950 nm. The laser repetition rate was set to 10 Hz in order to synchronize the laser pulse with the energy meter and spectrometer that were synchronously operated in a single-shot regime.

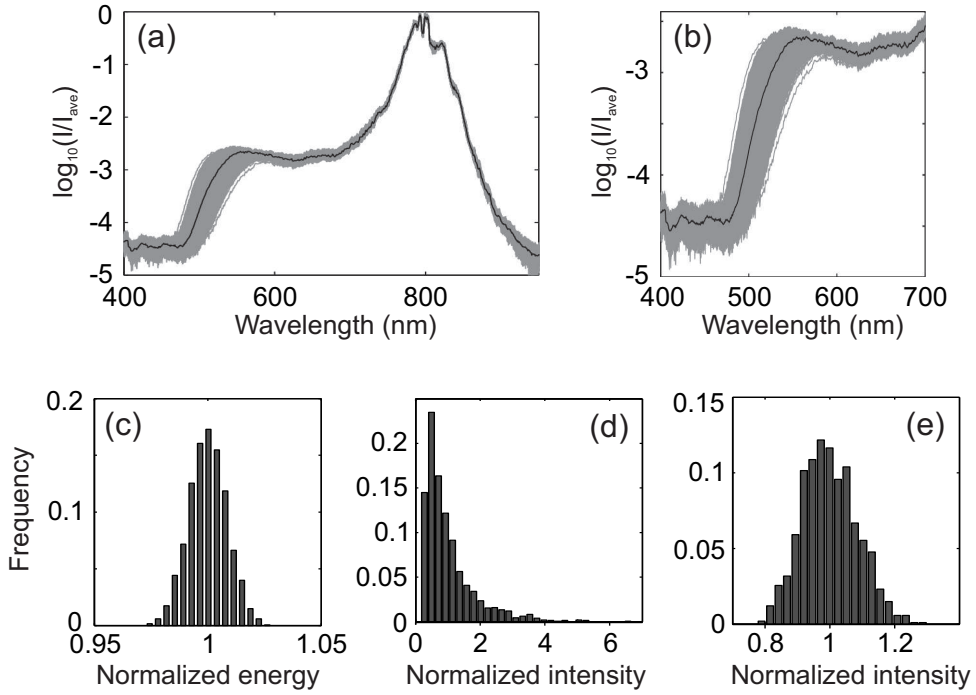

Figure 3.1.1: (a) 2000 individual WLC spectra (gray curves) generated at $E_{in} = 0.44\,\mu$J. The average spectrum is shown by the black curve. (b) Expanded view of the blue edge of WLC. Statistical distributions of (c) the input-pulse energy fluctuations, (d) and (e) the spectral intensity of the WLC at 500 nm and 650 nm, respectively.

3.1.2 Main results and discussion

Under described experimental settings, the spectral broadening was detected at the input-pulse energy $E_{in} = 0.3\,\mu$J, that corresponds to ~ 1.3 critical power of self-focusing, P_{cr}, which is 1.8 MW for sapphire. With increasing the input-pulse energy, an asymmetric, strongly blue-shifted spectral broadening was observed. Fig. 3.1.1(a) illustrates a series of consecutive 2000 WLC spectra, recorded at $E_{in} = 0.44\,\mu$J. In this condition, shot-to-shot variations of the spectral intensity in the plateau (550-700 nm) and in the cut-off (490-550 nm) regions revealed markedly different magnitudes of excursions from the average values, in particular, the spectral intensity of the blue edge varied considerably from shot to shot. These variations are highlighted by plotting the expanded blue-shifted portion of the individual WLC spectra in Fig. 3.1.1(b). In order to quantify the observed differences, in Figs. 3.1.1 (d) and (e) we plot the statistical distributions of the WLC spectral intensity at 500 nm and 650 nm, respectively. The spectral intensity distribution at 650 nm has a symmetric, nearly Gaussian shape, that yielded a standard deviation of $\sim 8\%$. In contrast, the spectral intensity at 500 nm exhibited a distinct long-tailed (L-shaped) statistical distribution, characteristic to an extreme-value process. Fig. 3.1.1(c) presents a corresponding histogram of the input-pulse energy fluctuations, which had perfectly Gaussian distribution. A standard deviation of 0.8% attested fairly stable laser operation.

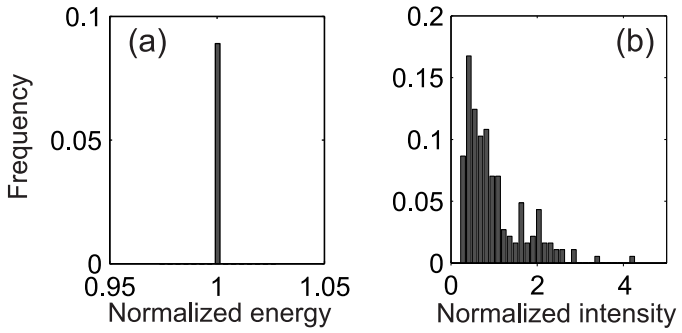

Figure 3.1.2: Statistical distributions of (a) the input-pulse energy, selected in $\pm 0.1\%$ energy range from the average value, (b) the resulting spectral intensity at 500 nm.

It is important to note that the L-shaped statistical distribution of the WLC spectral intensity at 500 nm is not a sole result of the laser pulse energy shot-to-shot fluctuations, but rather originates from shot-to-shot

input-pulse intensity modulation due to presence of the noise (intensity and phase noise), which is rather difficult to characterize experimentally. To verify this, in Fig. 3.1.2 we plot the statistical distribution of the spectral intensity at 500 nm, which corresponds only to a single input-energy bin (±0.1% from an average value) and despite fewer laser shots (approx. 200) included in the statistics, retains a similar L-shaped statistical distribution as in Fig. 3.1.1(d).

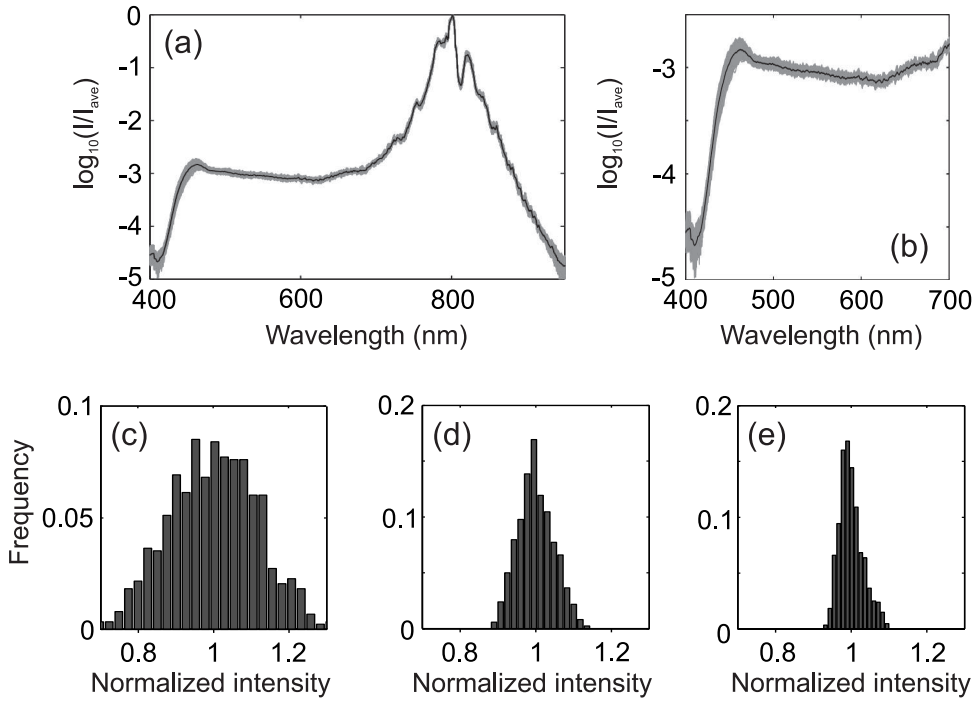

Figure 3.1.3: (a) and (b) the same as in Fig. 1, recorded at $E_{in} = 0.94\,\mu$J. Statistical distributions of the spectral intensity at (c) 425 nm, (d) 500 nm and (e) 650 nm.

Increasing the input-pulse energy above $0.6\,\mu$J, no further spectral broadening was observed, the blue edge of the WLC spectrum was limited to the cut-off wavelength of 410 nm, as a result of the combined effect of intensity clamping [7] and chromatic dispersion of the medium [74], which provides suitable intensity-dependent phase matching for the four-wave mixing process [25], and which serves as the main mechanism for spectral superbroadening. However, further increase of the input-pulse energy dramatically modified the statistics of the spectral intensity at all wavelengths. This is illustrated in Fig. 3.1.3 by plotting a series of 2000 WLC spectra and resulting statistics of the WLC spectral intensity at 425, 500 and 650 nm, as recorded at $E_{in} = 0.94\,\mu$J. Specifically, the statistical distri-

butions of the WLC spectral intensity acquire a nearly symmetric shapes across the entire wavelength range, see Figs. 3.1.3(c)-(e), thus indicating absence of the extreme events. Moreover, shot-to-shot fluctuations of the spectral intensity in the WLC plateau region were markedly suppressed, for example, the standard deviation of the spectral intensity at 650 nm was measured as low as approx. 3%. Note that throughout the measurements, the input-pulse energy fluctuations were essentially the same as illustrated in Fig. 3.1.1(c). The experimental results presented in Figs. 3.1.1- 3.1.3 were reproduced by the numerical simulations (not shown), using the numerical model by solving the extended nonlinear Schroedinger equation, which accounts for diffraction, dispersion, the instantaneous Kerr effect, self-steepening, 5-photon absorption, and the effect of free electron plasma with introduction of intensity and phase noise, as described in detail in Sec. 1.1 and [158].

From more detailed statistical investigations carried out by varying the input-pulse energy from 0.2 to 1 μJ, we found that distinct L-shaped statistical distributions were characteristic just to spectral components in the blue edge of the WLC spectrum. Moreover, the L-shaped statistics were observed only within a narrow input-energy interval between 0.40 and 0.46 μJ, when the blue edge of the WLC was confined in the wavelength interval of $480 \div 590$ nm. In order to quantitatively explain this finding, further we examined the spectral broadening dynamics versus the input-pulse energy. We measured the average (over 2000 laser shots) wavelength of the WLC blue edge, which was detected at a fixed intensity level of $10^{-3.5} I_{max}$, where I_{max} is the peak spectral intensity around 800 nm. The corresponding numerical simulations were performed without the inclusion of the noise, yielding fairly average values of the wavelength and peak intensity. The experimental and numerical data are compared in Fig. 3.1.4(a).

The experimentally measured non-Gaussian statistical distributions of the WLC spectral intensity at the blue edge were quantified by using a three-parameter Weibull fit function [140]:

$$f(x) = C \left(\frac{x - x_0}{l}\right)^{k-1} exp\left(-\left(\frac{x - x_0}{l}\right)^{k}\right) \tag{3.1.1}$$

where k, l and x_0 are shape, scale and location parameters, respectively, and

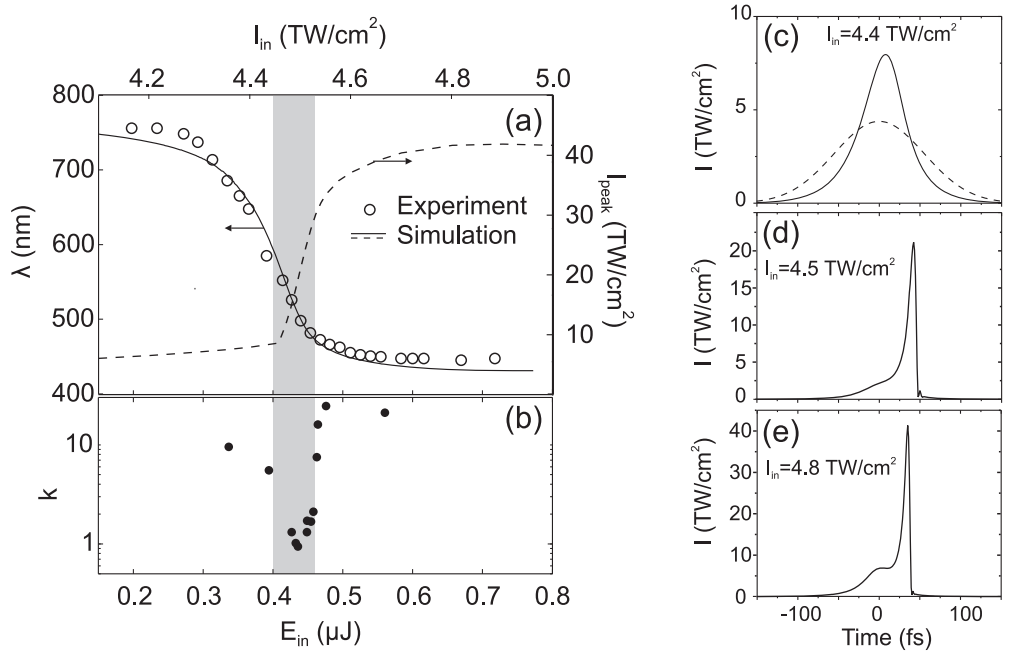

Figure 3.1.4: (a) Dynamics of the spectral broadening expressed as the wavelength of the blue edge. Dashed curve depicts the peak intensity inside the sapphire sample. (b) Shape parameter of the Weibull fit function vs input-pulse energy. Shaded area marks the energy (intensity) range where extreme-value statistics is detected. (c)-(e) Numerically simulated on-axis intensity profiles. Dashed curve shows the input-pulse. See text for details.

C is the normalization constant. The shape parameter k, which characterizes the skewness of the statistical distribution is plotted in Fig. 3.1.4(b). Note that for nearly-symmetric distributions that were recorded at the lowest ($E_{in} < 0.3\,\mu$J) and at the highest ($E_{in} > 0.6\,\mu$J) input-pulse energies, the fit function given by Eq. 3.1.1 yielded high k-values, but also a large error, therefore these data points were not included in the plot.

Summarizing the results illustrated in Fig. 3.1.4(a) and (b), we conclude that the dynamics of the spectral broadening undergoes three distinct stages, that are linked to the temporal dynamics of the pulse and resulting peak intensity inside the nonlinear medium, as shown by a dashed curve in Fig. 3.1.4(a), and where the blue-shifted spectral components of the WLC exhibit different statistical distributions. The initial WLC generation stage ($E_{in} = 0.28 \div 0.40\,\mu$J) is mainly associated with self-phase modulation-induced almost symmetric spectral broadening, where no extreme value statistics were detected. In the time domain, the pulse profile becomes gradually reshaped [Fig. 3.1.4(c)], however no pulse splitting occurs yet.

The second stage ($E_{in} = 0.40 \div 0.46\,\mu$J) is related to an abrupt increase of the peak intensity, which clearly indicates the pulse splitting event. The spectral broadening is governed by highly asymmetric pulse splitting, pulse front steepening and generation of the shock-front at the trailing edge of the pulse, as shown in Fig. 3.1.4(d), which is consistent with WLC generation scenario [12]. On the other hand, the spectral broadening might be described in terms of four-wave mixing and occurrence of two split X waves in full three-dimensional space [25], whose mutual interaction provides suitable phase matching condition for generation of the blue-shifted spectral components. In this stage, the build-up of the intense trailing pulse (which may be called transient stage of WLC generation) strongly depends on the input-pulse intensity. In fact, this suggests that any small intensity variation (intensity noise) in the input beam has a large impact on the resulting peak intensity of the trailing pulse, thus giving rise to the observed rogue-wave-like statistical distribution. In the final stage of the WLC generation ($E_{in} > 0.46\,\mu$J), the spectral broadening markedly slows down and finally stops at $E_{in} = 0.55\,\mu$J as the intensity of the trailing pulse is clamped at $\sim 41\,\mathrm{TW/cm^2}$ due to multiphoton (5-photon, in our case) absorption. The corresponding intensity profile is shown in Fig. 3.1.4(e). Here the dynamical picture settles and no extreme events occur. This in fact suggests that the intensity clamping acts as the mechanism, which suppresses occurrence of the extreme events. The extreme events therefore occur only within a narrow input-pulse energy (intensity) range, which is defined by the pulse splitting and intensity clamping.

3.1.3 Conclusion

In conclusion, it was demonstrated that the rogue-wave-like statistics of the spectral intensity of the WLC generated in a wide-bandgap solid (sapphire) are observed only in the transient stage of the WLC generation, and are associated with pulse splitting and build-up of intense trailing pulse, that strongly depend on the input-pulse intensity. The intensity clamping was found to be a mechanism which suppresses the occurrence of the extreme events. These findings also explain why the extreme events in WLC generation in bulk medium are observed only in a narrow input-energy (intensity) interval.

3.2 Spatio-temporal rogue events: rogue X-waves

In this Section we report on a class of optical rogue events that occur in three-dimensional geometries as opposed to the widely studied one- or two-dimensional systems. In three-dimensional space, strong space-time coupling may lead to rogue events that bear some specific features, namely a trailing peak with a lower-than-average intensity albeit with a wider spectrum. We show that these extreme events are associated to X-wave formation in the normal group-velocity-dispersion regime, as opposed to the temporal solitons observed in the anomalous regime in optical fibers.

3.2.1 Experimental setup

In the experiment we used an amplified Ti:sapphire laser system (Spitfire-PRO, Newport-Spectra Physics) that delivers 130-fs pulses at $\lambda_0 = 800$ nm. The laser beam was attenuated and loosely focused by $f = 500$ mm lens down to 60 μm FWHM diameter at the input face of the 43-mm-long water-filled cuvette. The input energy of 0.61 μJ (that equates to $1.23P_{\mathrm{cr}}$, $P_{\mathrm{cr}} = 3.77\lambda_0^2/(8\pi n_0 n_2) = 3.8\,\mathrm{MW}$, where $n_0 = 1.328$ and $n_2 = 1.9 \times 10^{-16}$ cm^2/W [83] are linear and nonlinear refractive indexes of water at 800 nm) was chosen so as to excite a single filament, whose occurrence was verified by the white-light spectrum at the exit of the nonlinear medium, and to uncover early spatiotemporal dynamics, not altered by propagation and other nonlinear effects. The spectrum of the filament was collected using a short focal distance ($f = 30\,\mathrm{mm}$) lens, and after passing several neutrally scattering layers of thin teflon-film was directed to a fiber spectrometer with a 16-bit detector (Ocean Optics), which has spectral detection range from 200 nm to 950 nm. The statistical distribution of the input-pulse energy was almost perfectly Gaussian, with the standard deviation of $\leq 1\%$.

3.2.2 Main results

The occurrence of extreme events in the filamentation regime is readily observable in the extreme-value statistics of the spectral intensity, which exhibits characteristic L-shaped distribution. Fig. 3.2.1(a) illustrates the statistics of experimentally recorded 5000 single-shot spectra measured at $1.23P_{cr}$. Multiple gray curves show the individual single-shot spectra, whose

average spectral intensity profile is overplotted by a black curve. The widest and the narrowest spectra are highlighted by the red and blue curves, respectively, while the dashed curve indicates the input-pulse spectrum.

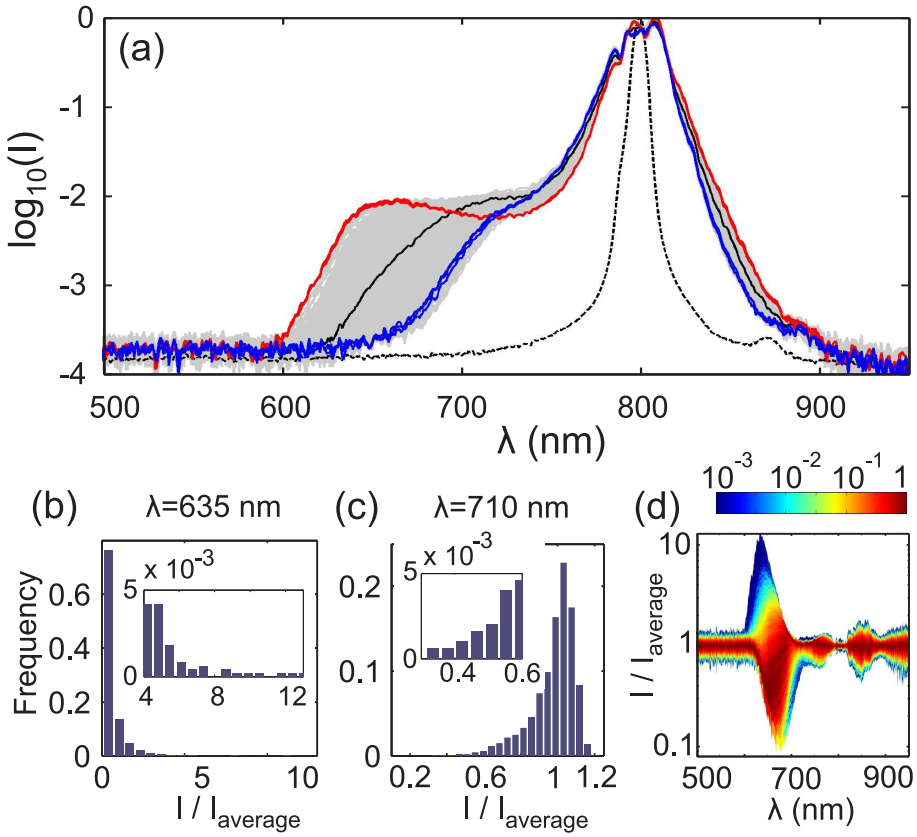

Figure 3.2.1: (a) Experimentally measured 5000 single-shot spectra of the filament (gray curves) recorded at $1.23P_{cr}$. The average spectrum is shown by the black curve, the widest and the narrowest extremes are highlighted by the red and blue curves, respectively, while the input spectrum is plotted by the dashed curve. Frequency distributions of the spectral intensity at: (b) 635 nm, (c) 710 nm. Insets show a magnified portion of the long tails. (d) statistics of the spectral intensity across the entire spectral detection range.

A more detailed statistical analysis of these spectra is presented in Fig. 3.2.1 (b) and (c) by plotting the frequency distribution of the spectral intensity at particular wavelengths of 635 nm and 710 nm, respectively. At 635 nm, the spectral intensity exhibits a clear right-tailed distribution. The spectral intensity of the most prominent extreme events is more than 10 times larger than the average, as seen from the inset, which highlights the extended tail. Interestingly, at 710 nm, the L-shaped distribution is left-tailed, i.e. showing that in the same dataset there is a number of events exposing small-intensity extremes. A closer look at Fig. 3.2.1(a) reveals that these marginal spectra have different shapes: those with the highest spectral intensity at 650 nm ex-

hibit a dip around 710 nm, and vice versa. Hence, the observed statistics at different wavelengths is determined by the change of the spectral shape due to correlation between frequency components that occur in the self-phase modulation-induced spectral broadening [164]. Fig. 3.2.1(d) combines the statistics of the spectral intensity across the entire spectral detection range, where (logarithmic) color coding renders the normalized frequency of the spectral intensity at a particular wavelength. Notice that distinct extreme events occur mostly on the blue-shifted side of the spectrum.

3.2.3 Numerical simulations

We quantitatively reproduced the experimental results and characterized the spatiotemporal structure of the extreme events by the use of numerical simulations. We solved the extended nonlinear Schroedinger equation (see Sec. 1.1 for details) with multiphoton absorption order $K = 5$, assuming $E_g = 6.5$ eV and a single photon energy $\hbar\omega_0 = 1.5$ eV, the multiphoton absorption coefficient, taken as $\beta^{(5)} = 1.1 \times 10^{-51}$ cm^7/W^4, cross section for electron-neutral inverse bremsstrahlung $\sigma = 4.7 \times 10^{-22}$ m^2 and electronic collision time in the conduction band$\tau_c = 3$ fs [165]. The values of $\beta^{(5)}$ and σ were evaluated using the formalism described in [63], the plasma dynamics was accounted for in the same manner as in Sec. 1.1, including multiphoton and avalanche ionization and neglecting electron diffusion and recombination owing to sufficiently longer lifetime of the electron plasma as compared to the pulse width [45]. Full dispersion for distilled water was accounted for according to [166]. The calculations were performed for input Gaussian pulsed beam with 60 μm diameter, $t_p = 130$ fs FWHM pulsewidth, central wavelength $\lambda_0 = 800$ nm and the input-beam intensity of $I_0 = 130$ GW/cm^2. In order to simulate the output statistics, we have modified the input-beam by introducing 2% intensity noise, 0.1% phase noise and 1% energy noise. The noise has Gaussian distribution and was implemented using Box-Muller transform of uniformly distributed random numbers.

3.2.4 Discussion

The statistical results obtained by the numerical simulations are shown in Fig. 3.2.2. Fig. 3.2.2(a) illustrates 500 individual axial spectra, panels (b) and (c) show the statistical distributions of the spectral intensity at 635

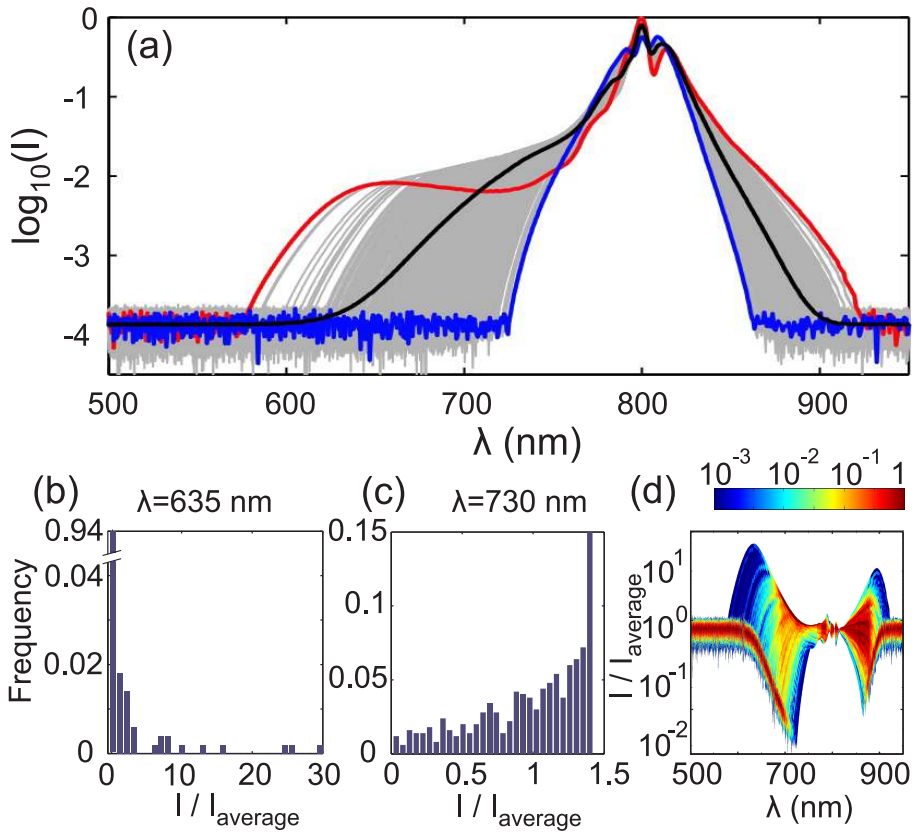

Figure 3.2.2: (a) Numerically simulated 500 single-shot spectra (gray curves). Curve designations are the same as in Fig. 3.2.1(a). Frequency distributions of the spectral intensity at: (b) 635 nm, (c) 730 nm. (d) statistics of the spectral intensity across the entire wavelength range.

and 730 nm, respectively, and which are summarized for the entire spectral range in panel (d). Note here, that in the presentation of the numerical results, we have added an artificial noise at the level, which corresponds to experimental detection range of the fiber spectrometer. The numerical data fairly recovers all the essential statistical features captured experimentally, as shown in Fig. 3.2.1.

The relevant question is how the extreme events in the spectral intensity manifest themselves in the space-time domain? We recall that in the fiber environment, rogue waves are associated with the red-shifted soliton pulses of extreme amplitude, which emerge in the region of anomalous group-velocity dispersion. However, the temporal dynamics in femtosecond filamentation is different: the spectral broadening during self-focusing of the ultrashort light pulses in a medium with normal group-velocity dispersion is linked to pulse splitting and shock-front dynamics, where the leading shock-front is associated with the red-shifted axial radiation, and the trail-

ing shock-front with the blue-shifted axial radiation [12]. A more general view of this concept was proposed in the framework of two split nonlinear X-waves, one traveling at subluminal and another at superluminal velocities with respect to the group velocity of the input Gaussian pulse, and whose localization is ensured by the off-axis, conical part of the beam (conical emission) [24, 25, 86].

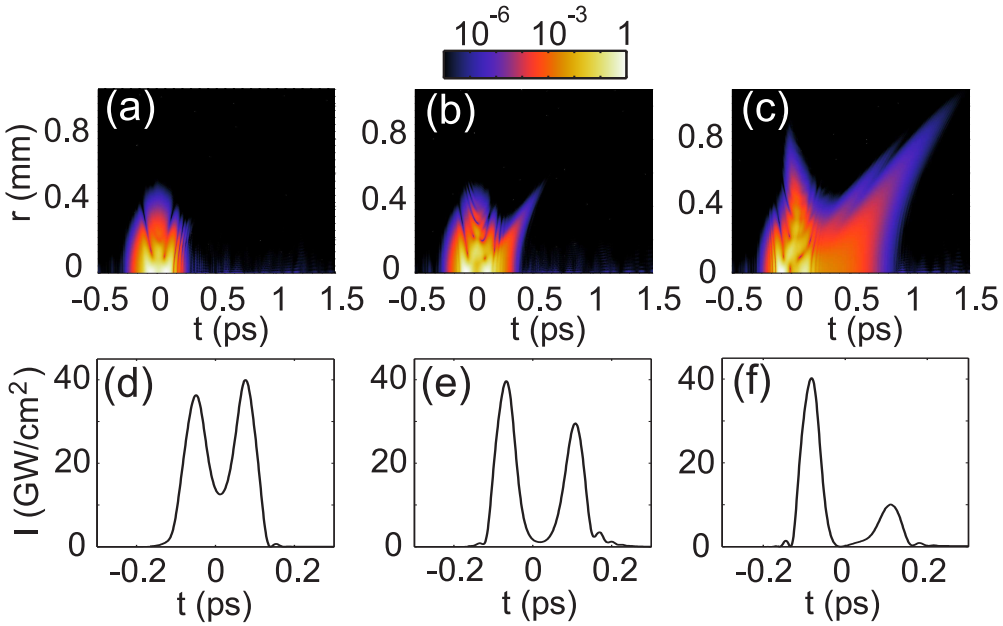

Figure 3.2.3: (a)-(c) spatiotemporal and (d)-(f) on-axis intensity profiles corresponding to the spectra highlighted in Fig. 3.2.2(a). See text for details.

Figures 3.2.3(a)-(c) show the numerically simulated spatiotemporal intensity distributions, that correspond to the narrowest, the average and the widest spectra, respectively, as highlighted in Fig. 3.2.2(a), indicating formation of the split X-waves. Panels (d)-(f) show the corresponding on-axis temporal intensity profiles, which highlight pulse splitting events and formation of optical shocks, that are recognized by weak and rapidly decaying oscillations at the pulse fronts. Notably, major differences between the three different cases are observed only in the trailing X-wave, whose spatiotemporal extent and on-axis intensity exhibit great variability if compared with the leading peak.

This finding was verified also experimentally, by measuring the cross-correlation function of the on-axis part of the filament as transmitted through a 40-μm pinhole, imaged and sampled with short, 30-fs pulse in 20-μm-thick beta-barium borate crystal via sum-frequency generation [Fig. 3.2.4 (a)]. Figures 3.2.4 (b) and (c) compare the numerical and experimental inten-

sity distributions, measured at the time delay of −60 and +70 fs [marked by dashed lines in Fig. 3.2.4 (a)], corresponding to the leading and trailing peaks. The results presented in Fig. 3.2.4 (b) and (c) imply that variation range of the leading pulse intensity is quite compact, its statistical distribution aside from a very slight skewness, is similar to the input-intensity variation. In contrast, the intensity of the trailing pulse varies considerably, with clearly expressed left-tailed extreme-value statistics. Given the good agreement between the numerical and experimental data, it is quite surprising that the statistics of the leading and trailing pulses are markedly different, so only the trailing pulse (or more generally, the overall trailing wave-packet) exhibits a rogue-wave-like behavior. We interpret this difference as the result of the X-wave formation under the experimental condition addressed: higher order dispersion and phase-matching in water, and more specifically, water absorption, that increases rapidly towards the infrared [39]. However, the observed peculiarities in dynamics of the red- and blue-shifted components require further, extensive study.

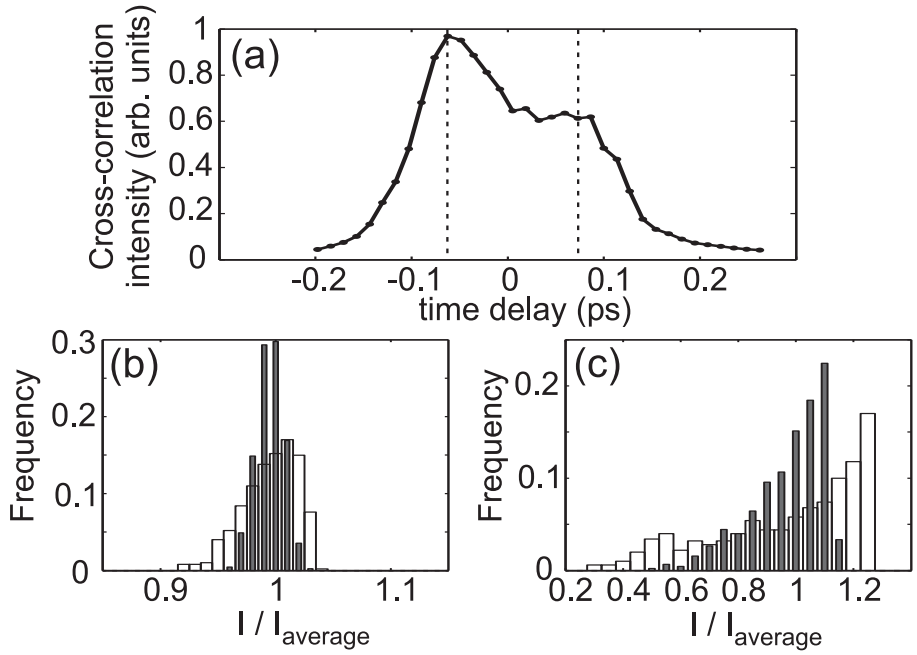

Figure 3.2.4: (a) Experimentally measured cross-correlation function of the on-axis radiation. (b) and (c) show the numerically simulated (white bars) and experimentally measured (black bars) intensity distributions of the leading and trailing peaks, respectively.

3.2.5 Conclusions

In conclusion, under investigated experimental conditions, the extreme events in the femtosecond filamentation regime are identified as large *space-time coupled* intensity fluctuations and formation of an X-wave at the trailing edge of the input pulse. The results are significantly different with respect to one-dimensional fiber settings in which extreme events are associated to higher-than-average intensities. The three-dimensional extreme event needs to be visualized in full three-dimensional rather than in a reduced one-dimensional space: indeed, in Fig. 3.2.3(c) we immediately notice that the extreme event is associated to the clear formation of an X-wave with largely extended conical tail, i.e. of a truly space-time coupled, three-dimensional wave-packet. Due to the ubiquity of space-time coupled effects in three-dimensional systems we may expect to observe similar rogue X-wave formation and wave localization events also in other settings involving e.g, acoustic [167] and even seismic waves [168].

3.3 Statistical properties of ultrafast supercontinuum

In recent years, Bessel beams carrying femtosecond pulses [femtosecond Bessel beams (FBBs)] have attracted a great deal of interest and constitute a rapidly growing research topic in the field of ultrafast light–matter interactions. The unique nondiffractive property of Bessel beams ensures high energy localization within the intense central spot over long distances, which makes Bessel beams very attractive for use in diverse fields of modern optics [169] and ultrafast technology [170]. Due to their conical nature FBBs are generally considered resistant to self-action effects, since self-focusing and self-phase modulation start manifesting themselves at an input power largely exceeding the critical power for selffocusing of a conventional Gaussian beam. In that regard, filamentation of FBBs poses a number of differences as compared to a standard case of Gaussian beam filamentation [66, 171–173]. The most relevant differences are related to slight progressive reshaping of its original near-field intensity profile (ring compression and loss of contrast), generation of extra rings, and occurrence of axial radiation in the far field [174–176]. These differences result in a

different scenario of the spectral broadening and SC generation with FBBs, which so far has been studied in water [175] and in barium fluoride [177].

On the other hand, there is great flexibility in producing a Bessel beam with desired properties: cone angle, central spot size, energy content, particular intensity variation along the propagation axis, and length of the Bessel zone, suggesting numerous, yet unexplored, possibilities for SC generation with FBBs. Moreover, to date, the statistical properties of the SC generated with Gaussian beams and FBBs, which are of great importance for many practical applications, have as yet been poorly investigated. Therefore, this Section aims at a comparative study of ultrafast SC generation in sapphire crystal using femtosecond Gaussian and Bessel beams. We show that, at the particular interaction geometry used in our experiment, the SC generated with an FBB has a smooth and featureless spectrum, whose extent and stability compares to that generated with low-numeric-aperture (NA) focused Gaussian beam. Our findings also indicate that the fluctuations of the SC spectral intensity are related to spectral correlations across the entire wavelength range covered by SC radiation.

3.3.1 Experimental setup

The experiments were carried out using a 1 kHz repetition rate Ti:sapphire laser system (Spitfire-PRO, Newport-Spectra Physics), which delivered 130 fs pulses with a central wavelength of 800 nm. Two focusing geometries used in the experiment are schematically sketched in Fig. 1. In the first case, shown in Fig. 1(a), a collimated Gaussian beam with $d = 650\,\mu$m FWHM diameter was suitably attenuated and focused by an $f = 50\,$mmlens onto 3-mm thick synthetic sapphire crystal so as to access a standard, low-NA condition for SC generation [130]. The estimated FWHM diameter of the focal spot was $30\,\mu$m, which corresponded to NA ≈ 0.01. The input energy was varied in the $0.2 \div 2.0\,\mu$J range, which allowed us to capture dynamics of the spectral broadening in detail. The output SC radiation was collimated and focused by two$f = 30\,$mm lenses arranged in $4f$ imaging geometry ensuring that almost all SC radiation was coupled onto the $200\,\mu$m diameter fiber tip of the fiber spectrometer (QE65000, Ocean Optics) with a 16-bit dynamic range thermoelectrically cooled converter and a $200 \div 950\,$nm detection range. The spectrometer was calibrated, and the recorded spectral intensity of the SC radiation was corrected for the sensitivity using the

actual curve of the spectral response. The acquisition rate of the spectrometer was synchronized with the repetition rate of the laser, thus enabling us to capture the SC spectra in a single-shot regime. At each given input pulse energy, a series of 2000 consecutive SC spectra was measured in order to accumulate the necessary statistics of the spectral intensity throughout the entire detection range. In the second case, shown in Fig. 3.3.1(a), the Gaussian beam was focused by BK7 glass axicon with base angle $\gamma = 2°18'$ so as to produce an FBB with a length of the Bessel zone of 26 mm and FWHM diameter of the central spot of 27 μm, which nearly matched the FWHM diameter of the focal spot of the Gaussian beam used in the first experiment. As a nonlinear medium, we used the same 3 mm-long sapphire sample, which was placed at the point where the Bessel beam had the highest intensity, i.e., at $d = 14$ mm from the axicon tip, as schematically illustrated in Fig. 3.3.1(b). In this case, the SC radiation emerged on the Bessel beam axis, which was then easily separated from the pump cone in the far field and collected in the same manner as described above. In the case of FBB, the SC generation was observed at more than 10 times higher input energy, which in the present case was varied in the range of $1 \div 16\,\mu$J.

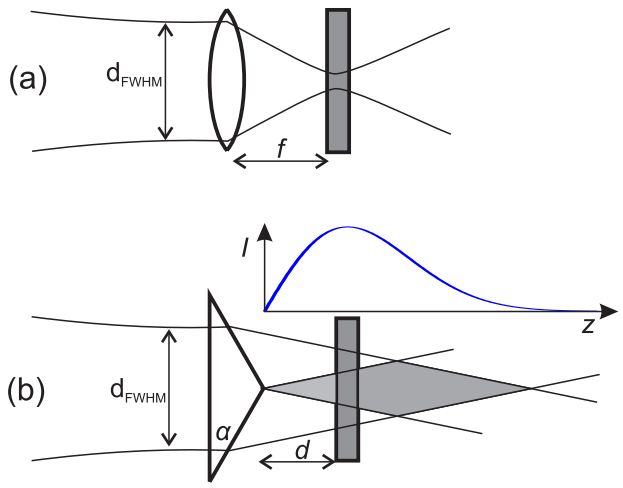

Figure 3.3.1: Experimental configurations showing the focusing conditions for (a) a Gaussian beam and (b) an FBB, where the inset shows the calculated intensity of the central peak versus distance z from the axicon tip. The real dimensions are not to scale.

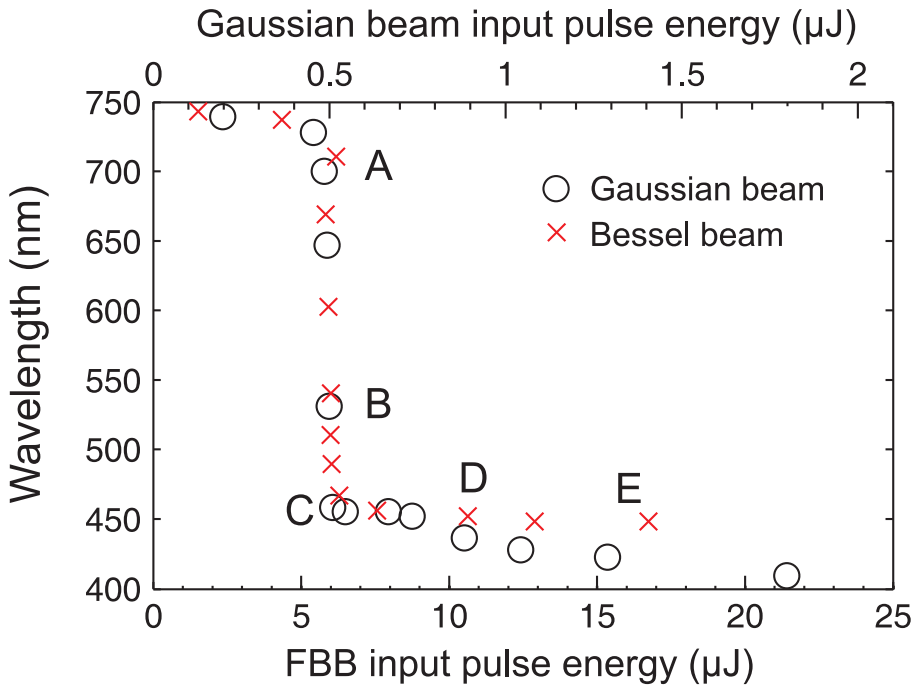

Figure 3.3.2: Cutoff wavelength of the SC generated by Gaussian beam and FBB versus the input pulse energy.

3.3.2 Comparative study of supercontinuum generated by femtosecond Bessel and Gaussian beams

Figure 3.3.2 compares the measured cutoff wavelength (defined at 10^{-4} intensity level at the blue side of the spectrum) of the SC spectra as a function of the input energy for Gaussian and Bessel input beams. Despite the marked difference in the absolute input energy values, the spectral broadening in both cases appears to be very similar: as the input pulse energy exceeds some threshold value (0.4 μJ for a Gaussian beam and 5.5 μJ for an FBB), there is observed very rapid, almost explosive blue broadening, which takes place within a very narrow input energy interval. Thereafter, with further increase of the input pulse energy, the blue broadening markedly slows down, and the cutoff wavelength slowly proceeds to 400 nm in the case of the Gaussian input beam and to 450 nm in the case of the FBB. More than tenfold difference in the input pulse energy could be explained in part by the differences of energy distribution in the Gaussian beam and FBB intensity profiles and in part by the differences of their nonlinear propagation. A computation of the peak intensity at the focal spot of the Gaussian beam and at the central spot of the FBB at 14 mm from the axicon tip yields

already a sevenfold difference in the peak intensity for the same input pulse energy, whereas the specific issues of nonlinear propagation of the FBB are addressed in [171, 172, 174, 177] and later in this text.

In order to analyze the spectral dynamics of the SC generation in more detail, in Fig. 3.3.2 we highlight five relevant stages of the spectral broadening, which are labeled by letters A, B, C, D, and E. The averaged (over 2000 laser shots) SC spectra representing these cases are shown in Fig. 3.3.3.

The dynamics of spectral broadening and development of the spectral shapes generated by low-NA focused Gaussian beam are shown in Fig. 3.3.3(a) and could be interpreted in the framework of the standard SC generation scenario [12]. In the initial stage (A), the spectrum of the input pulse broadens almost symmetrically due to pulse shortening and selfphase modulation. In the intermediate stage (B) the input pulse undergoes strong temporal reshaping, pulse front steepening, and eventually splits into two subpulses. Out of these, the most intense is the trailing subpulse, which gives rise to strong blueshifted spectral broadening. Thereafter, its peak intensity becomes rapidly clamped due to multiphoton absorption [16], and the spectral broadening saturates (C), yielding a typical strongly asymmetric SC spectrum [7], which has a characteristic blue bump near the cutoff that appears due to an X-wave phase-matching condition [178]. In the saturation regime (D), the spectral intensity becomes more smooth along with a slight increase of the red part in the SC spectrum. Finally, the pulse-splitting scenario is further confirmed by the SC spectrum recorded in the postsaturation regime (E). Here the SC spectrum develops fine periodic modulation, which occurs on both sides of the central wavelength, which is a signature of the secondary pulse-splitting event.

An apparent similarity of the spectral broadening recorded with FBB, as shown in Fig. 3.3.3(b), suggests that the axial pulse undergoes almost identical temporal dynamics. However, it must be noted that the measured smooth SC spectra are in sharp contrast with those reported in the previous studies [175, 177], which demonstrate distinct modulation of the spectral intensity and weaker spectral broadening. These marked differences could be attributed to the differences in the Bessel beam geometry used. In aforementioned experiments, the SC was generated in long samples exploiting extended depth of focus of the FBBs, which, however, had a considerable intensity variation of the central spot along the nonlinear medium, as il-

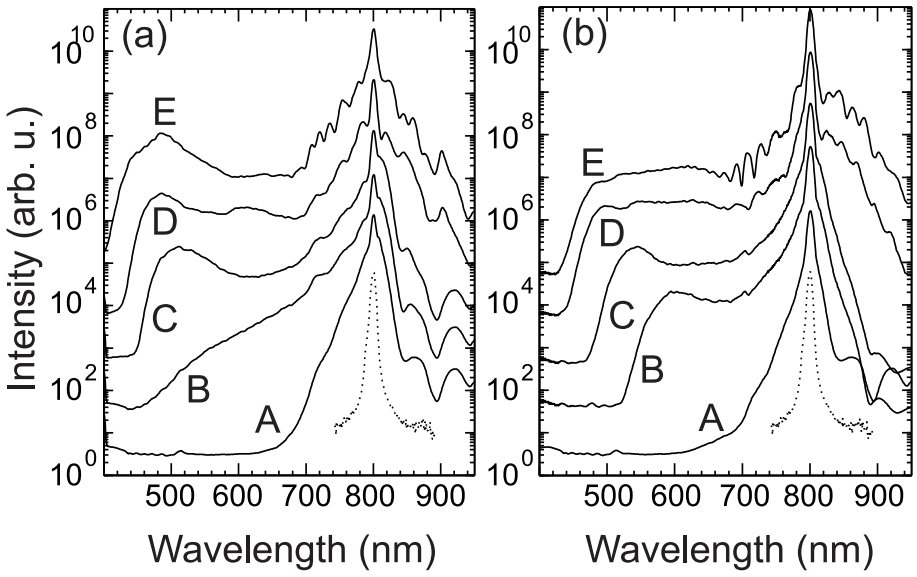

Figure 3.3.3: SC spectra generated by (a) a Gaussian input beam and (b) an FBB. Labeled spectra correspond to the cases highlighted in Fig. 3.3.2. The input spectrum is shown by a dashed curve. All the spectra are normalized to the peak intensity at the carrier wavelength (800 nm).

lustrated in the inset of Fig. 3.3.1(b). This in turn imposed a varying, intensity-dependent transverse phase-matching condition [179] for generation of the axial component via noncollinear four-wave mixing [175]. Much higher input pulse energy used in [177] led to multiple refocusing, which had a similar effect on the SC spectral modulation. Conversely, in the current case, the intensity change of the central spot throughout the short length (3 mm) of the nonlinear medium is negligible, so the phase-matching condition under which the axial pulse is generated was kept fairly constant. Once the intense axial pulse is produced, it starts its own nonlinear propagation, as justified by the dynamics of the spectral broadening, as shown in Fig. 3.3.3(b). There are, however, some differences in the SC spectra as generated by the Gaussian beam and the FBB. In the latter case, apart from somewhat weaker spectral broadening, the FBB-induced SC spectrum exhibits a very intense peak at the carrier wavelength (at least by 1 order of magnitude larger than in the case of the SC generated by a Gaussian beam), which is due to continuous refilling of the central spot by conical components of the Bessel beam [180].

In what follows, we analyze the statistics of the SC spectral intensity throughout the entire spectrum. The statistical issues are of primary importance for most applications of the ultrafast SC, which usually require high shot-

to-shot reproducibility of the SC spectra. However, to the best of our knowledge, only a very few works have been devoted to investigations of the statistical properties of the SC generated by Gaussian beams [128, 133, 181], whereas no such study has been performed addressing the statistics of the SC excited by FBBs.

The statistical results are summarized in Fig. 3.3.4, where curves depicting the fluctuations of the spectral intensity are labeled according to the spectra shown in Fig. 3.3.3. Here we restrict ourselves just to cases A–D, since case E represents a much more complex temporal structure of the SC pulse and is, therefore, of limited practical interest. The fluctuations of the spectral intensity are expressed through the root-mean-square (RMS) error at a given wavelength across the whole SC spectrum, being computed from a series of consecutive 2000 single-shot SC spectra recorded at a given input energy. Specifically, the RMS error was computed by subtracting the dark-current-induced noise, which was always lower than actual signal counts throughout the entire SC spectrum. The RMS error of the input pulse energy during the measurement was 0.4%, thus attesting, indeed, to stable laser operation.

First we refer to the statistics of the SC generated by the Gaussian beam, which are shown in Fig. 3.3.4(a). As expected, the fluctuations of the spectral intensity have a strong dependence on the input pulse energy; however, the character of the RMS fluctuations and its successive dynamics reveals an interesting picture. At the initial stage of the spectral broadening (curve A), the blue edge of the SC spectrum is very unstable with large shot-to-shot fluctuations whose RMS error is close to 30%. At the same time, spectral intensity at the closest vicinity of the central wavelength (800 nm) is fairly stable. With slight increase of the input pulse energy, which results in further spectral broadening, the unstable part of the spectrum shifts toward shorter wavelengths, where the instability approaches 100% (curve B). The elevated instability at the blue edge of the spectrum is attributed to the occurrence of extreme (rogue) events that are characterized by non-Gaussian, highly skewed (so called L-shaped) statistical distribution of the spectral intensity; see [133] for more details. With further increase of the input pulse energy, approaching the saturation regime of the spectral broadening (curve C), the instability at the blue edge becomes suppressed along with emergence of a remarkable feature: very stable intervals seen as a

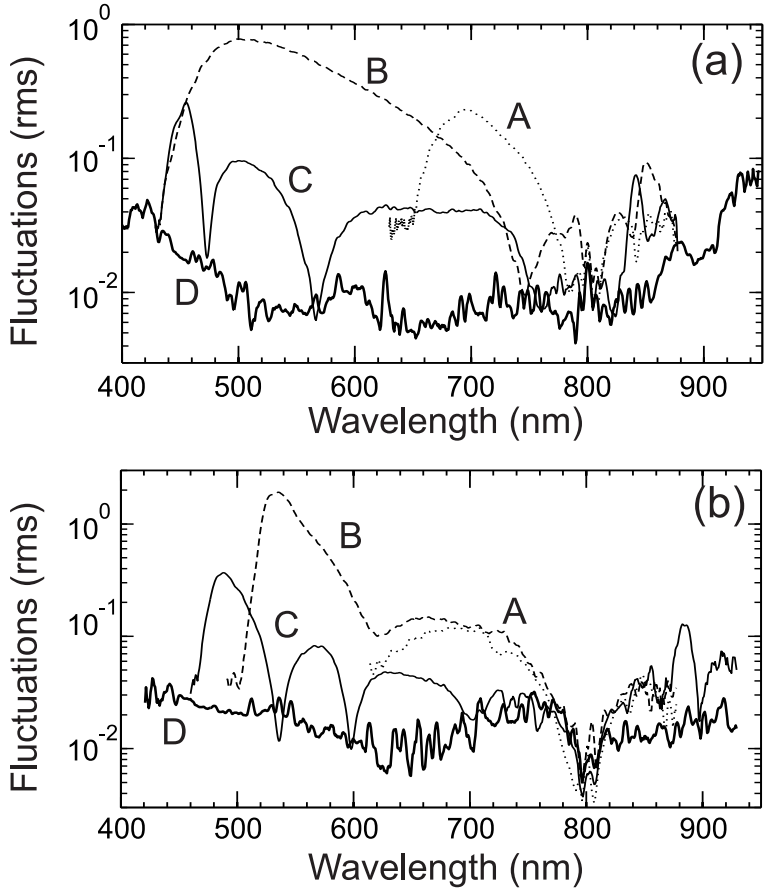

Figure 3.3.4: RMS error of the SC spectral intensity fluctuations at different stages of the spectral broadening: (a) in the case of the Gaussian input beam and (b) in the case of FBB. The curves are labeled according to Fig. 3.3.3.

broad minimum around the pump wavelength ($750 \div 820$ nm) and sharp prominent minima at wavelengths of 470 and 570 nm. Note that a similar feature located at 750 nm already emerges in curve B. Finally, in the regime of saturation of the spectral broadening (curve D), the spectral intensity becomes remarkably stable with RMS error $\leq 1\%$ across most of the wavelength range and few percent at the very edges, with small and irregular RMS oscillations. Very similar results, with almost identical features of the RMS fluctuations, were recorded also in the case of FBB input, as shown in Fig. 3.3.4(b). The only difference in the latter case is apparently suppressed fluctuations of the spectral intensity around 800 nm, as due to refilling effect [180].

In order to get some more insight into the observed statistical features and occurrence of distinct stability zones in particular, we investigated the correlations of the spectral intensity fluctuations within the entire SC spectrum.

For that purpose, we computed the cross-correlation coefficient between the spectral intensities S at wavelengths λ_1 and λ_2 [164, 182]:

$$C(\lambda_1, \lambda_2) = \frac{V(S_1 + S_2) - V(S_1) - V(S_2)}{2\sqrt{V(S_1)V(S_2)}} \tag{3.3.1}$$

where V is the variance of the spectral intensity. By varying the two wavelengths, the complete cross-correlation maps of the spectral intensity fluctuations were computed, as illustrated in Fig. 3.3.5. These complex patterns emerge from the basic mechanisms of the spectral broadening, i.e., self-phase modulation and successive four-wave mixing processes [164], and increase in complexity with increasing input energy.

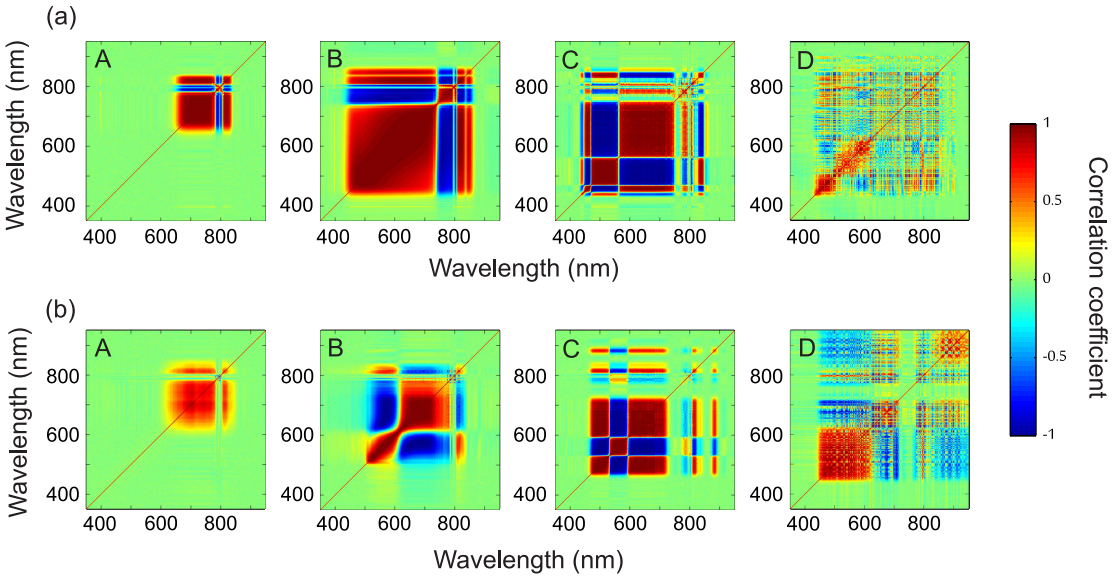

Figure 3.3.5: Cross-correlation maps of the spectral intensity fluctuations within SC spectra generated by (a) a Gaussian beam and (b) an FBB. Labels in capital letters correspond to SC spectra and their intensity fluctuation curves shown in Figs. 3.3.2 and 3.3.3.

In the case of the Gaussian input beam [Fig. 3.3.5(a)], the cross-correlation map reveals the occurrence of clear correlating ($C = 1$) and anticorrelating ($C = -1$) zones (case A), where the anticorrelation cross centered on the carrier wavelength manifests the depletion of the pump, while the occurrence of correlated regions on both sides of the input wavelength signifies the generation of conjugated wavelengths via four-wave mixing. In contrast, in the case of FBB [Fig. 3.3.5(b)], no correlation ($C = 0$) around the pump wavelength is observed, possibly owing to the conical nature of the

Bessel beam, which tends to continuously refill the central peak at the carrier wavelength [180], thus masking its correlation with generated spectral components. At slightly higher input energy (case B), alternating correlation and anticorrelation zones extend further due to four-wave mixing, while the character of the correlation pattern remains basically the same. Here, however, a fine structure of the anticorrelation cross around the carrier wavelength becomes clearly visible. Note that, at this instance, the pulse is expected to be already split, and the split subpulses with slightly shifted carrier frequencies serve as new pumps for the four-wave-mixing process [25]. Interestingly, even at this stage of the spectral broadening, careful inspection of the correlation maps referring to both focusing cases reveals that narrow noncorrelated dips in between the correlating and anticorrelating zones exactly coincide with markedly reduced fluctuations of the SC spectral intensity, as could be easily verified by comparing Figs. 3.3.5 and 3.3.4. At higher input energy, where the spectral broadening is close to saturation (case C), the correlation pattern develops a more complex structure, which consists of alternating correlation and anticorrelation zones, separated by narrow noncorrelating regions in the visible range and more extended ones around the carrier wavelength. The observed complexity in the correlation patterns could possibly be attributed to cascaded four-wave mixing between the spectral components of the SC, which, according to the energy conservation $\omega_{\text{pump}} + \omega_{\text{pump}} = \omega_{\text{signal}} + \omega_{\text{idler}}$, might take place in a variety of pathways. For example, an anticorrelating zone in $470 \div 560\,\text{nm}$ range could be interpreted as a new pump, which produces mutually correlated signal and idler waves with wavelengths in the range of $450 \div 460$ and $580 \div 750\,\text{nm}$, respectively, etc. Note how the noncorrelating regions perfectly coincide with suppressed fluctuations of the spectral intensity, as seen from curves C in Figs. 3.3.4(a) and 3.3.4(b). Finally, in the saturation regime of the spectral broadening (case D), the cross-correlation patterns become deteriorated and highly structured, being generally dominated by small-scale weakly or noncorrelating regions. That loss of correlation coincides with marked suppression of the intensity fluctuations across the entire SC spectrum, as seen from curves D in Figs. 3.3.4(a) and 3.3.4(b).

Firstly it must be pointed out that different spectrum realizations come from small noise in the pump beam. The response of our physical system could be considered non-chaotic – if exactly the same initial conditions

would be provided we'd have the same output. Fluctuations in the output spectra could be easily modeled by the pump beam intensity fluctuation although there might be other noise sources in the system (air turbulence, medium density fluctuations etc.). Furthermore we can state that a little change in the initial conditions is approximately equal to a little change in the propagation distance and this holds on while the changes are small and no additional effects appear due to changed propagation. Therefore spectra and their corresponding correlation maps show how the spectra would change with a minute increase (decrease) in the propagation distance. Since the intensity some spectral components are rising and some are falling we could guess that there is energy transfer between them through FWM process.

Spectral intensity correlations were already analyzed in [164, 182, 183] however apart for attributing appearance of correlating and anti-correlating zones to four wave mixing, more detailed insight was not provided. Four wave mixing appears as conversion of two pump photons to signal and idler. Therefore we should look for correlations between $-(I(\lambda_{\text{pump1}}) + I(\lambda_{\text{pump2}})$ and $-(I(\lambda_{\text{signal}}) + I(\lambda_{\text{idler}})$. Taking into account energy conservation law $\omega_{\text{pump1}} + \omega_{\text{pump2}} = \omega_{\text{signal}} + \omega_{\text{idler}}$, we have 3 degrees of freedom (e.g. λ_{pump1}, λ_{pump2} andλ_{signal}). Our spectrometer range prevents us from identifying processed where idler wavelength lies in NIR region, however we were still able to analyze and attribute supercontinuum generation to FWM from the available spectra. One of the major findings is that there are no FWM if the pump wavelengths do not belong to the same correlating (anti-correlating) island on the map. Therefore 3-dimensional correlations maps can be visualized in 2 dimensions by introducing additional constrain $\lambda_{\text{pump1}} = \lambda_{\text{pump2}}$.

In the initial stage of spectral broadening (Fig. 3.3.6(a) – A case for Gaussian pump), there are two pump pulses centered at 790 nm and 800 nm which generate signal ($650 \div 790$ nm) and idler ($800 \div 950$ nm). The signal should extend up to 450 nm which correspond to over 3 μm idler which is out of detection wavelength of the spectrometer and therefore is not visible in the map.

Fig. 3.3.6 (b) demonstrates cascaded processes: $570 \div 680$ nm pump generates $470 \div 560$ nm signal and $620 \div 860$ nm idler. Signal from this process $470 \div 560$ nm acts as a pump to generate $450 \div 460$ nm signal and $480 \div 750$ nm idler. Further on $450 \div 460$ nm pump generates $430 \div 440$ nm signal and

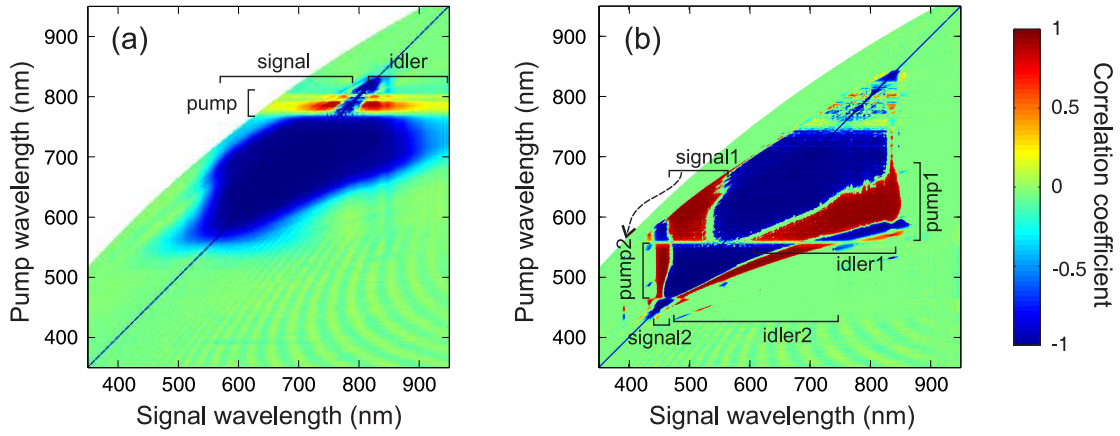

Figure 3.3.6: FWM correlation coefficient for Gaussian beam pumped supercontinuum (a) A case and (b) C case. White zones show phase matching constrains due to spectrometer detection interval.

$470 \div 500$ nm idler. The last cascade is not indicated in the figure due to small size.

3.3.3 Conclusions

We performed a comparative experimental study of femtosecond SC generation using Gaussian and Bessel beams carrying 130 fs pulses. In much contrast to previous results of SC generation with FBBs [175, 177], we obtain a smooth and modulation-free SC spectrum, whose characteristics are quite similar to SC characteristics generated by conventional Gaussian beams. More specifically, we demonstrate that dynamics of the spectral broadening in thin sapphire crystal (3 mm thickness) induced by a near-infrared (800 nm) low NA-focused Gaussian beam and axicon-generated FBB is rather similar, despite the 10 times larger input energy of the FBB, finally yielding smooth and featureless SC spectra with excellent shot-to-shot reproducibility. The observed similarity in spectral broadening dynamics suggests that the axial component of an FBB, as induced by noncollinear four-wave mixing, undergoes identical temporal dynamics as the input pulse in the case of a low-NA focused Gaussian beam.

An extensive statistical analysis of the SC spectral intensity fluctuations uncovers previously not observed statistical features of the spectral intensity across the entire wavelength range, as recorded at different stages of the spectral broadening by varying the input pulse energy. We disclose

a peculiar development of stability and instability regions within the SC spectra, which could be qualitatively associated with dynamics of the four-wave-mixing-induced spectral broadening. Specifically, we show that the disappearance of the correlations of intensity fluctuations at certain wavelengths is associated with the occurrence of distinct stability regions within the SC spectrum in the transient stages of the spectral broadening. In that regard, saturation of the spectral broadening is characterized by almost complete loss of spectral correlations, resulting in generation of spectrally flat SC with RMS fluctuations of the spectral intensity of less than 1% across the major part of the SC spectrum. The disclosed relationship between fluctuations of the SC spectral intensity and its spectral correlations offers an interesting topic for future studies of SC generation, which is still one of the most controversial topics in modern nonlinear optics.

3.4 Infrared extension of NIR pumped supercontinuum

There is a growing demand in producing femtosecond SC with large infrared extent, which is desirable for diverse spectroscopic applications and for development of few-optical-cycle near- and mid-infrared all-solid-state laser sources, which are exclusively based on optical parametric amplification, in particular [184, 185]. Experiments show that the infrared part of SC spectrum could be extended by means of pulse and beam shaping, as demonstrated in air [186–190], and simply by the use of loose focusing geometry in solids, see, e.g., [128, 191–193]. However, it is not explicitly understood which physical factors limit the infrared extent of the SC, especially in solid state media.

In this Section, we experimentally and numerically investigate the SC generation in sapphire with a standard 120-fs, 800-nm pumping under variable input beam focusing conditions. Our results show that loose focusing results in notable infrared extension of the SC spectrum. The numerical simulations are in good agreement with pulse splitting scenario of the SC generation and disclose that enhanced redshifted spectral broadening is related to increased nonlinear propagation of the leading sub-pulse after the pulse splitting event.

3.4.1 Supercontinuum generation in sapphire with variable focusing conditions

In the experiment, as the pump source, we used a 1 kHz repetition rate amplified Ti:sapphire laser system (Spitfire- PRO, Newport-Spectra Physics), which delivered 120 fs pulses with a central wavelength of 800 nm. The experimental setup is schematically depicted in Fig. 3.4.1. The laser beam was suitably attenuated, spatially filtered and reduced in size yielding 1.27 mm FWHM beam diameter on the focusing lens. In the experiment, we used three focusing lenses (L) with focal lengths of $f = +75\,\mathrm{mm}$, $f = +200\,\mathrm{mm}$ and $f = +400\,\mathrm{mm}$, which yielded the numerical apertures of 0.0169, 0.0064 and 0.0032, respectively. The SC was generated in 15-mm-long sapphire crystal, whose input face was always positioned at the beam waist. The input pulse energy was varied in the overall $0.3 - 3.0\,\mu\mathrm{J}$ range, and the input energy range in a particular focusing condition was chosen so as to capture the dynamics of spectral broadening in detail.

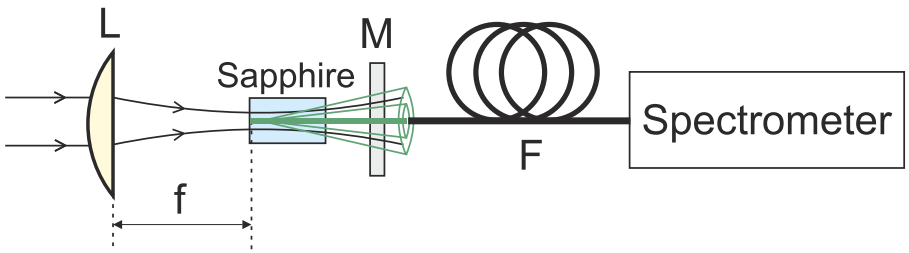

Figure 3.4.1: Experimental setup. See text for details.

Instead of recording the angle-integrated SC spectra, we selected only the axial part of the SC, which has low divergence and good focusability. Note that conical emission, which occurs as a result of group- and phase-matched four-wave mixing process that involves pulse splitting and X-wave generation [25] and whose angles are set by the phase-matching condition, i.e., by the material dispersion, carries a considerable portion of the SC energy. A comparison of angle-integrated and axial SC spectra shows that spectral intensity of angle-integrated SC is 2–3 orders of magnitude larger than spectral intensity of the axial SC part. The axial part of the SC was collected using high numerical aperture (NA = 0.22) fiber F with $400\,\mu\mathrm{m}$ core diameter (FT400EMT, Thorlabs), whose tip was located at 36 mm distance from the output face of sapphire crystal, thus ensuring acceptance angle of $\approx 0.8\,\mathrm{mrad}$. In this geometry, we efficiently coupled the axial part of the SC,

at the same time filtering out high-divergence conical emission. The axial SC spectrum was recorded by a home-built scanning prism spectrometer, which used Ge photodiode as a sensor with effective detection range from 500 nm to 1.7 μm. The intense SC radiation around the pump wavelength was attenuated by means of a dielectric mirror M, which had high reflectivity for 800 nm, and whose transmission function as well as sensitivity characteristics of the detector was then accounted for in reconstructing the actual SC spectra.

The dynamics of spectral broadening versus the input pulse energy under three different focusing conditions is illustrated in Fig. 3.4.2. After reaching a certain input pulse energy threshold, which depends on the focusing condition, the spectral broadening starts in an explosive manner. In our experimental settings, these thresholds are 0.4, 0.7 and 1.6 μJ, as measured with $f = +75$ mm, $f = +200$ mm and $f = +400$ mm focusing lenses, respectively. We observe different rates and different features of the blue- and redshifted spectral broadening. In all examined cases, the blueshifted broadening immediately covers all the visible range, with the blue cut-off wavelength at around 400 nm, as additionally verified using a standard fiber spectrometer (QE-65000, Ocean Optics) with 200–900 nm detection range (data not shown). The cut-off wavelength remains fairly constant and does not change with increasing the input pulse energy.

In contrast, the redshifted spectral broadening takes place at a slower pace and behaves in a different manner. Specifically, in all investigated cases, the redshifted broadening still continues with increasing the input pulse energy, and the red cut-off wavelength progressively shifts toward longer wavelengths with increasing focal length of the focusing lens. With $f = +75$ mm lens, the measured maximum spectral redshift is close to 1,200 nm, with $f = +200$ mm lens is at 1,450 nm, and with $f = +400$ mm lens exceeds 1,600 nm, as illustrated in more detail in Fig. 3.4.3.

In all examined cases, above a certain input pulse energy value, we observe an occurrence of distinct periodic spectral modulation, which is highlighted by plotting the spectral dynamics in a reduced dynamic range, as shown in Fig. 3.4.2(d)–(f) for better visual perception. The input energy thresholds for occurrence of the modulation are ~ 1.0, 1.4 and 2.3 μJ, as recorded with $f = +75$ mm, $f = +200$ mm and $f = +400$ mm focusing lenses, respectively. The occurrence of the spectral modulation is also correlated with a slight

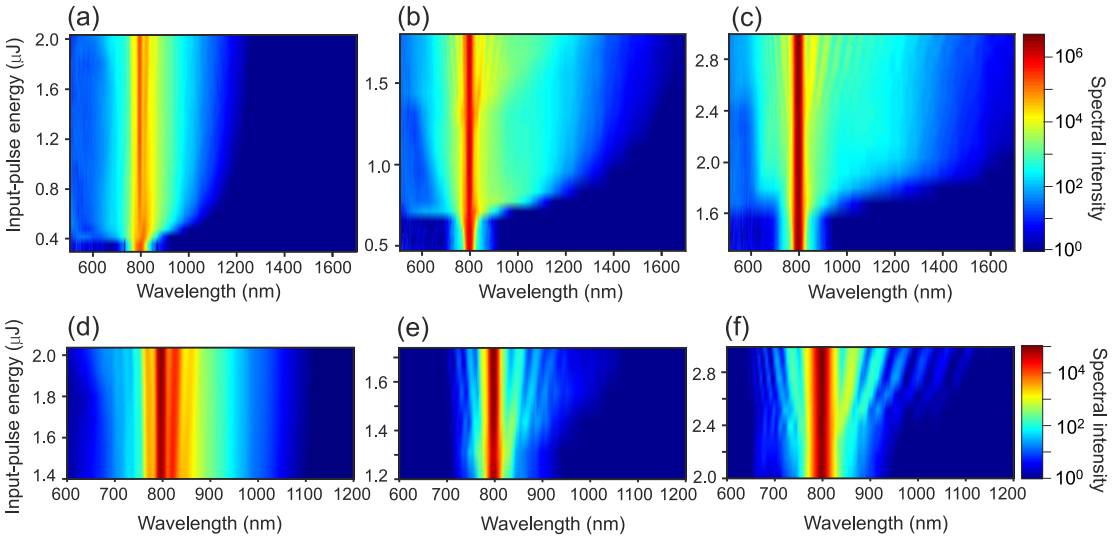

Figure 3.4.2: Experimentally measured dynamics of spectral broadening in sapphire versus the input-pulse energy as focused with: (a) f = +75 mm, (b) f = +200 mm, (c) f = +400 mm lenses. (d)-(f) show the respective occurrences of spectral modulations in a reduced dynamic range.

increase in spectral intensity of the blueshifted spectral components, as best seen in Fig. 3.4.2(b) and (c) and their enlarged parts in Fig. 3.4.2(e) and (f).

3.4.2 Numerical simulations

In order to explain the experimental observations and identify the relevant physical processes, we performed a series of numerical simulations using the input pulse and beam parameters as in the experiment. The numerical simulations were performed using the numerical model described in Sec. 1.1.

The evolution equation for the electron density was modified to account for saturating nonlinear absorption (considering neutral atom density) and plasma recombination:

$$\frac{\partial \rho}{\partial t} = \left(\frac{\beta^{(K)}}{K\hbar\omega_0} |A|^{2K} + \frac{\sigma}{E_g} \rho |A|^2 \right) \left(1 - \frac{\rho}{\rho_0} \right) - \frac{\rho}{\tau_r} \tag{3.4.1}$$

where E_g is the material bandgap and τ_r is the recombination time.

The numerical simulations were performed using 120 fs, 800 nm input pulses with FWHM widths of the input beam of 18, 47 and 94 μm that corre-

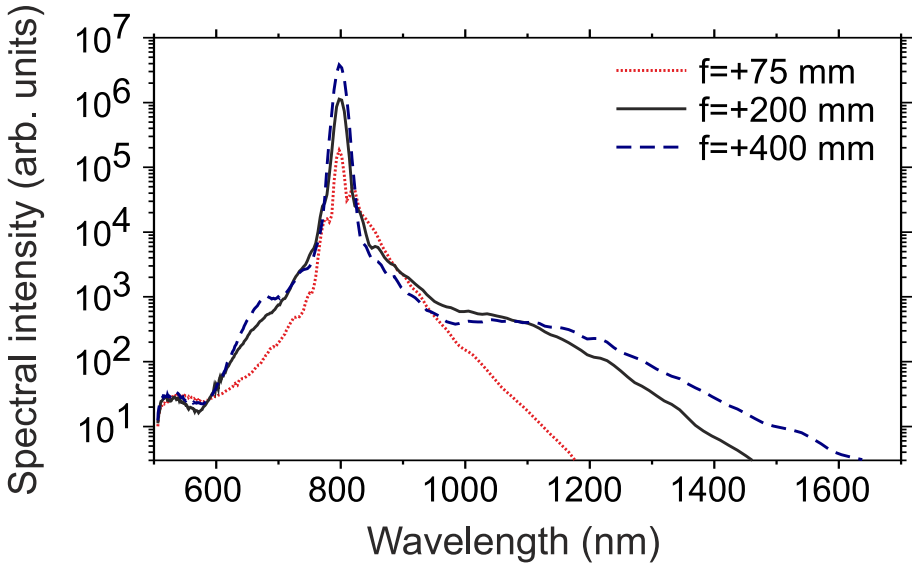

Figure 3.4.3: Comparison of the SC spectra measured at different focusing conditions. The input-pulse energies are 1.0 µJ, 1.1 µJ and 2.1 µJ, as correspond to f = +75 mm, f = +200 mm and f = +400 mm focusing, respectively.

sponded to 1.27 mm beam focusing with $f = +75\,\mathrm{mm}$, $f = +200\,\mathrm{mm}$ and $f = +400\,\mathrm{mm}$ lenses, respectively, as used in the experiment. A following set of material parameters was used: the full material dispersion was taken from Sellmeier equation provided in [194], the nonlinear refractive index $n_2 = 2.7 \times 10^{-16}\,\mathrm{cm^2W^{-1}}$, neutral atom density $\rho_0 = 2.3512 \times 10^{22}\,\mathrm{cm^{-3}}$ [195], multiphoton absorption order $K = 7$ was found assuming the bandgap of $E_g = 9.9\,\mathrm{eV}$ [195] and photon energy of 1.55 eV, the multiphoton absorption coefficient $\beta^{(K)} = 4.3 \times 10^{-78}\,\mathrm{cm^{11}W^{-6}}$ was calculated using the formalism described in [63], electron collision time $\tau_c = 1.7\,\mathrm{fs}$, characteristic electron recombination time $\tau_r = 96\,\mathrm{fs}$, reduced electron-hole mass $m = 0.3m_e$ [196] and cross-section for inverse bremsstrahlung $\sigma = 6 \times 10^{-22}\,\mathrm{m^2}$.

The results of numerical simulations, illustrating the dynamics of spectral broadening under different input beam focusing conditions, are presented in Fig. 3.4.4. Despite a slight difference in the experimental and numeric input pulse energy values, which are associated with relevant events in spectral broadening, the numerical simulations reproduce the experimental data in every detail. About 30–50 % higher experimental input energy values could be attributed to slight deviation of the real beam/pulse shapes from ideal Gaussian intensity profiles.

In order to explain the dynamics of spectral broadening and distinct spectral

features, such as emergence of spectral modulation in particular, we first refer to the temporal transformations of the filamenting pulse. Taking the input pulse with energy of 1.1 μJ, which is focused by $f = +200$ mm lens, as an exemplary case, in Fig. 3.4.5(a), we plot the temporal dynamics of the pulse versus propagation distance, while in Fig. 3.4.5(b) we present the corresponding dynamics of spectral broadening. The results of numerical simulation confirm the time-domain scenario of spectral broadening and SC generation via pulse splitting [12], which is a generic effect in media with normal group velocity dispersion [197] and has been experimentally observed in various nonlinear media in the ultraviolet, visible and near-infrared spectral range, see, e.g., [46, 51, 79, 131, 132] .

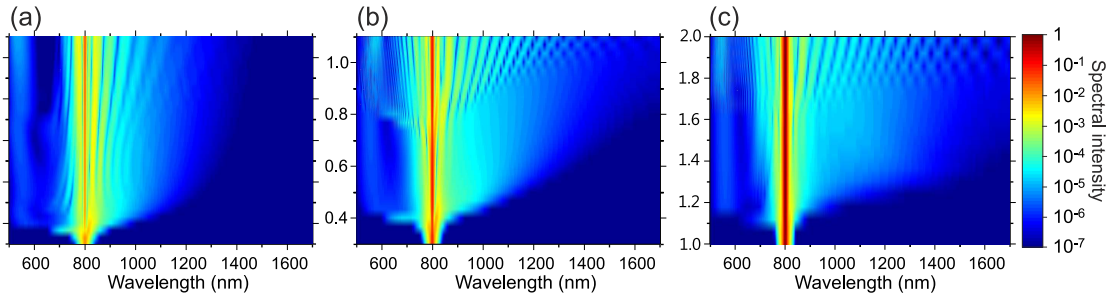

Figure 3.4.4: Numerically simulated dynamics of spectral broadening in sapphire versus the input-pulse energy as focused with: (a) f = +75 mm, (b) f = +200 mm, (c) f = +400 mm lenses.

An immediate blueshifted spectral broadening is associated with emergence of the intense trailing sub-pulse after the pulse splitting event at $z = 3.5$ mm. The intensity of the trailing sub-pulse becomes quickly clamped at $15 - 16\,\mathrm{TW/cm^2}$ due to combined action of the nonlinear absorption and plasma formation and thereafter rapidly decreases due to dispersive spreading in few tenths of millimeters of propagation. The intensity of the leading sub-pulse is somewhat smaller [see Fig. 3.4.6(d) for more details], and its temporal broadening is slower due to reduced group velocity dispersion at the vicinity of the zero group velocity dispersion point at around 1.3 μm. Therefore, the less intense leading sub-pulse experiences a longer distance of nonlinear propagation that in turn results in gradual redshifted spectral broadening, which continues after the pulse splitting event. During further propagation, the central temporal peak is replenished and then refocused [3, 85], and the refocusing cycle ends-up with a secondary pulse splitting event, which in present case occurs at $z = 7$ mm. The leading and trailing sub-pulses produced by the secondary splitting event undergo very similar

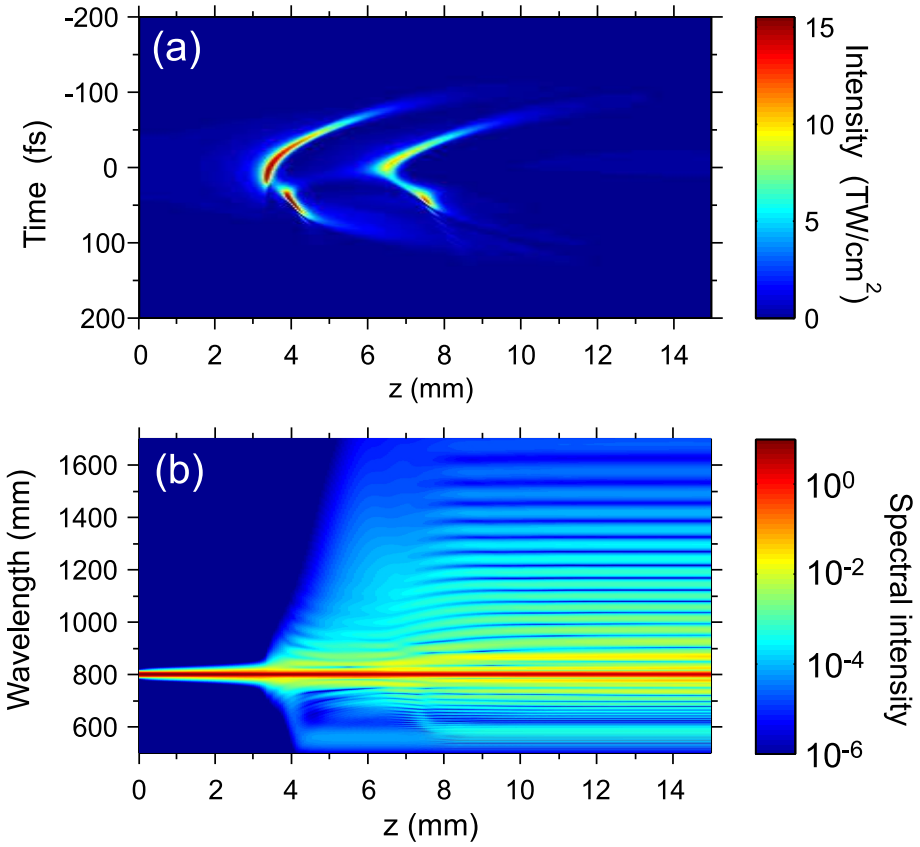

Figure 3.4.5: Numerically simulated (a) temporal and (b) spectral evolution of 1.1 µJ, 120 fs filamenting pulse in sapphire as focused with f = +200 mm lens.

dynamics of the spectral broadening and interfere with those produced after the first splitting event, thus yielding a periodic spectral modulation across the SC spectrum [79]. The second splitting event also produces a small burst of axial SC in the visible range and slight enhancement of the redshifted broadening, which is captured experimentally as well, however, the temporal structure of the SC becomes rather complex. The described scenario holds for all investigated cases; note also that decreasing of the numerical aperture extends the input pulse energy range between the first and second pulse splitting events. Note also a generic change in the spectral intensity of the blueshifted axial spectral components, which occurs with each pulse splitting event, initially generated strong axial radiation and then ceases due to pulse-front steepening and X-wave generation [25]. As in practical SC generation schemes, the input pulse energy is usually chosen so as to avoid the secondary pulse splitting; in our further analysis, we restrict ourselves to the input pulse energy range, which produces a single splitting event and smooth SC spectrum. More specifically, we investigated the dynamics of the redshifted spectral broadening in more detail for the input pulse en-

ergies of 0.4, 0.6 and 1.4 μJ, as focused by $f = +75$ mm, $f = +200$ mm and $f = +400$ mm lenses, respectively. Figure 3.4.6 compares the dynamics of the peak intensities of the leading (at a negative time) and trailing (at a positive time) sub-pulses versus propagation distance under different focusing conditions.

The fast rise and fall of the trailing sub-pulse intensity takes place in just few tenths of mm of propagation, and its peak intensity is always clamped at the same value of $15 - 16\,\mathrm{TW/cm^2}$, hence resulting in identical spectral blueshift, regardless on the input beam focusing condition. Variation in the focusing condition changes just the propagation distance within the nonlinear medium, where the pulse splitting event occurs, as seen from Fig. 3.4.6. In contrast, the behavior of the peak intensity of the leading sub-pulse, which is responsible for the redshifted spectral broadening, is markedly different and strongly depends on the focusing condition. The peak intensity of the leading sub-pulse is generally lower right after the pulse splitting event; however, when decreasing the focal length of the focusing lens, the propagation distance over which the leading sub-pulse keeps localized increases, as seen from Fig. 3.4.6(d), thus resulting in progressive redshifted spectral broadening. The propagation distance of the leading sub-pulse also slightly increases by increasing the input pulse energy, until the secondary pulse splitting event occurs. The blueshifted spectral broadening is mainly contributed by a very steep descending slope (the trailing front) of the trailing sub-pulse, in line with the results of Gaeta [12]. Both ascending and descending temporal slopes of the trailing sub-pulse do not change when varying the focusing condition. Therefore, the observed enhancement of redshifted spectral broadening could be mainly associated with the ascending temporal slope (leading front) of the leading sub-pulse, whose dynamics strongly depends on the focusing condition. In loose focusing condition ($f = +400$ mm lens), the steepness of ascending temporal slope of the leading sub-pulse is somewhat larger, and the leading sub-pulse preserves its high intensity and steep ascending front at least for an additional millimeter of propagation.

3.4.3 Conclusions

In conclusion, we have investigated the SC generation with 120 fs, 800 nm pulses in sapphire under variable focusing conditions. We experimentally

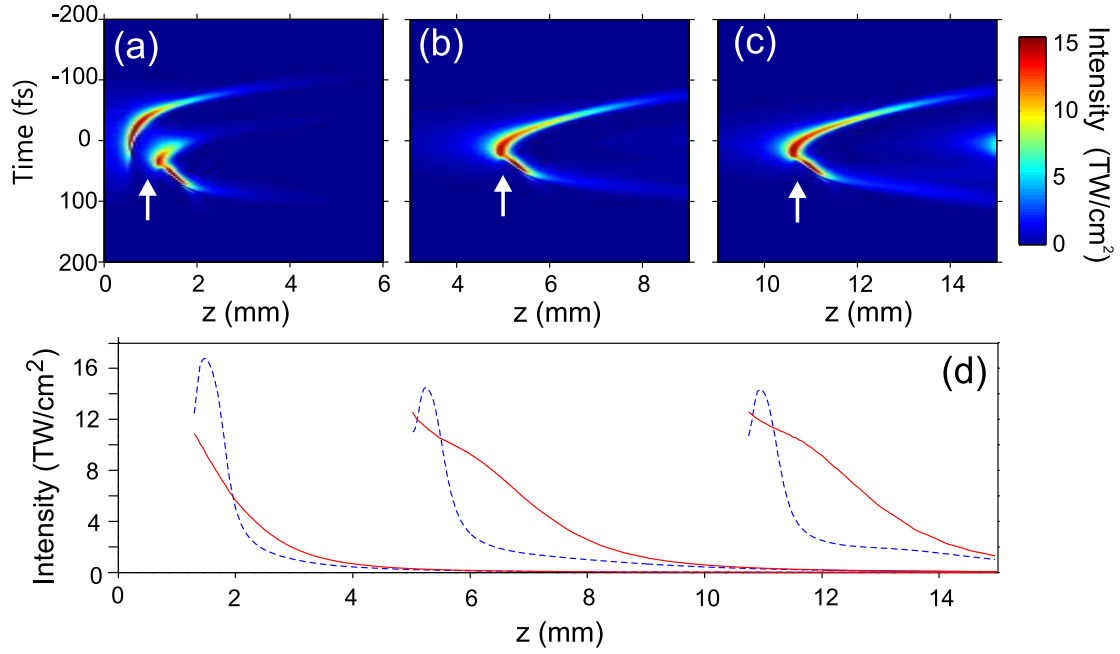

Figure 3.4.6: Temporal evolution of the filamenting pulse, as the input-beam is focused by (a) f = +75 mm, (b) f = +200 mm, (c) f = +400 mm lenses. Arrows indicate pulse splitting events. (d) summarizes the respective peak intensity dynamics of the leading (red solid curves) and trailing (blue dashed curves) sub-pulses.

demonstrated that changing the input beam focusing condition from tight to loose, the infrared extent of the SC increases significantly. The numerical simulations reproduced the experimental results in great detail, confirming the time-domain scenario of the SC generation, which is based on pulse splitting in normally dispersive nonlinear medium. In particular, we showed that the red- and blueshifted broadenings of the SC spectrum are related to intensity dynamics and pulse-front evolution of the leading and trailing sub-pulses, respectively, and we found that focusing condition affects only the dynamics of the leading sub-pulse. Therefore, the maximum blueshift of the SC spectrum remained fairly constant regardless of the focusing condition, while in contrast, enhanced redshifted spectral broadening was achieved in loose focusing condition as a result of increased nonlinear propagation of the leading sub-pulse, which preserves a steep ascending front. We also show that the secondary pulse splitting, which occurs as a result of spatial replenishment and filament refocusing, produces periodic modulation in the SC spectrum due to interference between the primary and secondary split pulses with overlapping spectra. Our results are relevant for better

understanding the temporal dynamics that lead to SC generation and for optimization of ultrafast SC generators based on wide bandgap dielectric media.

4 Filamentation of highly elliptical laser beams

Material related to this chapter was published in [A1, A2]

Physics behind the femtosecond filaments covers exciting fundamental topics [3, 4] and foresees a number of relevant applications, which range from the atmospheric research [29] to permanent refractive index modification in bulk solid state media [30, 198, 199] for optical waveguiding and synthesizing of photonic structures and excitation of the arrays of coherent lasing sources [200, 201]. When the beam power well exceeds the critical power for self-focusing, the beam breaks-up into multiple filaments (MFs) [202–204]. The nature of the multiple filamentation process is described in terms of growth of wave-front perturbations (known as transverse modulation instability) and leads to random filament distribution over a given transverse plane. Multiple filaments originating from a single input beam exhibit high coherence properties and serve as a source of multichannel white-light radiation[205], or may be used for phase-matched ultrafast Raman frequency conversion [206], production of plasma channels [207] and guiding of microwave radiation [208]. However, most of the applications require precise filament localization and high MF pattern reproducibility.

Many experimental methods and tools allowing control of the MF arrays have been developed recently, suggesting a wide choice of techniques, ranging from a simple modification of the input-beam parameters (e.g. induced astigmatism via tilted lens or deformable mirror, circular beam polarization) to a precise all-optical control [209–219] . A particularly interesting case of the multiple filamentation refers to spontaneous break-up of intense elliptical laser beams, which yields reproducible and periodic MF patterns, despite the fact that the break-up process is initiated by random intensity modulation across the beam [220–224].

The break-up of elliptical laser beams is universal, and regular MF patterns had been experimentally observed in water [220], air [225], carbon

disulfide [221], BK7 glass [222], and fused silica [223]. Regardless of the physical state of the nonlinear medium (solid, liquid or gas) even slight input beam ellipticity overcomes the random nature of the beam break-up and results in deterministic and highly reproducible MF patterns. It was recently demonstrated that in the case of large beam ellipticity, light filaments evolve along the major axis of the beam with constant spacing thus forming a periodic one-dimensional MF array [224]. Despite of a wide range of potential applications based on the periodicity of the MF array, specific factors determining the period has not been explicitly studied yet. The major question still concerns the distance between the adjacent filaments and the whole period of the MF array.

In this chapter we demonstrate that self-focusing of high power beams with large ellipticity leads to formation of periodic and highly reproducible MF arrays. The observed periodicity could be controlled by the input beam intensity and is explained within the framework of phase-matched degenerate noncollinear multistep four-wave mixing and parametric amplification of certain components occurring in the spatial spectrum of the self-focusing laser beam.

Secondly, we study experimentally and numerically the spatiotemporal dynamics of the multiple filament arrays excited by self-focusing of intense elliptical laser beams in fused silica. Our results demonstrate that although multiple filament arrays emerge as apparently regular patterns in the space domain, the spatiotemporal dynamics of the individual filaments is governed by the input-beam power and the input-beam ellipticity. In the case of moderate input-beam ellipticity, the individual filaments propagate in curved trajectories arising from skewed (spatiotemporal) coherence. The spatiotemporal propagation dynamics is regularized by increasing the input-beam ellipticity, and in part due to permanent modifications of fused silica that occur under intense irradiation. In this case, strong pulse reshaping and shock-front generation is observed, which yields a regular array of very short ($< 5\,\mathrm{fs}$) superluminally propagating localized peaks in the leading front, followed by the sub-pulses centered on the input-pulse top, and trailed by subluminally propagating pulses with rather complex transverse intensity distribution.

Although a significant progress in control and regularization of the MF arrays has been achieved in practice, many aspects of the spatiotemporal dy-

namics, which takes place within the MF array in dense dispersive media, are still poorly investigated. The knowledge of temporal, and more generally speaking, spatiotemporal behavior of the individual light filaments comprising the MF array is vital for understanding and optimization of the energy deposition in light and matter interactions. Therefore the aim of this chapter is to study the spatiotemporal dynamics that emerges in the MF regime, set by self-focusing of femtosecond elliptical laser beams in fused silica. For this purpose we applied the three dimensional mapping technique (see Sec. 1.3) with high temporal (30 fs) and spatial (5 μm) resolution, which enables to precisely reconstruct the spatiotemporal intensity profiles of the light pulses within the entire MF array. Numerical simulations qualitatively reproduce the experimental results and helps to identify some of the key physical mechanisms behind the space-time dynamics of multiple filamentation process.

4.1 Generation of periodic multifilament arrays

4.1.1 Experimental results

The experiment was performed using 1 ps, 1054 nm pulses from a chirped-pulse amplification technique based Nd:glass laser system (Twinkle, Light Conversion Ltd.) operating at 10 Hz repetition rate. The laser output was frequency doubled, spatially filtered to yield a clean Gaussian beam profile and focused by a cylindrical lens ($f_x = \infty$, $f_y = 750\,\mathrm{mm}$) onto the input face of the UV-grade (type KU-1) fused silica sample. The beam at the sample input had FWHM dimensions $a_x = 1.3\,\mathrm{mm}$, $a_y = 170\,\mu\mathrm{m}$ and its intensity distribution is depicted in Fig. 4.1.1(a). The output face of the sample was imaged onto a CCD camera (COHU-6612, pixel size $9.9\,\mu$m, 10-bit dynamic range, linked to a Spiricon LBA-400PC frame grabber) by means of an achromatic lens with 3.4× magnification. Power (energy) of the incident beam was varied by means of a half-wave plate and a thin-film polarizer. In the experiment we used 8-mm and 45-mm long fused silica samples so as to investigate the beam break-up at fairly different intensity range.

With increasing the input energy, the input elliptical beam propagating in a 45-mm-long sample first experiences one-dimensional self-focusing along

its short axis dimension forming a narrow light stripe of $\sim 25\,\mu$m FWHM diameter. The beam filamentation starts at $E_{\text{in}} = 75\,\mu$J, which corresponds to the input peak intensity of $I_0 = 28\,\text{GW/cm}^2$, that is $52P_{\text{cr}}$ in terms of critical power for self-focusing [$P_{\text{cr}} = 3.77\lambda^2/(8\pi n n_2)$]. Multiple filaments having individual FWHM diameter of $\sim 20\,\mu$m emerge along the long-axis of the beam as shown in Fig. 4.1.1(b). An average distance between adjacent filaments keeps fixed to a high degree for a given input energy. The MF pattern is reproduced with each laser shot and each individual filament retains its position with accuracy better than $3\,\mu$m that is the detection accuracy set by the imaging system and the resolution of the CCD camera. Further increase of the input energy leads to the increased number of the individual filaments, which extend outwards the beam center as well as to the reduced period (from 86 μm at $I_0 = 28\,\text{GW/cm}^2$ to 57 μm at $I_0 = 45\,\text{GW/cm}^2$). With the input intensity $I_0 > 45\,\text{GW/cm}^2$ we observed a formation of distinct secondary MF bands parallel the main MF array as depicted in Fig. 4.1.1(c). At even higher input intensity ($I_0 > 60\,\text{GW/cm}^2$), MF array losses its strict periodicity and shot-to-shot reproducibility as a result of interactions between the individual filaments.

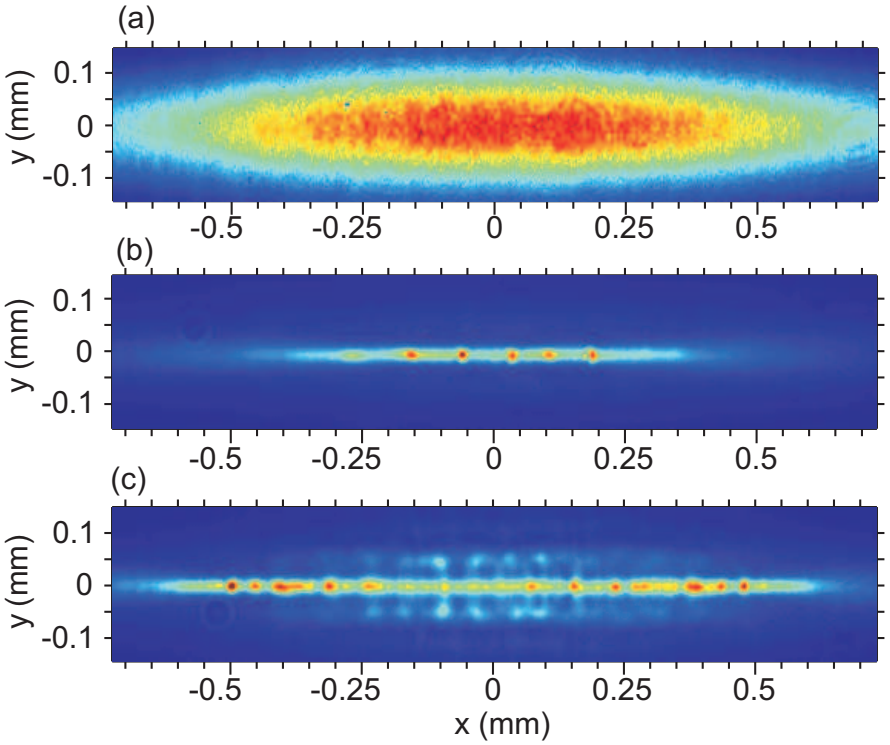

Figure 4.1.1: Near-field intensity distribution of (a) input beam and output beam after the nonlinear propagation in 45-mm-long fused silica sample with (b) $I_0 = 32$ GW/cm^2 and (c) $I_0 = 58$ GW/cm^2.

In order to investigate the very first stage of the MF array formation, we have performed a complimentary experiment under a different focusing condition and in a shorter (8-mm) fused silica sample. Here, we focused a laser beam with $f_x = \infty$, $f_y = 100\,\text{mm}$ cylindrical lens, yielding FWHM dimensions of the $a_x = 1.3\,\text{mm}$ and $a_y = 20\,\mu\text{m}$. The smaller dimension of the input beam, i.e. a_y, almost exactly matched that of a single filament, hence no apparent beam contraction along the short axis over a sample length took place in this case. The results are depicted in Fig. 4.1.2 by plotting a central cross section of the beam along its long-axis. In this case we observe how with increasing the input energy the initial noise present in the input beam [Fig. 4.1.2(a)] develops into a well-defined multipeaked structure [Fig. 4.1.2(b,c)] that eventually forms a one-dimensional MF array [Fig. 4.1.2(d)]. We note that the input intensity range ($I_0 = 0.31 - 0.48\,\text{TW/cm}^2$) in the present experiment was very much different from the previous one, therefore the measured period was sufficiently smaller (in the range of $35 \div 45\,\mu\text{m}$, depending on the input intensity). Despite a different initial focusing condition, the MF pattern showed an excellent shot-to-shot reproducibility both in position of the individual filaments and in periodicity.

4.1.2 Numerical simulations of the multiple filamentation dynamics

Space domain studies of the ultrashort pulse filamentation could be successfully performed using continuous-wave models [226]. In this Section we study multiple filamentation dynamics of monochromatic elliptical laser beam by solving the nonlinear Schroedinger equation, which accounts for diffraction, self-focusing and multiphoton absorption [17] and compared to theoretical model in Sec. 1.1 does not account for dispersion (as it is continuous-wave model), non-paraxial and generated plasma effects:

$$\frac{\partial A}{\partial z} = \frac{i}{2k}\Big(\frac{\partial^2}{\partial x^2} + \frac{\partial^2}{\partial y^2}\Big)A + \frac{i\omega n_2}{c}|A|^2 A - \frac{\beta^{(K)}}{2}|A|^{2K-2}A, \tag{4.1.1}$$

where z is the propagation distance, ω is the carrier frequency, $k = n_0\omega/c$ is the wave number, n and n_2 are the linear and nonlinear refractive indexes, respectively, $\beta^{(K)}$ is the multiphoton absorption coefficient with K being

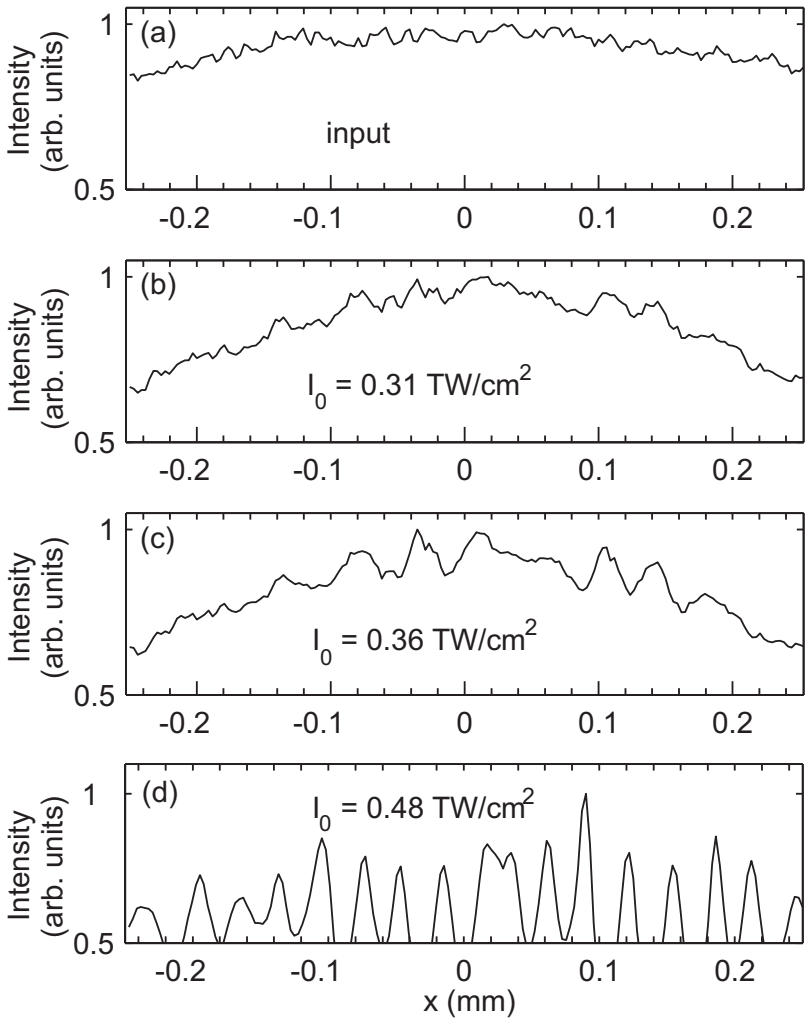

Figure 4.1.2: Central cross section of the beam: (a) at the input and (b)–(d) at the output of a short, 8-mm-long fused silica sample at different input intensity.

the order of the multiphoton absorption. A is the complex amplitude of the electric field, defined at the input ($z = 0$) as

$$A_{\text{in}}(x, y) = A_0 \exp\Big[-2 \ln 2 \Big(\frac{x^2}{a_x^2} + \frac{y^2}{a_y^2} \Big) \Big], \tag{4.1.2}$$

where a_x and a_y are FWHM beam widths along x and y axes, respectively. Eq. (4.1.1) was solved numerically by split-step Fourier method with $\lambda = 527\,\text{nm}$, $n_0 = 1.46$, $n_2 = 2.24 \times 10^{-20}\,\text{m}^2/\text{W}$, $K = 3$, $\beta^{(3)} = 1 \times 10^{-23}\,\text{cm}^3/\text{W}^2$, taking the input beam dimensions a_x and a_y as in the experiment. We have also added 5% amplitude noise on the input beam profile, which is very close to that evaluated experimentally, as seen from

the input beam cross-section plotted in Fig. 4.1.2(a). From the numerical simulations we have verified that the initial amplitude of the added noise (in the range of $1 \div 10\%$) does not greatly alter the final result (MF period in particular), at least in the applied power range, what is in good agreement with the recent study concerning multiple filamentation of circular laser beams [226]. The input intensity I_0 was varied from $30\,\mathrm{GW/cm^2}$ to $600\,\mathrm{GW/cm^2}$ so as to cover the range of experimental values.

Fig. 4.1.3(a)-(c) illustrates few examples of the near field intensity distribution of the beam *vs* propagation distance at $I_0 = 32\,\mathrm{GW/cm^2}$. The elliptical input beam [Fig. 4.1.3(a)] propagating in the nonlinear medium experiences 1-dimensional self-focusing along its short (y) axis [Fig. 4.1.3(b)] and eventually breaks-up into 1-dimensional array of regularly spaced light filaments [Fig. 4.1.3(c)]. The numerically simulated propagation dynamics are qualitatively consistent with recent experimental observations of the beam propagation dynamics in water [224]. Fig. 4.1.3(d) plots the near field intensity distribution at $I_0 = 58\,\mathrm{GW/cm^2}$, illustrating the formation of two-dimensional MF array. The simulated MF patterns at the output of the sample ($z = 45\,\mathrm{mm}$) reproduce those recorded in the experiment, as shown in Fig. 4.1.1. More detailed comparison between the numerical and experimental data is accomplished in terms of the MF array period, with the results being summarized in the subsection 4.1.4.

Fig. 4.1.4 illustrates the dynamics of the far field spectra plotted in (k_x, k_y) space, each of these correspond to the near field images presented in Fig. 4.1.3 (a)-(c). These plots demonstrate how the wave vector spectrum of the input beam [Fig. 4.1.4(a)] notably broadens along k_y direction as a result of self-focusing [Fig. 4.1.4(b)], while the occurrence of distinct sidebands along k_x direction [Fig. 4.1.4(c)] triggers the beam break-up into multiple filaments. The position of the sidebands determines the period of the MF array. Closer inspection revealed that the position of the sidebands is in fair agreement with the standard modulational instability theory, which associates the break-up of intense laser beams into multiple filaments with the growth of perturbations present in the input beam wavefront by means of the four-wave parametric mixing process, as described in detail in[81].

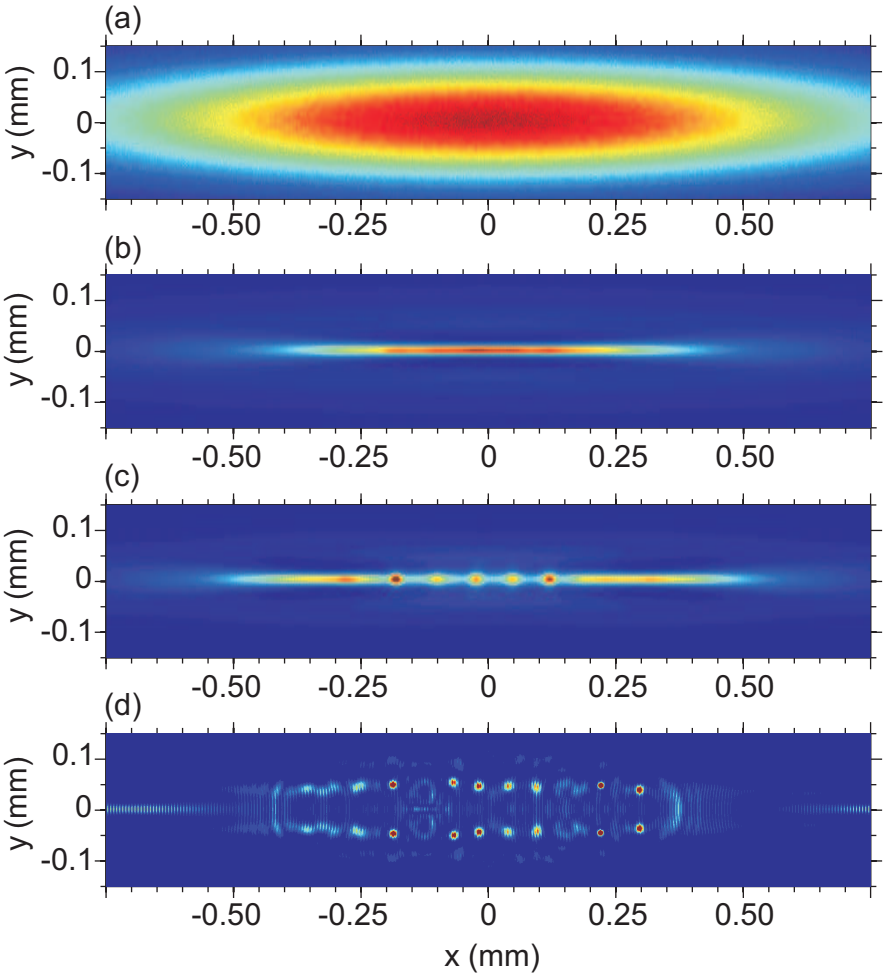

Figure 4.1.3: Numerical simulation of intense laser beam propagation in fused silica. Normalized near field intensity profile (a) at the input ($z = 0$ mm), (b) inside ($z = 40$ mm), and (c) at the output ($z = 45$ mm) of the sample at $I_0 = 32$ GW/cm^2. (d) shows the output beam profile at $I_0 = 58$ GW/cm^2.

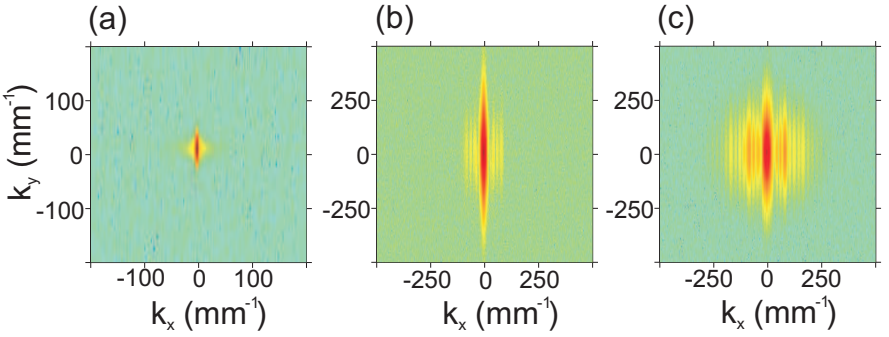

Figure 4.1.4: Far-field intensity distribution (on a logarithmic intensity scale) plotted as (k_x, k_y) spectra, corresponding to images shown in Fig. 4.1.3(a)-(c).

4.1.3 Multistep four-wave mixing model

Several alternative ways have been proposed to describe multiple filamentation phenomena without numerical integration and which provide useful insights into the underlying physics. In particular, a classical approach is based on the theory of modulational instability [81], while the most recent work considers ray racing adopted to a nonlinear optical system [227]. In what follows, we introduce a simple analytical model, which explains multiple filamentation as a sole result of the multistep four-wave parametric interactions, occurring in the self-focusing high power elliptical laser beam and reproduces in detail the basic features of experimentally observed one- and two-dimensional MF arrays.

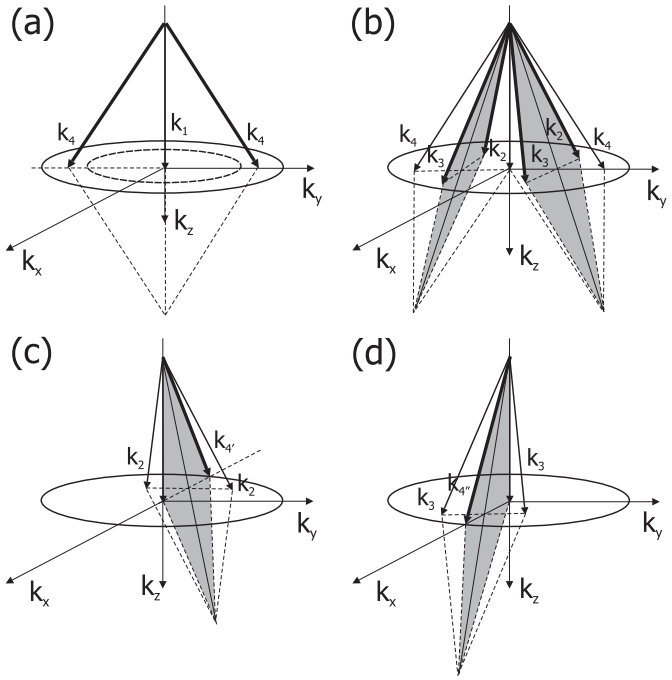

Figure 4.1.5: Schematic illustration of the multistep four-wave mixing process in $k-$space. The resulting wave vectors in each step are depicted by bold arrows. Shaded areas indicate that the resulting vectors lie in a different plane than the initial ones. See text for description.

The schematic step-by-step representation of the interacting wave vectors is shown in Fig. 4.1.5. Suppose an input monochromatic elliptical Gaussian beam with the central wave vector $\vec{k}_1$, while its full $k-$vector spectrum is confined within an ellipse depicted by a dashed line in the (k_x, k_y) plane, as shown in Fig. 4.1.5(a). In the first step, an input elliptical beam experiences self-focusing, which leads to enrichment of its wave vector spectrum by new components (within an ellipse depicted by a solid line) with a pair of vectors

$\vec{k}_4$ among them, so that the non-collinear phase matching condition for the four-wave parametric amplification.

$$\vec{k}_1 + \vec{k}_1 = \vec{k}_4 + \vec{k}_4 \tag{4.1.3}$$

becomes satisfied, where

$$|\vec{k}_1| = \frac{2\pi}{\lambda_0}(n_0 + n_2 I_0), \tag{4.1.4}$$

$$|\vec{k}_4| = \frac{2\pi}{\lambda_0}(n_0 + 2n_2 I_0), \tag{4.1.5}$$

are the wave vectors, modified via local refractive index change due to the optical Kerr effect. Assuming the monochromatic case and frequency-degenerate interaction, the modulus of $\vec{k}_1$ is modified as a result of the self-phase modulation, and which thus modifies the modulus of a weak signal $\vec{k}_4$ via cross-phase modulation. Here $\lambda_0 = 527$ nm denotes the central wavelength of the laser radiation. Note that vectors $\vec{k}_1$ and $\vec{k}_4$ lie in the (k_y, k_z) plane with their endpoints located along k_y axis. The second step considers four-wave interaction between $\vec{k}_1$ and $\vec{k}_4$, which gives rise to occurrence of wave vectors $\vec{k}_2$ and $\vec{k}_3$ as illustrated in Fig. 4.1.5(b):

$$\vec{k}_1 + \vec{k}_4 = \vec{k}_2 + \vec{k}_3. \tag{4.1.6}$$

Here $|\vec{k}_2| = |\vec{k}_3| = |\vec{k}_4|$. Note that the resultant vectors $\vec{k}_2$ and $\vec{k}_3$ lie in a tilted plane [perpendicular to (k_y, k_z)], which is indicated by gray shading. The endpoint locations of vectors $\vec{k}_2$ and $\vec{k}_3$ are symmetric with respect to principal axes k_x and k_y, respectively. In the third step, vectors $\vec{k}_2$ and $\vec{k}_3$ interact with the central vector $\vec{k}_1$:

$$\vec{k}_2 + \vec{k}_2 = \vec{k}_1 + \vec{k}_{4'}, \tag{4.1.7}$$

$$\vec{k}_3 + \vec{k}_3 = \vec{k}_1 + \vec{k}_{4''}; \tag{4.1.8}$$

$$|\vec{k}_{4'}| = |\vec{k}_{4''}| = |\vec{k}_4|,$$

so as $\vec{k}_{4'}$ and $\vec{k}_{4''}$ occur as shown in Fig. 4.1.5(c) and (d), whose endpoints are located along k_x axis. Strictly speaking, in the case of monochromatic waves, the phase matching conditions described by Eqs. 4.1.7 and 4.1.8 could be fulfilled only by introducing a nonzero phase mismatch Δk. In our experimental settings the phase mismatch was found to be negligibly small ($\Delta k \approx 4\,\mathrm{cm}^{-1}$), so the wave vectors $\vec{k}_{4'}$ and $\vec{k}_{4''}$ could be generated with still reasonable efficiency. And finally, $\vec{k}_{4'}$ and $\vec{k}_{4''}$ are parametrically amplified by the intense pump $\vec{k}_1$, in analogy with the first step:

$$\vec{k}_1 + \vec{k}_1 = \vec{k}_{4'} + \vec{k}_{4''}. \tag{4.1.9}$$

The phase-matched multistep four-wave processes therefore give rise to a particular set of wave vectors $\vec{k}_j$ ($j = 1, 2, 3, 4, 4', 4''$). Further we assume a set of monochromatic waves with central wave vectors $\vec{k}_j$ generated at different steps of the four-wave mixing process as replicas of the initial pump beam with the envelope A_{in} described by Eq. 4.1.2:

$$A_j(x, y) = C_j A_{\mathrm{in}}(x, y) \exp\left[i(k_{j,x}x + k_{j,y}y)\right], \tag{4.1.10}$$

where $k_{j,x}$ and $k_{j,y}$ are the respective projections of the wave vectors $\vec{k}_j$. Here arbitrary coefficients C_j represent weighted contributions to the amplitudes of each wave. The output intensity pattern is calculated as a superposition of waves described by Eq. 4.1.10:

$$I(x, y) = \left| \sum A_j(x, y) \right|^2. \tag{4.1.11}$$

Figure 4.1.6 illustrates the resulting intensity distribution calculated for different input beam intensities, and qualitatively reproduces the experimentally observed MF patterns and the occurrence of the secondary filament bands in particular. Values of C_j ($C_1 = 1.0, C_2 = C_3 = C_4 = 0.6, C_{4'} = C_{4''} = 0.4$) in our calculation were chosen so as to obtain a distinct visibility contrast in the resulting intensity distribution pattern. We note that in the present model C_j is a freely chosen parameter, which, however, has just a weak effect on the period of the MF array. Therefore periodic break-up of

the elliptical laser beam along its long axis is dictated by beating of the wave vector components along k_x axis, while the secondary MF bands originate from the beating of the wave vector components distributed along k_y axis. Here we also note that possible interactions between the neighboring filaments as well as the input beam contraction due to self-focusing are not accounted for. The effect of the latter is discussed in more detail in the following subsection.

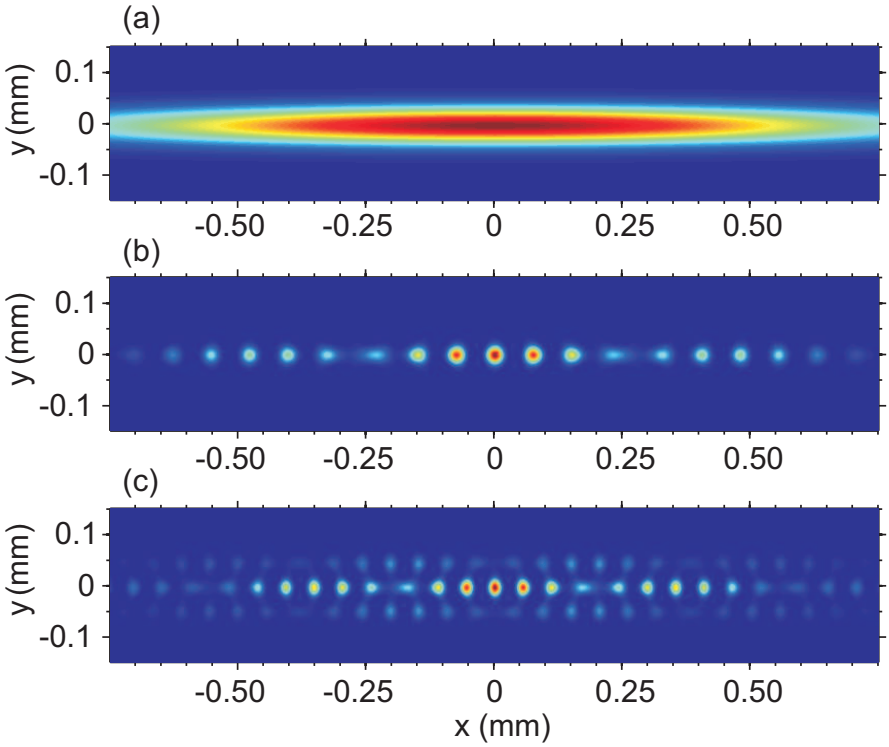

Figure 4.1.6: Numerical simulation using an analytical model: (a) input beam, (b) filament array formed at $I_0 = 90$ GW/cm^2 and (c) $I_0 = 170$ GW/cm^2.

4.1.4 Discussion and conclusions

For a qualitative comparison of the experimental data, numerical simulations and the results obtained using an analytical model, in Fig. 4.1.7 we plot the period of the MF array *vs* the input beam intensity. The data from the numerical model and the experiment coincide fairly well in the full range of the input intensities. It is worth mentioning that the MF period does not depend on the input beam ellipticity, defined as a_x/a_y, at least while the input beam ellipticity remains sufficiently large. In fact, these results suggest that the period of the MF array may be efficiently controlled via the input beam intensity. For what concerns the results obtained using

an analytical model, the general trend closely follows the results obtained for the beam break-up in planar waveguides [228]. However, the results of analytical model notably depart from the experimental and numerical data in the low intensity limit ($30 \div 60\,\mathrm{GW/cm^2}$), but fit the data well for high ($100 \div 600\,\mathrm{GW/cm^2}$) input intensities. These differences could be explained by the fact that the analytical multistep four-wave mixing model does not account for the beam propagation, where the input beam experiences notable contraction due to self-focusing prior to break-up. As a result, the initial intensity at which the multistep four-wave parametric processes are triggered, remains undefined. However, a quantitative agreement between the data in the intensity range of $30 \div 60\,\mathrm{GW/cm^2}$ could be achieved with scaling the input intensity in the analytical model by a factor of ~ 3, so as $I_0^{\mathrm{an}} = 3I_0^{\mathrm{exp}}$, which thus "compensates" for the intensity change due to the beam contraction. The resulting MF period after this adjustment is plotted by a bold dashed curve in Fig. 4.1.7. Conversely, in the high intensity limit, the input conditions are those that no beam contraction there occurs, and the results of the analytical model coincide very well with the numerical and experimental data.

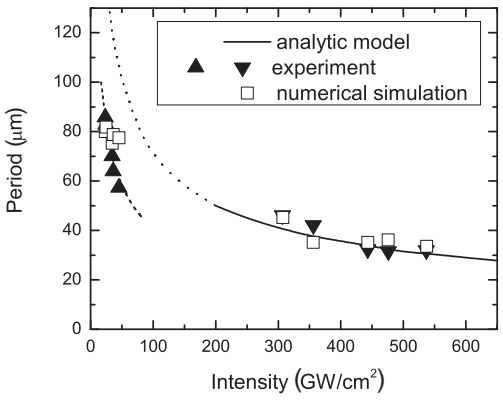

Figure 4.1.7: Period of the MF array *vs* the input beam intensity. Experimental data points are shown by solid triangles ▲ and ▼, while the results of the numerical simulation are illustrated by □. The results of the analytical model are plotted by curves, see text for details.

To summarize the results of above, we have demonstrated that intense highly elliptical laser beam breaks-up into periodic one- and two dimensional arrays of light filaments. Although the multiple filamentation is initiated by random amplitude noise, it forms highly reproducible periodic MF patterns, whose periodicity may be easily controlled via the input beam intensity. On simple physical grounds the observed periodicity in the MF array could be

understood within a simple analytical framework of phase-matched multi-step degenerate four-wave parametric interactions. The periodic break-up of the elliptical input beam is initiated by noncollinear nearly degenerate four-wave parametric amplification of certain wave vectors, which fulfill the phase-matching condition. The intensity dependence of the period in the MF array is explained as due to modification of the phase-matching condition by self- and cross-phase-modulation via nonlinear refractive index. The results of the analytical model well explain the experimental and numerical data at high input intensity and short nonlinear medium length, where the initial beam does not undergo contraction dynamics. The model is still feasible in explaining the results of the MF pattern formation in long samples with lower input intensity, however, a correction on the input beam intensity and diameter should be applied.

4.2 Spatiotemporal structure of multiple filament arrays

4.2.1 Experimental setup

As a laser source we have used an amplified Ti:sapphire laser system (Spitfire PRO-XP, Newport-Spectra Physics), which produces 130-fs, 3.5-mJ pulses with central wavelength of 800 nm at 1 kHz repetition rate. The experimental setup consisted of four blocks: (i) the generator of the MF array (test beam), (ii) the generator of a short probe pulse, (iii) the nonlinear gate and (iv) the data acquisition system, as schematically depicted in Fig 4.2.1. The laser output was split into two parts by a beam splitter BS1. The smaller portion (20%) of the laser radiation was made variable in energy by means of a half-wave plate ($\lambda/2$) and a polarizer P and focused using the cylindrical lens CL ($f_x = 500\,\mathrm{mm}$, $f_y = \infty$) onto the input face of 20-mm-long fused silica sample FS. The desired beam ellipticity was set using the beam-size reducing telescopes (not shown), while the input energy (power) was adjusted so as to excite a distinct MF array at the output of the sample. The larger portion (80%) of the laser radiation was frequency doubled and used to pump the non-collinear optical parametric amplifier (TOPAS-White, Light Conversion Ltd.), which produced 30-fs, 10-μJ probe pulse with central wavelength of 720 nm. Its output beam was spatially filtered to obtain a smooth Gaussian profile with FWHM diameter

of 4 mm. The generated MF array (test beam) was combined with the probe pulse by means of a dichroic mirror BS2 and sent to 20 μm thick, type I phase-matching BBO crystal, cut at $\theta = 29.2°$, which served as a nonlinear gate NG. The small crystal thickness was chosen so as to achieve a broadband phase-matching for sum-frequency generation in the undepleted pump regime and to minimize the temporal and spatial walk-off effects between the test and probe pulses and beams. A small angle of 2° between the test and probe beams was introduced to spatially separate the sum-frequency (cross-correlation) signal from the input beams and their second harmonics. The acquisition system consisted of a CCD camera (pixel size 4.65 μm, 8-bit dynamic range, JAI A1) and a filter F that blocked the infrared radiation. The sum-frequency signal (with a central wavelength of 379 nm) was imaged onto the CCD sensor with 2× magnification by means of the imaging lens IL. By changing the time delay between the test and probe beams in 12 fs step, a collection of the cross-correlation images was acquired, and which was used to reconstruct the spatiotemporal intensity profile of the test beam with 30 fs temporal and 5 μm spatial resolution.

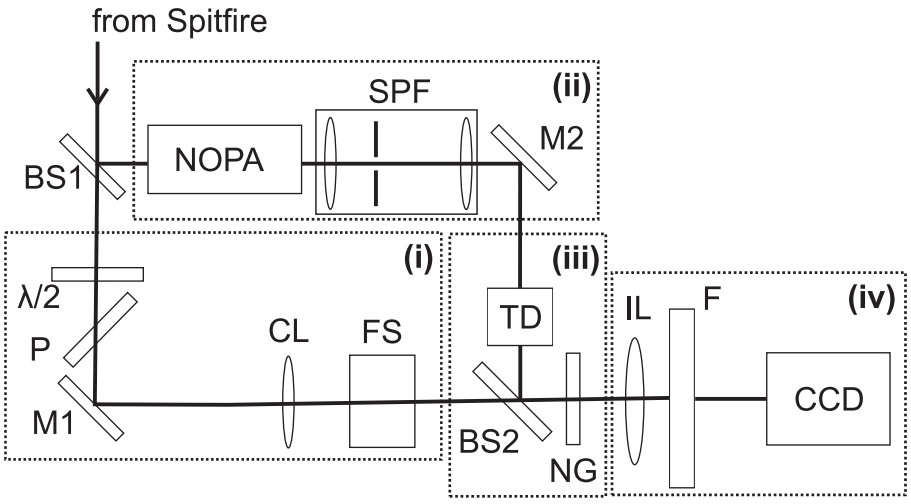

Figure 4.2.1: Experimental setup. NOPA is the non-collinear optical parametric amplifier, FS is the fused silica sample, TD is the time delay line, $\lambda/2$ is the half wave plate, P is the polarizer, BS1, BS2 are the beam splitters, CL is the cylindrical lens, SPF is the spatial filter, IL is the imaging lens, F is the filter, NG is the nonlinear gate, CCD is the charge coupled device.

4.2.2 Numerical model

The propagation dynamics of the ultrashort-pulsed elliptical light beams was studied using one-directional propagation equation for the linearly po-

larized wave with the complex envelope, see Sec. 1.1 for details. The calculations were performed for $t_p = 130\,\mathrm{fs}$ pulses with central wavelength $\lambda_0 = 800\,\mathrm{nm}$, using the following relevant parameters of the fused silica: $n_0 = 1.45$ and the full dispersion relation from [229], $n_2 = 2.8 \times 10^{-16}\,\mathrm{cm^2/W}$ [230], $E_g = 7.8\,\mathrm{eV}$, and $K = 6$, assuming a single photon energy $\hbar\omega_0 = 1.5\,\mathrm{eV}$. The parameters of the electron plasma were evaluated using the formalism described in [63], which yielded the six photon absorption coefficient $\beta^{(6)} = 1.1 \times 10^{-66}\,\mathrm{cm^9/W^5\,m^2}$, taking the electronic collision time in the conduction band $\tau_c = 1.7\,\mathrm{fs}$ [37].

The input-pulse was defined as an elliptical Gaussian beam characterized by FWHM beam widths a_x and a_y along x and y axes, respectively, and by FWHM pulse duration t_p:

$$A(t, x, y, z = 0) = A_0 \exp\left[-2\ln 2\left(\frac{t^2}{t_p^2} + \frac{x^2}{a_x^2} + \frac{y^2}{a_y^2}\right)\right]. \tag{4.2.1}$$

The calculations were performed by adding 5% intensity noise to the input beam. We note that the numerical simulations allowed only qualitative comparison between the numerical and experimental data: the period of the simulated MF array and the diameter of the individual filaments were smaller by a factor of $2 \div 4$, as compared to the experimentally measured values. This issue will be discussed in more detail the next section. Nevertheless, the numerical simulations enabled capturing the propagation dynamics (versus z) and corresponding spatiotemporal evolution of the MF array in detail, as well as calculation of the spatiotemporal spectra, whose intensity range extends over more than 6 orders of magnitude and therefore not possible to measure experimentally.

And finally, we have simulated the intensity cross-correlation function of the output (test) pulses with 30-fs probe pulses via sum-frequency generation process, as it was performed in the experiment. Therefore we have calculated the intensity cross-correlation function between the test pulse at the output of the fused silica sample $I_t(t, x, y, z = L)$, where L is the sample length, and 30-fs Gaussian probe pulse:

$$I_{cc}(t,x,y) = \int I_t(t,x,y) I_p(t-\tau,x,y) d\tau = \frac{1}{2\pi} \int S_t(\Omega,x,y) \exp\left(-\frac{\Omega^2 \tau_p^2}{16 \ln 2}\right) \exp(-i\Omega t) d\Omega, \quad (4.2.2)$$

where $I_{cc}(t,x,y)$ is the cross-correlation intensity (intensity of the sum-frequency signal), $S_t(\Omega,x,y)$, is the power spectrum of the test pulse, τ_p is the probe pulse duration, and τ is the time delay.

4.2.3 Results and discussion

In the experiment, formation of the MF arrays was investigated in two particular cases: using moderate ($a_y/a_x = 3.5$) and high ($a_y/a_x = 6.8$) input-beam ellipticity. In the first case, the dimensions of the input beam at the input face of the fused silica sample were set as $a_x = 80\,\mu$m and $a_y = 280\,\mu$m ($a_y/a_x = 3.5$). The self-focusing dynamics of the elliptical light beams is well known from previous studies: an intense elliptical input-beam undergoes self-focusing in its shorter dimension (a_x) and eventually breaks-up into multiple filaments, arranged in a (quasi)periodic MF pattern along the longer dimension of the beam [224, 231]. With present experimental settings, a distinct MF array starts to emerge at the output of 20-mm fused silica sample with the input-beam energy of $E_{in} > 10\,\mu$J.

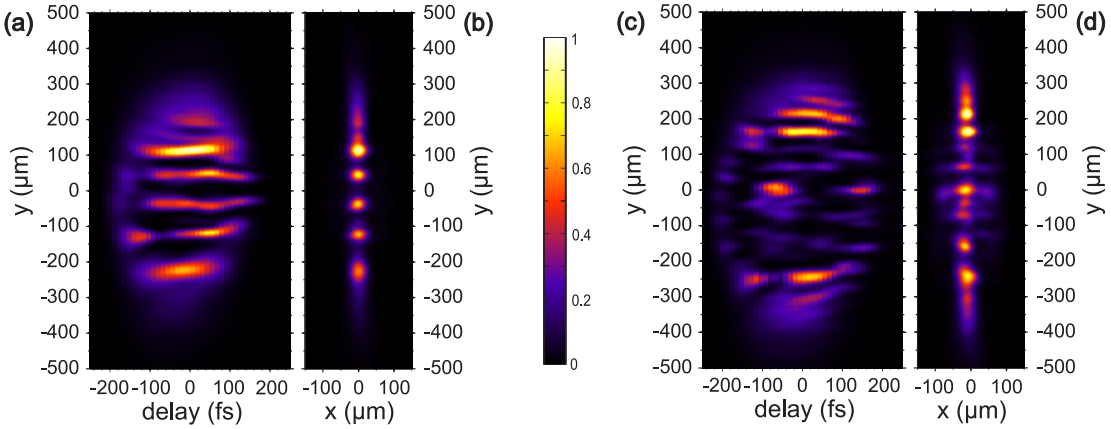

Figure 4.2.2: Central cross-section in the y-t plane of the experimentally measured spatiotemporal intensity distribution in the MF array, excited by (a) $12\,\mu$J and (c) $14\,\mu$J energy pulses with moderate input-beam ellipticity. Panels (b) and (d) show the corresponding time-integrated images.

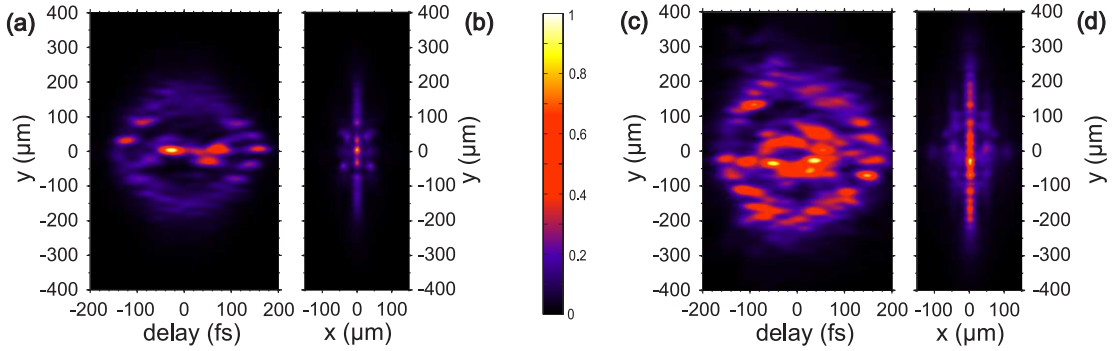

Figure 4.2.3: Numerically simulated intensity cross-correlation between the MF array and 30-fs probe pulse at different input-beam intensity: (a) $I_{in} = 200\,\mathrm{GW/cm^2}$, (c) $I_{in} = 250\,\mathrm{GW/cm^2}$. Panels (b) and (d) show the corresponding time-integrated images.

Figure 4.2.3 summarizes the experimental results obtained with the input-beams of moderate ellipticity. The central cross-section in the y-t plane of the spatiotemporal intensity profile of the MF array excited by $E_{in} = 12\,\mu\mathrm{J}$ pulses is illustrated in Fig. 4.2.3(a). Although the temporal reshaping of the pulses comprising the individual filaments is barely visible, the striking feature of the MF array is that the individual filaments propagate in curved trajectories. It is also interesting that the time integration of the full spatiotemporal intensity profile yields a periodic MF pattern, as illustrated in Fig. 4.2.3(b), which is familiar to that captured directly with the time-integrating CCD camera [231].

With slightly higher input energy ($E_{in} = 14\,\mu\mathrm{J}$), the number of the individual filaments increases, the pulse break-up regime sets in, and the measured spatiotemporal intensity profile increases in complexity, as illustrated in Fig. 4.2.3(c). In this case, short temporal peaks emerge in the leading front (whose origin and features will be discussed later), while the remaining spatiotemporal intensity distribution acquires a complex shape and shows a superficial resemblance with the propagation of intense femtosecond pulses in air, in the so called optically turbulent regime [232], which recently has also been revealed from numerical simulations of the propagation of infrared and ultraviolet pulsed beams in fused silica [103]. The curvature of the individual filament trajectories becomes apparently three-dimensional, the time-integrated MF pattern becomes deteriorated; note how the centers of the individual filaments deviate from a straight central $x = 0$ line, as shown in Fig. 4.2.3(d).

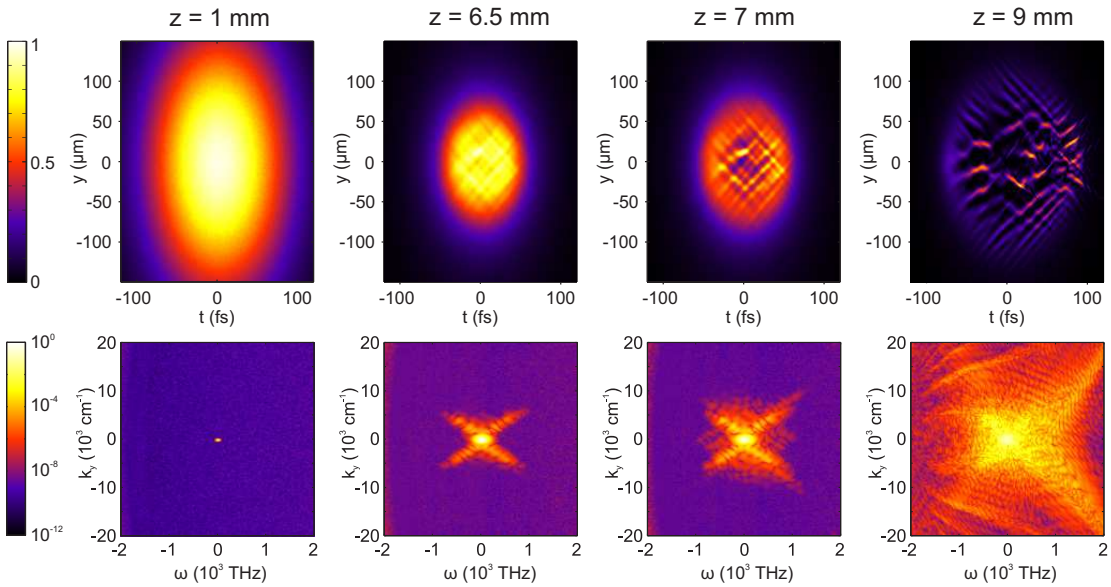

Figure 4.2.4: Numerically simulated evolution of (top panel) spatiotemporal intensity distribution in the y-t plane and (bottom panel) corresponding spatiotemporal spectrum of the self-focusing elliptical beam of moderate input-beam ellipticity at $I_{in} = 250\,\mathrm{GW/cm^2}$.

The results of numerical simulation are presented in Fig. 4.2.3 and qualitatively reproduce the essential features observed experimentally: the curvature of the individual filament trajectories, occurrence of the short temporal peaks, and showing how the complexity of the spatiotemporal picture increases with increasing the input-beam energy. Also note, how these apparently irregular structures "merge" into quasi-regular MF patterns in the time-integrated representation. However, we note the marked differences in the period of the MF array and the diameter of the individual filaments, as obtained by the numerical simulations and measured experimentally. For instance, by comparing the results depicted in Fig. 4.2.3(b) and Fig. 4.2.3(b), the experimental data suggests the MF period of 85 μm and FWHM diameter of the individual filament of 30 μm, whereas these values obtained from the numerical simulation are 30 μm and 5 μm, respectively. Indeed, in the earlier study [165], it was found that the filament diameter is intimately related to the nonlinear losses, which reflect the contribution of the multiphoton absorption and electron plasma. However, there remains an unresolved problem of matching of these two quantities, as obtained from the simulation and from the experiment, because of the uncertainties in knowledge of the relevant plasma parameters and because of the limitations of the theoretical model itself. As a result, the differ-

ences in the filament diameter by a factor of 2 were obtained in the case of three and four photon absorption [165]. In the present case, we deal with the nonlinear losses associated with 6-photon absorption, therefore it is not surprising that the differences in relevant parameters characterizing the MF array are even larger.

Despite the aforementioned differences, the results of numerical simulation provide useful insights into formation dynamics of the MF array. Specifically, the origin of the curved filament trajectories may be interpreted in terms of so-called hidden (or skewed) coherence between waves arising from nonlinear interactions [233]. These space-time trajectories rely on the phase-matching conditions and are featured by emergence of the X-shaped spatiotemporal spectrum, as recently demonstrated in the case of the three-wave parametric interactions [234, 235]. In our case, the governing process is the four-wave interaction. Indeed, the four-wave parametric interaction mediates the beam break-up [231] and generates the fields that are self-correlated along specific spatiotemporal trajectories as well. A closer look at the early spatiotemporal dynamics is presented in Fig. 4.2.3, where we plot the magnified portion of the numerically simulated spatiotemporal intensity distribution and its spatiotemporal spectrum as a function of the propagation distance z. Note, how the intensity modulation at the beam center manifests itself along specific lines, that are skewed with respect to y and t axes at $z = 6.5$ mm, and how these lines intensify and form a distinct "net-shaped" intensity modulation at $z = 7\,\text{mm}$. At the same time, the corresponding spatiotemporal spectra develop a clearly distinguishable X-shaped profiles, whose arms are directed along the phase-matching lines. The increased intensity modulation (at $z = 9\,\text{mm}$) provides centers of attraction, that precede formation of light filaments. On the other hand, the X-shaped spatiotemporal spectra are unambiguously linked to the X-wave formation in the filamentation regime [84], and therefore sets the link between formation of the MF array and X-wave generation.

In the second experiment, the dimensions of the input beam were set as $a_x = 90\,\mu\text{m}$ and $a_y = 610\,\mu\text{m}$, producing high ($a_y/a_x = 6.8$) input-beam ellipticity. The threshold for emergence of the MF array in this case was found at $E_{in} = 48\,\mu\text{J}$. Figure 4.2.3(a) plots the measured spatiotemporal intensity distribution of the MF array excited with $E_{in} = 58\,\mu\text{J}$ input pulses. It worth mentioning that in this case the experimental and numerical MF

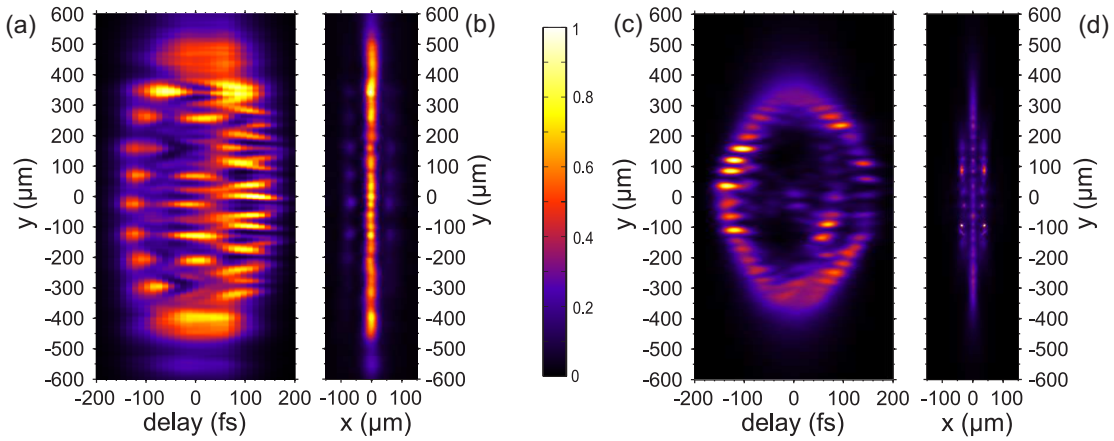

Figure 4.2.5: (a) Central cross-section in the y-t plane of the experimentally measured spatiotemporal intensity distribution and (b) time-integrated image of the MF array, excited by 58 μJ energy pulses with high input-beam ellipticity; (c), (d) show the corresponding cross-correlation data obtained by the numerical simulation with $I_{in} = 180\,\mathrm{GW/cm^2}$.

periods and filament diameters differ by a factor of 2. The emerging spatiotemporal picture exhibits much more regularity as compared with the picture discussed above. Specifically, the individual filaments experience well-distinguished temporal and spatial reshaping, trajectories of the individual filaments are no longer curved, although skewed spatiotemporal substructures are still present at the beam periphery. Three distinct arrays of sub-pulses may be identified: very short superluminally (with respect to the group velocity of the input pulse) propagating localized peaks in the leading front, which are followed by longer sub-pulses centered on the input-pulse top, and trailed by subluminally propagating sub-pulses at the back front, which form fork-shaped spatiotemporal structures; see also the isointensity plot in Fig. 4.2.6, which is provided for illustrative reasons and clearly outlines the basic features. The experimental observations are qualitatively reproduced by the numerical simulations, illustrated in Figs. 4.2.3 (c) and (d).

By comparing Figs. 4.2.3 and 4.2.6 and taking into account the findings in early propagation dynamics, the emerging spatiotemporal dynamics within the MF array could be interpreted in terms of the interplay between the X-wave formation and development of shock-fronts, which are considered to play the key role in the single filament dynamics [25, 86]. At the leading front, very short, equally spaced (in the direction perpendicular to the propagation direction) localized peaks (the leading shock-fronts) line-up into a

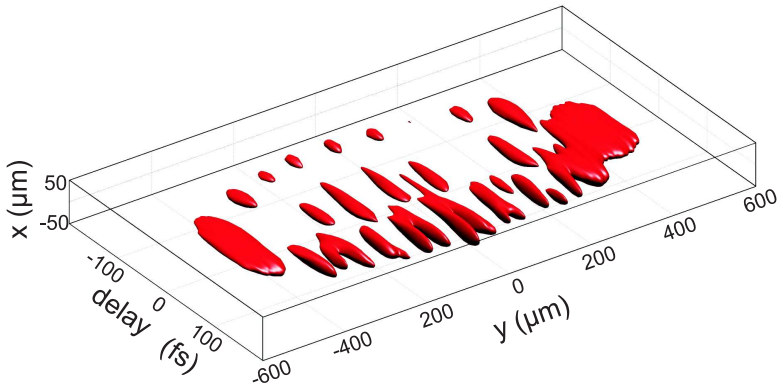

Figure 4.2.6: Spatiotemporal isointensity surface at 45% maximum intensity level of the MF array depicted in Fig. 4.2.3(a) and (b).

distinct temporal head of the MF array. The FWHM duration of each of the peaks was estimated from the cross-correlation data and was found to be close to 30 fs, that corresponds to the length of the probe pulse itself. This indicates that the actual temporal width of the leading shock-fronts is much shorter. Indeed, their duration, as estimated from the numerical simulation, is close to 5 fs. These extremely short shock-fronts advance the input pulse (whose top is centered at $t = 0$), and that is a clear signature of their superluminal propagation. Indeed, the superluminal propagation of the leading shock-fronts was recently captured in the single filament propagation regime in dense media with normal group velocity dispersion by time-gated angular spectrum characterization [86], time-resolved optical polarigraphy [236] and shadowgraphy [46]. The leading shock-fronts experience strong self-compression and comprise an apparent bow-shaped front of the MF array: note, how the shortest and the most advanced peaks reside in the center of the beam, where the input-beam intensity is the highest and where the beam break-up and pulse splitting events occur first. Also note, how the pulse splitting is absent in the very periphery of the beam, where the input-beam intensity is the lowest.

The occurrence of distinct central sub-pulses at $t = 0$ (at the top of the input-pulse), which are only marginally present in the numerical simulation, might be attributed to permanent structural change of fused silica under intense pulse irradiation. Indeed, intense long-term irradiation at 1 kHz repetition rate induces permanent guiding channels with slightly higher refractive index due to material densification [237]. These channels trap and guide the radiation from the closest vicinity. To our opinion, the guiding

effect also contributes to the "straightening" of the propagation trajectories of the individual filaments. Note also that skewed spatiotemporal structures still persist away from the beam center, as seen in Figs. 4.2.3(a) and (c).

At the back front, an array of subluminally propagating (and therefore delayed with respect to the input pulse top) shock-fronts are formed as well, however, with substantial differences as compared to the single filament dynamics. The complex trailing spatiotemporal structure is likely produced by a collective interplay between extended conical tails of the neighboring filaments, central sub-pulses and trailing shock-fronts and by electron plasma contribution. It is worth mentioning that this structure is two dimensional and is located only at the center of the y-t plane, as evident from the isointensity plot in Fig. 4.2.6. Note also, how these complex trailing formations blur the time-integrated MF pattern, as seen from Figs. 4.2.3(b) and (d). Yet, exact physical mechanisms responsible for the formation of complex trailing spatiotemporal part in the MF array are still pending to be disclosed.

4.2.4 Conclusions

In conclusion, experimental and numerical investigation of the spatiotemporal behavior of the MF arrays excited by intense elliptical laser beams in fused silica revealed a number of interesting features. Although intense elliptical input-beams carrying femtosecond light pulses break-up into regular and quasi-periodic MF patterns in the space domain, the spatiotemporal behavior of the individual filaments exhibits surprising features, which depend on the input-beam ellipticity and power. In the case of moderate input-beam ellipticity, the individual filaments propagate in curved trajectories and form complex spatiotemporal structures, which resemble optically turbulent propagation. These features originate from skewed (spatiotemporal) coherence arising in phase-matched four-wave interactions within self-focusing elliptical light beam. Conversely, the input-beams with high ellipticity break-up into (quasi)regular spatiotemporal patterns, featuring a distinct bow-shaped temporal head of the MF array, composed of extremely short peaks, which originate from the interplay between the X-wave and shock-front formation, and share many common with the single filament dynamics. In particular, extremely short ($\sim 5\,\mathrm{fs}$) and localized (FWHM width of $20\,\mu\mathrm{m}$) shock-fronts at the leading edge propagate at superlumi-

nal velocity with respect to the group velocity of the input pulse. Each individual filament in the MF array is almost a replica of its neighbor, just with different temporal position of the leading shock-front, indicating when, earlier or later, the pulse splitting event occurs as a function of the local input-beam intensity. The trailing spatiotemporal part of the MF array reveals a number of specific features, that are likely promoted by collective interactions among weak and extended conical tails of the neighboring filaments, central sub-pulses, trailing shock-fronts and by electron plasma contribution.

And finally, our findings might be of use by providing useful hints for better understanding and optimization of light and matter interactions, concerning energy localization and deposition processes in dense dispersive media in particular; the knowledge that is on demand for many practical applications.

Main results and conclusions

1. The complete evolution cycle of ultraviolet filaments in water is captured in detail disclosing intimate relationship between the relevant physical processes: focusing and defocusing of the beam, pulse splitting and replenishment, supercontinuum generation, conical emission and occurrence of nonlinear absorption peaks. It is demonstrated that every focusing cycle ends up with a peak of the nonlinear losses at the nonlinear focus, followed by the pulse splitting, supercontinuum generation and conical emission. Defocusing forms a ring structure at the center of the pulse, which replenishes the central peak. Thereafter the central peak undergoes a successive self-focusing cycle, which leads to secondary splitting of the pulse, producing modulations in the supercontinuum spectra and in conical emission pattern, as due to interference between the primary and secondary sub-pulses.

2. By combined high dynamic range measurements of spatiotemporal intensity profiles, angularly resolved spectra and energy flux, the physical nature of spatiotemporal light bullets which emerge from self-focusing of mid-infrared laser pulses in bulk dielectric medium with anomalous group velocity dispersion is disclosed. It is demonstrated that the light bullet consists of a sharply localized high-intensity core which carries the self-compressed pulse and an extended, ring-shaped spatiotemporal periphery. Strong space-time coupling within the light bullet results in very specific flow of the energy that finds an explanation in terms of a polychromatic Bessel beam with subluminally propagating envelope peak. As a consequence of this, the light bullets exhibit temporal dispersion and strongly suppressed diffraction as they exit the nonlinear medium and propagate in free space.

3. It is demonstrated experimentally and numerically that large shot-to-shot fluctuations of the spectral intensity of the blue-shifted supercontinuum components, that occur in the transient stage of the

supercontinuum generation obey extreme-value (heavy-tailed) statistics. These large fluctuations arise from small fluctuations of the input pulse intensity and are related to the pulse splitting and build-up of intense trailing sub-pulse. These fluctuations are found to be coupled in space and time and therefore linked to formation of a three-dimensional rogue X wave with largely extended conical tail at the trailing edge of the pulse. The intensity clamping was found to be a mechanism which efficiently suppresses the occurrence of the extreme events.

4. A comparative experimental study of the supercontinuum generation in sapphire with femtosecond 800 nm, 130 fs pulses revealed that dynamics of the spectral broadening induced by low numerical aperture-focused Gaussian beam and axicon-generated Bessel beam are very similar, leading to generation of ultrastable (with RMS fluctuation less than 1%), broadband and smooth supercontinuum spectra. It is demonstrated that the occurrence of peculiar stability and instability regions in the supercontinuum spectra is associated with cascaded four-wave mixing-induced spectral broadening, which is responsible for distinct correlations of the intensity fluctuations at certain wavelengths.

5. Detailed experimental investigation of the supercontinuum generation in sapphire with 120 fs, 800 nm laser pulses is carried out under variable focusing conditions and demonstrates that loose focusing results in strongly enhanced red-shifted spectral broadening (up to 1.6 μm). The numerical simulations reproduced the experimental results in great detail, confirming the time-domain scenario of the supercontinuum generation, which is based on pulse splitting in normally dispersive nonlinear medium. It is shown that the red- and blue-shifted broadenings of the spectrum are related to intensity dynamics and pulse-front evolution of the leading and trailing sub-pulses, respectively. In particular, it is demonstrated that enhanced red-shifted spectral broadening is achieved in loose focusing condition as a result of increased nonlinear propagation of the leading sub-pulse, which preserves a steep ascending front.

6. Formation of reproducible periodic one- and two-dimensional filament arrays is demonstrated by self-focusing of highly elliptical laser beams

in fused silica. Multiple filaments form highly reproducible periodic patterns, emerging from four-wave mixing between wave vectors, which fulfill the phase-matching condition. The spacing between the individual filaments is intensity dependent and is explained as due to modification of the phase-matching condition by self-phase and cross-phase modulation via nonlinear refractive index. Spatiotemporal characterization of multiple filament arrays discloses that the individual filaments propagate in curved trajectories, which resemble optically turbulent propagation, originating from skewed (spatiotemporal) coherence, which arises from phase-matched four-wave interactions.

Acknowledgments

Author considers himself lucky to work in a team lead by prof. A. Dubietis - numerous publications and international collaboration would have not happened without his leadership. All the experiments described in this thesis were performed in Vilnius University, Department of Quantum Electronics during the period 2008-2014 by the author himself and without any exception - under supervision of dr. G. Tamošauskas. Dr. V. Jukna was supporting experiments with numerical simulations which were vital to disclose the nature of the phenomena in investigation. I'd like to express my deepest gratitude to my closest colleagues. Thank you.

Part of the works presented was funded by Grant No. VP1-3.1-SMM-07-K-03-001 from the Lithuanian Science Council.

Bibliography

[1] A. Braun, G. Korn, X. Liu, D. Du, J. Squier, and G. Mourou, Self-channeling of high-peak-power femtosecond laser pulses in air, Opt. Lett., **20**(1), 73–75 (1995).

[2] S. L. Chin, S. A. Hosseini, W. Liu, Q. Luo, F. Théberge, N. Aközbek, A. Becker, V. P. Kandidov, O. G. Kosareva, and H. Schroeder, The propagation of powerful femtosecond laser pulses in opticalmedia: physics, applications, and new challenges, Can. J. Phys., **83**(9), 863–905 (2005).

[3] A. Couairon and A. Mysyrowicz, Femtosecond filamentation in transparent media, Phys. Rep., **441**(2-4), 47–189 (2007).

[4] L. Bergé, S. Skupin, R. Nuter, J. Kasparian, and J.-P. Wolf, Ultrashort filaments of light in weakly ionized, optically transparent media, Rep. Prog. Phys., **70**(10), 1633 (2007).

[5] V. P. Kandidov, S. A. Shlenov, and O. G. Kosareva, Filamentation of high-power femtosecond laser radiation, Quant. Electron., **39**(3), 205 (2009).

[6] J. H. Marburger, Self-focusing: Theory, Prog. Quant. Electron, **4, Part 1**(0), 35 – 110 (1975).

[7] A. Brodeur and S. L. Chin, Ultrafast white-light continuum generation and self-focusing in transparent condensed media, J. Opt. Soc. Am. B, **16**(4), 637–650 (1999).

[8] F. Silva, D. R. Austin, A. Thai, M. Baudisch, M. Hemmer, D. Faccio, A. Couairon, and J. Biegert, Multi-octave supercontinuum generation from mid-infrared filamentation in a bulk crystal, Nature Commun., **3**, 807 (2012).

[9] J. Darginavičius, D. Majus, V. Jukna, N. Garejev, G. Valiulis, A. Couairon, and A. Dubietis, Ultrabroadband supercontinuum and third-harmonic generation in bulk solids with two optical-cycle carrier-envelope phase-stable pulses at 2 μm, Opt. Express, **21**(21), 25210–25220 (2013).

[10] M. A. Porras, A. Dubietis, E. Kucinskas, F. Bragheri, V. Degiorgio, A. Couairon, D. Faccio, and P. Di Trapani, From X- to O-shaped spatiotemporal spectra of light filaments in water, Opt. Lett., **30**(24), 3398–3400 (2005).

[11] D. Faccio, A. Couairon, and P. Di Trapani, Conical waves, filaments and nonlinear filamentation optics, Aracne (2007).

[12] A. L. Gaeta, Catastrophic collapse of ultrashort pulses, Phys. Rev. Lett., **84**, 3582–3585 (2000).

[13] A. Couairon, J. Biegert, C. P. Hauri, W. Kornelis, F. W. Helbing, U. Keller, and A. Mysyrowicz, Self-compression of ultra-short laser pulses down to one optical cycle by filamentation, J. Mod. Opt., **53**(1-2), 75–85 (2006).

[14] M. Durand, A. Jarnac, A. Houard, Y. Liu, S. Grabielle, N. Forget, A. Durécu, A. Couairon, and A. Mysyrowicz, Self-guided propagation of ultrashort laser pulses in the anomalous dispersion region of transparent solids: A new regime of filamentation, Phys. Rev. Lett., **110**, 115003 (2013).

[15] J. Kasparian, R. Sauerbrey, and S.L. Chin, The critical laser intensity of self-guided light filaments in air, Appl. Phys. B, **71**(6), 877–879 (2000).

[16] W. Liu, S. Petit, A. Becker, N. Aközbek, C.M. Bowden, and S.L. Chin, Intensity clamping of a femtosecond laser pulse in condensed matter, Opt. Commun., **202**(1-3), 189 – 197 (2002).

[17] A. Dubietis, E. Gaižauskas, G. Tamošauskas, and P. Di Trapani, Light filaments without self-channeling, Phys. Rev. Lett., **92**, 253903 (2004).

[18] A. Dubietis, E. Kucinskas, G. Tamosauskas, E. Gaizauskas, M. A. Porras, and P. Di Trapani, Self-reconstruction of light filaments, Opt. Lett., **29**(24), 2893–2895 (2004).

[19] F. Courvoisier, V. Boutou, J. Kasparian, E. Salmon, G. Méjean, J. Yu, and J.-P. Wolf, Ultraintense light filaments transmitted through clouds, Appl. Phys. Lett., **83**(2), 213–215 (2003).

[20] M. Kolesik and J. V. Moloney, Self-healing femtosecond light filaments, Opt. Lett., **29**(6), 590–592 (2004).

[21] V. Jukna, G. Tamošauskas, G. Valiulis, M. Aputis, M. Puida, F. Ivanauskas, and A. Dubietis, Filamentation of ultrashort light pulses in a liquid scattering medium, Appl. Phys. B, **94**(1), 175–179 (2009).

[22] C. Conti, S. Trillo, P. Di Trapani, G. Valiulis, A. Piskarskas, O. Jedrkiewicz, and J. Trull, Nonlinear electromagnetic X waves, Phys. Rev. Lett., **90**, 170406 (2003).

[23] W. Liu, J.-F. Gravel, F. Théberge, A. Becker, and S.L. Chin, Background reservoir: its crucial role for long-distance propagation of femtosecond laser pulses in air, Appl. Phys. B, **80**(7), 857–860 (2005).

[24] M. Kolesik, E. M. Wright, and J. V. Moloney, Dynamic nonlinear X waves for femtosecond pulse propagation in water, Phys. Rev. Lett., **92**, 253901 (2004).

[25] D. Faccio, M. A. Porras, A. Dubietis, F. Bragheri, A. Couairon, and P. Di Trapani, Conical emission, pulse splitting, and X-wave parametric amplification in nonlinear dynamics of ultrashort light pulses, Phys. Rev. Lett., **96**, 193901 (2006).

[26] D. Faccio, M. Clerici, A. Averchi, A. Lotti, O. Jedrkiewicz, A. Dubietis, G. Tamosauskas, A. Couairon, F. Bragheri, D. Papazoglou, S. Tzortzakis, and P. Di Trapani, Few-cycle laser-pulse collapse in Kerr media: The role of group-velocity dispersion and X-wave formation, Phys. Rev. A, **78**, 033826 (2008).

[27] D. Faccio, A. Averchi, A. Lotti, P. Di Trapani, A. Couairon, D. Papazoglou, and S. Tzortzakis, Ultrashort laser pulse filamentation fromspontaneous X-wave formation in air, Opt. Express, **16**(3), 1565–1570 (2008).

[28] J. Kasparian, M. Rodriguez, G. Méjean, J. Yu, E. Salmon, H. Wille, R. Bourayou, S. Frey, Y.-B. André, A. Mysyrowicz, R. Sauerbrey, J.-P. Wolf, and L. Wöste, White-light filaments for atmospheric analysis, Science, **301**(5629), 61–64 (2003).

[29] J. Kasparian and J.-P. Wolf, Physics and applications of atmospheric nonlinear optics and filamentation, Opt. Express, **16**(1), 466–493 (2008).

[30] K. Yamada, W. Watanabe, T. Toma, K. Itoh, and J. Nishii, In situ observation of photoinduced refractive-index changes in filaments formed in glasses by femtosecond laser pulses, Opt. Lett., **26**(1), 19–21 (2001).

[31] D. Kiselev, L. Woeste, and J.-P. Wolf, Filament-induced laser machining (film), Appl. Phys. B, **100**(3), 515–520 (2010).

[32] M. Hemmer, M. Baudisch, A. Thai, A. Couairon, and J. Biegert, Self-compression to sub-3-cycle duration of mid-infrared optical pulses in dielectrics, Opt. Express, **21**(23), 28095–28102 (2013).

[33] D. Faccio, S. Cacciatori, V. Gorini, V. G. Sala, A. Averchi, A. Lotti, M. Kolesik, and J. V. Moloney, Analogue gravity and ultrashort laser pulse filamentation, Europhys. Lett., **89**(3), 34004 (2010).

[34] F. Belgiorno, S. L. Cacciatori, M. Clerici, V. Gorini, G. Ortenzi, L. Rizzi, E. Rubino, V. G. Sala, and D. Faccio, Hawking radiation from ultrashort laser pulse filaments, Phys. Rev. Lett., **105**, 203901 (2010).

[35] A. Couairon, E. Brambilla, T. Corti, D. Majus, O. Ramírez-Góngora, and M. Kolesik, Practitioner‘s guide to laser pulse propagation models and simulation, Eur. Phys. J. Spec. Top., **199**(1), 5–76 (2011).

[36] D. Majus, V. Jukna, G. Tamošauskas, G. Valiulis, and A. Dubietis, Three-dimensional mapping of multiple filament arrays, Phys. Rev. A, **81**, 043811 (2010).

[37] Q. Sun, H. Jiang, Y. Liu, Z. Wu, H. Yang, and Q. Gong, Measurement of the collision time of dense electronic plasma inducedby a femtosecond laser in fused silica, Opt. Lett., **30**(3), 320–322 (2005).

[38] R. M. Pope and E. S. Fry, Absorption spectrum (380–700 nm) of pure water. II. integrating cavity measurements, Appl. Opt., **36**(33), 8710–8723 (1997).

[39] L. Kou, D. Labrie, and P. Chylek, Refractive indices of water and ice in the 0.65- to 2.5-µm spectral range, Appl. Opt., **32**(19), 3531–3540 (1993).

[40] G. G. Luther, E. M. Wright, J. V. Moloney, and A. C. Newell, Self-focusing threshold in normally dispersive media, Opt. Lett., **19**(12), 862–864 (1994).

[41] M. M. T. Loy and Y. R. Shen, Small-scale filaments in liquids and tracks of moving foci, Phys. Rev. Lett., **22**, 994–997 (1969).

[42] V. No. Lugovoi and A. M. Prokhorov, Possible explanation of small-scale filaments of selffocusing, JETP Lett, **7**, 117–119 (1968).

[43] V. N. Lugovoi and A. M. Prokhorov, Theory of the propagation of high-power laser radiation in a nonlinear medium, Physics-Uspekhi, **16**(5), 658–679 (1974).

[44] Y. R. Shen, Principles of Nonlinear Optics, Wiley, New York (1984).

[45] S. Minardi, A. Gopal, M. Tatarakis, A. Couairon, G. Tamošauskas, R. Piskarskas, A. Dubietis, and P. Di Trapani, Time-resolved refractive index and absorption mapping of light-plasma filaments in water, Opt. Lett., **33**(1), 86–88 (2008).

[46] S. Minardi, A. Gopal, A. Couairon, G. Tamošauskasuskas, R. Piskarskas, A. Dubietis, and P. Di Trapani, Accurate retrieval of pulse-splitting dynamics of a femtosecond filament in water by time-resolved shadowgraphy, Opt. Lett., **34**(19), 3020–3022 (2009).

[47] P. Whalen, J. V. Moloney, and M. Kolesik, Self-focusing collapse distance in ultrashort pulses and measurement of nonlinear index, Opt. Lett., **36**(13), 2542–2544 (2011).

[48] A. Brodeur, C. Y. Chien, F. A. Ilkov, S. L. Chin, O. G. Kosareva, and V. P. Kandidov, Moving focus in the propagation of ultrashort laser pulses in air, Opt. Lett., **22**(5), 304–306 (1997).

[49] A. Couairon, Light bullets from femtosecond filamentation, Eur. Phys. J. D, **27**, 159–167 (2003).

[50] M. A. C. Potenza, S. Minardi, J. Trull, G. Blasi, D. Salerno, A. Varanavičius, A. Piskarskas, and P. Di Trapani, Three dimensional imaging of short pulses, Opt. Commun., **229**(1-6), 381 – 390 (2004).

[51] A. Matijošius, J. Trull, P. Di Trapani, A. Dubietis, R. Piskarskas, A. Varanavičius, and A. Piskarskas, Nonlinear space-time dynamics ofultrashort wave packets in water, Opt. Lett., **29**(10), 1123–1125 (2004).

[52] F. Wise and P. Di Trapani, Spatiotemporal solitons, Opt. Photon. News, **13**(2), 28–32 (2002).

[53] B. A. Malomed, D. Mihalache, F. Wise, and L. Torner, Spatiotemporal optical solitons, J. Opt. B, **7**(5), R53 (2005).

[54] D. Mihalache, Linear and nonlinear light bullets: recent theoretical and experimental studies, Rom. J. Phys, **57**, 352–371 (2012).

[55] H. Leblond and D. Mihalache, Models of few optical cycle solitons beyond the slowly varying envelope approximation, Phys. Rep., **523**(2), 61 – 126 (2013).

[56] J. S. D'Souza, J. A. Dharmadhikari, A. K. Dharmadhikari, B. J. Rao, and D. Mathur, Effect of intense, ultrashort laser pulses on dna plasmids in their native state: Strand breakages induced by in situ electrons and radicals, Phys. Rev. Lett., **106**, 118101 (2011).

[57] A. Vogel, N. Linz, S. Freidank, and G. Paltauf, Femtosecond-laser-induced nanocavitation in water: Implications for optical breakdown threshold and cell surgery, Phys. Rev. Lett., **100**, 038102 (2008).

[58] A. Vogel, J. Noack, G. Hüttman, and G. Paltauf, Mechanisms of femtosecond laser nanosurgery of cells and tissues, Appl. Phys. B, **81**(8), 1015–1047 (2005).

[59] R. Meesat, H. Belmouaddine, J.-F. Allard, C. Tanguay-Renaud, R. Lemay, T. Brastaviceanu, L. Tremblay, B. Paquette, J. R. Wagner, J.-P. Jay-Gerin, M. Lepage, M. A. Huels, and D. Houde, Cancer radiotherapy based on femtosecond IR laser-beam filamentation yielding ultra-high dose rates and zero entrance dose, Proc. Natl. Acad. Sci. U.S.A., **109**(38), E2508–E2513 (2012).

[60] K. Plamann, F. Aptel, C. L. Arnold, A. Courjaud, C. Crotti, F. Deloison, F. Druon, P. Georges, M. Hanna, J.-M. Legeais, F. Morin, É. Mottay, V. Nuzzo, D. A. Peyrot, and M. Savoldelli, Ultrashort pulse laser surgery of the cornea and the sclera, J. Opt., **12**(8), 084002 (2010).

[61] M. Vengris, E. Gabryte, A. Aleknavicius, M. Barkauskas, O. Ruksenas, A. Vaiceliunaite, and R. Danielius, Corneal shaping and ablation of transparent media by femtosecond pulses in deep ultraviolet range, J. Cataract Refract. Surg., **36**(9), 1579 – 1587 (2010).

[62] M. Merker, R. Ackermann, R. Kammel, K. S. Kunert, and S. Nolte, An in vitro study on focusing fs-laser pulses into ocular media for ophthalmic surgery, Lasers Surg. Med., **45**(9), 589–596 (2013).

[63] J. Noack and A. Vogel, Laser-induced plasma formation in water at nanosecond to femtosecond time scales: calculation of thresholds, absorption coefficients, and energy density, IEEE J. Quant. Electron., **35**(8), 1156–1167 (1999).

[64] Q. Feng, E. M. Wright, J. V. Moloney, and A. C. Newell, Laser-induced breakdown versus self-focusing for focused picosecond pulses in water, Opt. Lett., **20**(19), 1958–1960 (1995).

[65] C. Schaffer, N. Nishimura, E. Glezer, A. Kim, and E. Mazur, Dynamics of femtosecond laser-induced breakdown in water from femtoseconds to microseconds, Opt. Express, **10**(3), 196–203 (2002).

[66] D. Faccio, E. Rubino, A. Lotti, A. Couairon, A. Dubietis, G. Tamošauskas, D. G. Papazoglou, and S. Tzortzakis, Nonlinear light-matter interaction with femtosecond high-angle Bessel beams, Phys. Rev. A, **85**, 033829 (2012).

[67] A.C. Bernstein, T.S. Luk, T.R. Nelson, A. McPherson, J.-C. Diels, and S.M. Cameron, Asymmetric ultra-short pulse splitting measured in air using frog, Appl. Phys. B, **75**(1), 119–122 (2002).

[68] A. C. Bernstein, J.-C. Diels, T. S. Luk, T. R. Nelson, A. McPherson, and S. M. Cameron, Time-resolved measurements of self-focusing pulses in air, Opt. Lett., **28**(23), 2354–2356 (2003).

[69] M. Wittmann and A. Penzkofer, Spectral superbroadening of femtosecond laser pulses, Opt. Commun., **126**(4-6), 308 – 317 (1996).

[70] A. Brodeur and S. L. Chin, Band-gap dependence of the ultrafast white-light continuum, Phys. Rev. Lett., **80**, 4406–4409 (1998).

[71] A. Dubietis, G. Tamošauskas, I. Diomin, and A. Varanavičius, Self-guided propagation of femtosecond light pulses in water, Opt. Lett., **28**(14), 1269–1271 (2003).

[72] W. Liu, O. Kosareva, I.S. Golubtsov, A. Iwasaki, A. Becker, V.P. Kandidov, and S.L. Chin, Femtosecond laser pulse filamentation versus optical breakdown in H2O, Appl. Phys. B, **76**(3), 215–229 (2003).

[73] D. Faccio, A. Matijosius, A. Dubietis, R. Piskarskas, A. Varanavičius, E. Gaizauskas, A. Piskarskas, A. Couairon, and P. Di Trapani, Near- and far-field evolution of laser pulse filaments in Kerr media, Phys. Rev. E, **72**, 037601 (2005).

[74] M. Kolesik, G. Katona, J. V. Moloney, and E. M. Wright, Physical factors limiting the spectral extent and band gap dependence of supercontinuum generation, Phys. Rev. Lett., **91**, 043905 (2003).

[75] S. Tzortzakis, D. G. Papazoglou, and I. Zergioti, Long-range filamentary propagation of subpicosecond ultraviolet laser pulses in fused silica, Opt. Lett., **31**(6), 796–798 (2006).

[76] D. Faccio, M. Clerici, A. Averchi, O. Jedrkiewicz, S. Tzortzakis, D. Papazoglou, F. Bragheri, L. Tartara, A. Trita, S. Henin, I. Cristiani, A. Couairon, and P. Di Trapani, Kerr-induced spontaneous Bessel beam formation in the regime of strong two-photon absorption, Opt. Express, **16**(11), 8213–8218 (2008).

[77] B. Prade, M. Franco, A. Mysyrowicz, A. Couairon, H. Buersing, B. Eberle, M. Krenz, D. Seiffer, and O. Vasseur, Spatial mode cleaning by femtosecond filamentation in air, Opt. Lett., **31**(17), 2601–2603 (2006).

[78] S.L. Chin, F. Théberge, and W. Liu, Filamentation nonlinear optics, Appl. Phys. B, **86**(3), 477–483 (2007).

[79] A. Jarnac, G. Tamosauskas, D. Majus, A. Houard, A. Mysyrowicz, A. Couairon, and A. Dubietis, Whole life cycle of femtosecond ultraviolet filaments in water, Phys. Rev. A, **89**, 033809 (2014).

[80] K. D. Mielenz, Refraction correction for fluorescence spectra of aqueous solutions, Appl. Opt., **17**(18), 2875–2876 (1978).

[81] R. W. Boyd, Nonlinear Optics, Academic Press, San Diego, CA (2003).

[82] D. N. Nikogosyan, Properties of Optical and Laser-Related Materials: A Handbook, Wiley, Chichester, UK (1997).

[83] Z. W. Wilkes, S. Varma, Y.-H. Chen, H. M. Milchberg, T. G. Jones, and A. Ting, Direct measurements of the nonlinear index of refraction of water at 815 and 407 nm using single-shot supercontinuum spectral interferometry, Appl. Phys. Lett., **94**(21), 211102 (2009).

[84] A. Couairon, E. Gaižauskas, D. Faccio, A. Dubietis, and P. Di Trapani, Nonlinear X-wave formation by femtosecond filamentation in Kerr media, Phys. Rev. E, **73**, 016608 (2006).

[85] M. Mlejnek, E. M. Wright, and J. V. Moloney, Dynamic spatial replenishment of femtosecond pulses propagating in air, Opt. Lett., **23**(5), 382–384 (1998).

[86] F. Bragheri, D. Faccio, A. Couairon, A. Matijosius, Tamošauskas., A. Varanavičius, V. Degiorgio, A. Piskarskas, and P. Di Trapani, Conical-emission and shock-front dynamics in femtosecond laser-pulse filamentation, Phys. Rev. A, **76**, 025801 (2007).

[87] Y. Silberberg, Collapse of optical pulses, Opt. Lett., **15**(22), 1282–1284 (1990).

[88] K. D. Moll, Alexander L. Gaeta, and Gadi Fibich, Self-similar optical wave collapse: Observation of the townes profile, Phys. Rev. Lett., **90**, 203902 (2003).

[89] M. A. Porras, A. Parola, D. Faccio, A. Couairon, and P. Di Trapani, Light-filament dynamics and the spatiotemporal instability of the townes profile, Phys. Rev. A, **76**, 011803 (2007).

[90] M. Belić, N. Petrović, W.-P. Zhong, R.-H. Xie, and G. Chen, Analytical light bullet solutions to the generalized (3+1)-dimensional nonlinear schrödinger equation, Phys. Rev. Lett., **101**, 123904 (2008).

[91] I. B. Burgess, M. Peccianti, G. Assanto, and R. Morandotti, Accessible light bullets via synergetic nonlinearities, Phys. Rev. Lett., **102**, 203903 (2009).

[92] S. Chen and J. M. Dudley, Spatiotemporal nonlinear optical self-similarity in three dimensions, Phys. Rev. Lett., **102**, 233903 (2009).

[93] L. Torner and Y. V. Kartashov, Light bullets in optical tandems, Opt. Lett., **34**(7), 1129–1131 (2009).

[94] V. E. Lobanov, Y. V. Kartashov, and L. Torner, Light bullets by synthetic diffraction-dispersion matching, Phys. Rev. Lett., **105**, 033901 (2010).

[95] S. Minardi, F. Eilenberger, Y. V. Kartashov, A. Szameit, U. Röpke, J. Kobelke, K. Schuster, H. Bartelt, S. Nolte, L. Torner, F. Lederer, A. Tünnermann, and T. Pertsch, Three-dimensional light bullets in arrays of waveguides, Phys. Rev. Lett., **105**, 263901 (2010).

[96] P. Saari and K. Reivelt, Evidence of X-shaped propagation-invariant localized light waves, Phys. Rev. Lett., **79**, 4135–4138 (1997).

[97] A. Chong, W. H. Renninger, D. N. Christodoulides, and F. W. Wise, Airy-Bessel wave packets as versatile linear light bullets, Nature Photon., **4**, 103–106 (2010).

[98] D. Abdollahpour, S. Suntsov, D. G. Papazoglou, and S. Tzortzakis, Spatiotemporal Airy light bullets in the linear and nonlinear regimes, Phys. Rev. Lett., **105**, 253901 (2010).

[99] M. Bock, S. K. Das, and R. Grunwald, Ultrashort highly localized wavepackets, Opt. Express, **20**(11), 12563–12578 (2012).

[100] P. Di Trapani, G. Valiulis, A. Piskarskas, O. Jedrkiewicz, J. Trull, C. Conti, and S. Trillo, Spontaneously generated x-shaped light bullets, Phys. Rev. Lett., **91**, 093904 (2003).

[101] P. Panagiotopoulos, D. G. Papazoglou, A. Couairon, and S. Tzortzakis, Sharply autofocused ring-Airy beams transforming into non-linear intense light bullets, Nature Commun., **4**, 2622 (2013).

[102] K. D. Moll and Alexander L. Gaeta, Role of dispersion in multiple-collapse dynamics, Opt. Lett., **29**(9), 995–997 (2004).

[103] L. Bergé, S. Mauger, and S. Skupin, Multifilamentation of powerful optical pulses in silica, Phys. Rev. A, **81**, 013817 (2010).

[104] J. Liu, R. Li, and Z. Xu, Few-cycle spatiotemporal soliton wave excited by filamentation of a femtosecond laser pulse in materials with anomalous dispersion, Phys. Rev. A, **74**, 043801 (2006).

[105] S. Skupin and L. Bergé, Self-guiding of femtosecond light pulses in condensed media: Plasma generation versus chromatic dispersion, Physica D., **220**(1), 14 – 30 (2006).

[106] S. V. Chekalin, V. O Kompanets, E. O. Smetanina, and V. P. Kandidov, Light bullets and supercontinuum spectrum during femtosecond pulse filamentation under conditions of anomalous group-velocity dispersion in fused silicalicati, Quant. Electron., **43**, 326–331 (2013).

[107] E. O. Smetanina, V. O. Kompanets, A. E. Dormidonov, S. V. Chekalin, and V. P. Kandidov, Light bullets from near-IR filament in fused silica, Laser Phys. Lett., **10**(10), 105401 (2013).

[108] M. Durand, K. Lim, V. Jukna, E. McKee, M. Baudelet, A. Houard, M. Richardson, A. Mysyrowicz, and A. Couairon, Blueshifted continuum peaks from filamentation in the anomalous dispersion regime, Phys. Rev. A, **87**, 043820 (2013).

[109] M. A. Porras, A. Parola, and P. Di Trapani, Nonlinear unbalanced O waves: nonsolitary, conical light bullets in nonlinear dissipative media, J. Opt. Soc. Am. B, **22**(7), 1406–1413 (2005).

[110] M. A. Porras, A. Dubietis, A. Matijošius, R. Piskarskas, F. Bragheri, A. Averchi, and P. Di Trapani, Characterization of conical emission of light filaments in media with anomalous dispersion, J. Opt. Soc. Am. B, **24**(3), 581–584 (2007).

[111] D. Faccio, A. Lotti, A. Matijosius, F. Bragheri, V. Degiorgio, A. Couairon, and P. Di Trapani, Experimental energy-density flux characterization of ultrashort laser pulse filaments., Opt. Express, **17**(10), 8193–8200 (2009).

[112] A. Lotti, A. Couairon, D. Faccio, and P. Di Trapani, Energy-flux characterization of conical and space-time coupled wave packets, Phys. Rev. A, **81**, 023810 (2010).

[113] M. A. Porras, G. Valiulis, and P. Di Trapani, Unified description of Bessel X waves with cone dispersion and tilted pulses, Phys. Rev. E, **68**, 016613 (2003).

[114] R. R. Alfano and S. L. Shapiro, Emission in the region 4000 to 7000 a via four-photon coupling in glass, Phys. Rev. Lett., **24**, 584–587 (1970).

[115] R. R. Alfano, editor, The Supercontinuum Laser Source, Springer, NY, 2nd ed. edition (2006).

[116] J. M. Dudley, G. Genty, and S. Coen, Supercontinuum generation in photonic crystal fiber, Rev. Mod. Phys., **78**, 1135–1184 (2006).

[117] M. K. Reed, M. K. Steiner-Shepard, M. S. Armas, and D. K. Negus, Microjoule-energy ultrafast optical parametric amplifiers, J. Opt. Soc. Am. B, **12**(11), 2229–2236 (1995).

[118] G. Cerullo and S. De Silvestri, Ultrafast optical parametric amplifiers, Rev. Sci. Instrum., **74**(1), 1–18 (2003).

[119] A. Dubietis, R. Butkus, and A.P. Piskarskas, Trends in chirped pulse optical parametric amplification, IEEE J. Select. Top. Quantum Electron., **12**(2), 163–172 (2006).

[120] R. L. Fork, W. J. Tomlinson, C. V. Shank, C. Hirlimann, and R. Yen, Femtosecond white-light continuum pulses, Opt. Lett., **8**(1), 1–3 (1983).

[121] G. S. He, G. C. Xu, Y. Cui, and P. N. Prasad, Difference of spectral superbroadening behavior in Kerr-type and non-Kerr-type liquids pumped with ultrashort laser pulses, Appl. Opt., **32**(24), 4507–4512 (1993).

[122] C. Nagura, A. Suda, H. Kawano, M. Obara, and K. Midorikawa, Generation and characterization of ultrafast white-light continuum in condensed media, Appl. Opt., **41**(18), 3735–3742 (2002).

[123] X.-J. Fang and T. Kobayashi, Evolution of a super-broadened spectrum in a filament generated by an ultrashort intense laser pulse in fused silica, Appl. Phys. B, **77**(2-3), 167–170 (2003).

[124] V.P. Kandidov, O.G. Kosareva, I.S. Golubtsov, W. Liu, A. Becker, N. Akozbek, C.M. Bowden, and S.L. Chin, Self-transformation of a powerful femtosecond laser pulse into a white-light laser pulse in bulk optical media (or supercontinuum generation), Appl. Phys. B, **77**(2-3), 149–165 (2003).

[125] M. Kolesik, G. Katona, J.V. Moloney, and E.M. Wright, Theory and simulation of supercontinuum generation in transparent bulk media, Appl. Phys. B, **77**(2-3), 185–195 (2003).

[126] A. Dharmadhikari, F. Rajgara, N. C. Reddy, A. Sandhu, and D. Mathur, Highly efficient white light generation from barium fluoride, Opt. Express, **12**(4), 695–700 (2004).

[127] A.K. Dharmadhikari, F.A. Rajgara, and D. Mathur, Systematic study of highly efficient white light generation in transparent materials using intense femtosecond laser pulses, Appl. Phys. B, **80**(1), 61–66 (2005).

[128] M. Bradler, P. Baum, and E. Riedle, Femtosecond continuum generation in bulk laser host materials with sub-μJ pump pulses, Appl. Phys. B, **97**(3), 561–574 (2009).

[129] N. T. Nguyen, A. Saliminia, W. Liu, S. L. Chin, and R. Vallée, Optical breakdown versus filamentation in fused silica by use of femtosecond infrared laser pulses, Opt. Lett., **28**(17), 1591–1593 (2003).

[130] J. B. Ashcom, R. R. Gattass, C. B. Schaffer, and E. Mazur, Numerical aperture dependence of damage and supercontinuum generation from femtosecond laser pulses in bulk fused silica, J. Opt. Soc. Am. B, **23**(11), 2317–2322 (2006).

[131] J. K. Ranka, R. W. Schirmer, and A. L. Gaeta, Observation of pulse splitting in nonlinear dispersive media, Phys. Rev. Lett., **77**, 3783–3786 (1996).

[132] A. A. Zozulya, S. A. Diddams, A. G. Van Engen, and T. S. Clement, Propagation dynamics of intense femtosecond pulses: Multiple splittings, coalescence, and continuum generation, Phys. Rev. Lett., **82**, 1430–1433 (1999).

[133] D. Majus, V. Jukna, E. Pileckis, G. Valiulis, and A. Dubietis, Rogue-wave-like statistics in ultrafast white-light continuum generation in sapphire, Opt. Express, **19**(17), 16317–16323 (2011).

[134] D. Majus and A. Dubietis, Statistical properties of ultrafast supercontinuum generated by femtosecond Gaussian and Bessel beams: a comparative study, J. Opt. Soc. Am. B, **30**(4), 994–999 (2013).

[135] N. Akhmediev and E. Pelinovsky, "rogue waves - towards a unifying concept?", Eur. Phys. J. Spec. Top., **185**(1), 1–266 (2010).

[136] A.I. Dyachenko and V.E. Zakharov, Modulation instability of Stokes wave -> freak wave, JETP Lett., **81**(6), 255–259 (2005).

[137] N. Akhmediev, J.M. Soto-Crespo, and A. Ankiewicz, Extreme waves that appear from nowhere: On the nature of rogue waves, Phys. Lett. A, **373**(25), 2137 – 2145 (2009).

[138] D. R. Solli, C. Ropers, P. Koonath, and B. Jalali, Optical rogue waves, Nature, **450**, 1054–1057 (2007).

[139] M. Erkintalo, G. Genty, and J. M. Dudley, Rogue-wave-like characteristics in femtosecond supercontinuum generation, Opt. Lett., **34**(16), 2468–2470 (2009).

[140] J. M. Dudley, G. Genty, and B. J. Eggleton, Harnessing and control of optical rogue waves insupercontinuum generation, Opt. Express, **16**(6), 3644–3651 (2008).

[141] A. Mussot, A. Kudlinski, M. Kolobov, E. Louvergneaux, M. Douay, and M. Taki, Observation of extreme temporal events in CW-pumped supercontinuum, Opt. Express, **17**(19), 17010–17015 (2009).

[142] D. R. Solli, C. Ropers, and B. Jalali, Active control of rogue waves for stimulated supercontinuum generation, Phys. Rev. Lett., **101**, 233902 (2008).

[143] M. Erkintalo, G. Genty, and J. M. Dudley, Giant dispersive wave generation through soliton collision, Opt. Lett., **35**(5), 658–660 (2010).

[144] Kibler, B., Finot, C., and Dudley, J. M., Soliton and rogue wave statistics in supercontinuum generation in photonic crystal fibre with two zero dispersion wavelengths, Eur. Phys. J. Spec. Top., **173**, 289–295 (2009).

[145] A. Aalto, G. Genty, and J. Toivonen, Extreme-value statistics in supercontinuum generation by cascaded stimulated Raman scattering, Opt. Express, **18**(2), 1234–1239 (2010).

[146] K. Hammani, A. Picozzi, and C. Finot, Extreme statistics in Raman fiber amplifiers: From analytical description to experiments, Opt. Commun., **284**(10-11), 2594 – 2603 (2011).

[147] K. Dysthe, H. E. Krogstad, and P. Müller, Oceanic rogue waves, Annu. Rev. Fluid Mech., **40**, 287–310 (2008).

[148] A. N. Ganshin, V. B. Efimov, G. V. Kolmakov, L. P. Mezhov-Deglin, and P. V. E. McClintock, Observation of an inverse energy cascade in developed acoustic turbulence in superfluid helium, Phys. Rev. Lett., **101**, 065303 (2008).

[149] Yu. V. Bludov, V. V. Konotop, and N. Akhmediev, Matter rogue waves, Phys. Rev. A, **80**, 033610 (2009).

[150] M.S. Ruderman, Freak waves in laboratory and space plasmas, Eur. Phys. J. Spec. Top., **185**(1), 57–66 (2010).

[151] L. Stenflo and M. Marklund, Rogue waves in the atmosphere, J. Plasma Phys., **76**, 293–295 (2010).

[152] J. M. Dudley, C. Finot, G. Millot, J. Garnier, G. Genty, D. Agafontsev, and F. Dias, Extreme events in optics: Challenges of the manureva project, Eur. Phys. J. Spec. Top., **185**(1), 125–133 (2010).

[153] B. Jalali, D.R. Solli, K. Goda, K. Tsia, and C. Ropers, Real-time measurements, rare events and photon economics, Eur. Phys. J. Spec. Top., **185**(1), 145–157 (2010).

[154] K. Hammani, C. Finot, and G. Millot, Emergence of extreme events in fiber-based parametric processes driven by a partially incoherent pump wave, Opt. Lett., **34**(8), 1138–1140 (2009).

[155] K. Hammani, C. Finot, J. M. Dudley, and G. Millot, Optical rogue-wave-like extreme value fluctuations in fiber Raman amplifiers, Opt. Express, **16**(21), 16467–16474 (2008).

[156] K. Hammani, B. Kibler, C. Finot, and A. Picozzi, Emergence of rogue waves from optical turbulence, Phys. Lett. A, **374**(34), 3585 – 3589 (2010).

[157] J. Kasparian, P. Béjot, J.-P. Wolf, and J. M. Dudley, Optical rogue wave statistics in laser filamentation, Opt. Express, **17**(14), 12070–12075 (2009).

[158] D. Majus, V. Jukna, G. Valiulis, D. Faccio, and A. Dubietis, Spatiotemporal rogue events in femtosecond filamentation, Phys. Rev. A, **83**, 025802 (2011).

[159] A. Montina, U. Bortolozzo, S. Residori, and F. T. Arecchi, Non-Gaussian statistics and extreme waves in a nonlinear optical cavity, Phys. Rev. Lett., **103**, 173901 (2009).

[160] A. Maluckov, Lj. Hadžievski, N. Lazarides, and G. P. Tsironis, Extreme events in discrete nonlinear lattices, Phys. Rev. E, **79**, 025601 (2009).

[161] Y. V. Bludov, V. V. Konotop, and N. Akhmediev, Rogue waves as spatial energy concentrators in arrays of nonlinear waveguides, Opt. Lett., **34**(19), 3015–3017 (2009).

[162] A. Major, F. Yoshino, I. Nikolakakos, J. S. Aitchison, and P. W. E. Smith, Dispersion of the nonlinear refractive index in sapphire, Opt. Lett., **29**(6), 602–604 (2004).

[163] O. Uteza, B. Bussière, F. Canova, J.-P. Chambaret, P. Delaporte, T. Itina, and M. Sentis, Laser-induced damage threshold of sapphire in nanosecond, picosecond and femtosecond regimes, Appl. Surf. Sci., **254**(4), 799 – 803 (2007).

[164] P. Béjot, J. Kasparian, E. Salmon, R. Ackermann, and J.-P. Wolf, Spectral correlation and noise reduction in laser filaments, Appl. Phys. B, **87**(1), 1–4 (2007).

[165] A. Dubietis, A. Couairon, E. Kučinskas, G. Tamošauskas, E. Gaižauskas, D. Faccio, and P. Di Trapani, Measurement and calculation of nonlinear absorption associated with femtosecond filaments in water, Appl. Phys. B, **84**(3), 439–446 (2006).

[166] M. Daimon and A. Masumura, Measurement of the refractive index of distilled water from the near-infrared region to the ultraviolet region, Appl. Opt., **46**(18), 3811–3820 (2007).

[167] J.-Y. Lu and J.F. Greenleaf, Experimental verification of nondiffracting X waves, IEEE Trans. Ultrason. Ferroelectr. Freq. Control., **39**(3), 441–446 (1992).

[168] E. Larose, L. Margerin, B. A. van Tiggelen, and M. Campillo, Weak localization of seismic waves, Phys. Rev. Lett., **93**, 048501 (2004).

[169] D. McGloin and K. Dholakia, Bessel beams: Diffraction in a new light, Contemp. Phys., **46**(1), 15–28 (2005).

[170] M. Duocastella and C. B. Arnold, Bessel and annular beams for materials processing, Laser Photon. Rev., **6**(5), 607–621 (2012).

[171] P. Polesana, A. Couairon, D. Faccio, A. Parola, M. A. Porras, A. Dubietis, A. Piskarskas, and P. Di Trapani, Observation of conical waves in focusing, dispersive, and dissipative Kerr media, Phys. Rev. Lett., **99**, 223902 (2007).

[172] P. Polesana, M. Franco, A. Couairon, D. Faccio, and P. Di Trapani, Filamentation in Kerr media from pulsed Bessel beams, Phys. Rev. A, **77**, 043814 (2008).

[173] Z. Song, Z. Zhang, and T. Nakajima, Transverse-mode dependence of femtosecond filamentation, Opt. Express, **17**(15), 12217–12229 (2009).

[174] P. Polesana, A. Dubietis, M. A. Porras, E. Kučinskas, D. Faccio, A. Couairon, and P. Di Trapani, Near-field dynamics of ultrashort pulsed Bessel beams in media with Kerr nonlinearity, Phys. Rev. E, **73**, 056612 (2006).

[175] A. Dubietis, P. Polesana, G. Valiulis, A. Stabinis, P. Di Trapani, and A. Piskarskas, Axial emission and spectral broadening in self-focusing of femtosecond Bessel beams, Opt. Express, **15**(7), 4168–4175 (2007).

[176] I. Blonskyi, V. Kadan, I. Dmitruk, and P. Korenyuk, Cherenkov phase-matching in Raman-seeded four-wave mixing by a femtosecond Bessel beam, Appl. Phys. B, **107**(3), 649–652 (2012).

[177] K. Dota, A. Pathak, J. A. Dharmadhikari, D. Mathur, and A. K. Dharmadhikari, Femtosecond laser filamentation in condensed media with Bessel beams, Phys. Rev. A, **86**, 023808 (2012).

[178] D. Faccio, A. Averchi, A. Couairon, A. Dubietis, R. Piskarskas, A. Matijosius, F. Bragheri, M. A. Porras, A. Piskarskas, and P. Di Trapani, Competition between phase-matching and stationarity in Kerr-driven optical pulse filamentation, Phys. Rev. E, **74**, 047603 (2006).

[179] S. P. Tewari, H. Huang, and R. W. Boyd, Theory of self-phase-matching, Phys. Rev. A, **51**, R2707–R2710 (1995).

[180] M. A. Porras, A. Parola, D. Faccio, A. Dubietis, and P. Di Trapani, Nonlinear unbalanced Bessel beams: Stationary conical waves supported by nonlinear losses, Phys. Rev. Lett., **93**, 153902 (2004).

[181] U. Megerle, I. Pugliesi, C. Schiever, C. F. Sailer, and E. Riedle, Sub-50 fs broadband absorption spectroscopy with tunable exitation: putting the analysis of ultrafast molecular dinamics on solid, Appl. Phys. B., **96**(2-3), 215–231 (2009).

[182] P. Béjot, J. Kasparian, E. Salmon, R. Ackermann, N. Gisin, and J.-P. Wolf, Laser noise reduction in air, Appl. Phys. Lett., **88**(25), 251112 (2006).

[183] E. Schmidt, L. Knöll, D.-G. Welsch, M. Zielonka, F. König, and A. Sizmann, Enhanced quantum correlations in bound higher-order solitons, Phys. Rev. Lett., **85**, 3801–3804 (2000).

[184] D. Brida, C. Manzoni, G. Cirmi, M. Marangoni, S. Bonora, P. Villoresi, S. De Silvestri, and G. Cerullo, Few-optical-cycle pulses tunable from the visible to the mid-infrared by optical parametric amplifiers, J. Opt., **12**(1), 013001 (2010).

[185] J. Biegert, P.K. Bates, and O. Chalus, New mid-infrared light sources, IEEE J. Sel. Top. Quant. Electron., **18**(1), 531–540 (2012).

[186] J. Kasparian, R. Sauerbrey, D. Mondelain, S. Niedermeier, J. Yu, J.-P. Wolf, Y.-B. André, M. Franco, B. Prade, S. Tzortzakis, A. Mysyrowicz, M. Rodriguez, H. Wille, and L. Wöste, Infrared extension of the super continuum generated by femtosecond terawatt laser pulses propagating in the atmosphere, Opt. Lett., **25**(18), 1397–1399 (2000).

[187] Y. Chen, F. Théberge, C. Marceau, H. Xu, N. Aközbek, O. Kosareva, and S.L Chin, Observation of filamentation-induced continuous self-frequency down shift in air, Appl. Phys. B, **91**(2), 219–222 (2008).

[188] P. Lassonde, F. Théberge, S. Payeur, M. Châteauneuf, J. Dubois, and J.-C. Kieffer, Infrared generation by filamentation in air of a spectrally shaped laser beam, Opt. Express, **19**(15), 14093–14098 (2011).

[189] I. Ahmad, L. Bergé, Zs. Major, F. Krausz, S. Karsch, and S. A. Trushin, Redshift of few-cycle infrared pulses in the filamentation regime, New J. Phys., **13**(9), 093005 (2011).

[190] F. Théberge, P. Lassonde, S. Payeur, M. Châteauneuf, J. Dubois, and J.-C. Kieffer, Efficient spectral-step expansion of a filamenting laser pulse, Opt. Lett., **38**(9), 1576–1578 (2013).

[191] M. Ghotbi, V. Petrov, and F. Noack, Broadly tunable, sub-30 fs near-infrared pulses from an optical parametric amplifier based on BiB3O6, Opt. Lett., **35**(13), 2139–2141 (2010).

[192] O. Isaienko, E. Borguet, and P. Vöhringer, High-repetition-rate near-infrared noncollinear ultrabroadband optical parametric amplification in KTiOPO4, Opt. Lett., **35**(22), 3832–3834 (2010).

[193] G. Andriukaitis, T. Balčiūnas, S. Ališauskas, A. Pugžlys, A. Baltuška, T. Popmintchev, M.-C. Chen, M. M. Murnane, and H. C. Kapteyn, 90 GW peak power few-cycle mid-infrared pulses from an optical parametric amplifier, Opt. Lett., **36**(15), 2755–2757 (2011).

[194] M. Bass, C. DeCusatis, J. Enoch, V. Lakshminarayanan, G. Li, C. MacDonald, V. Mahajan, and E. Van Stryland, Handbook of Optics, volume 4, McGraw-Hill, New York, 3 edition (2009).

[195] A. A. Dergachev, V. N. Kadan, and S. A. Shlenov, Interaction of noncollinear femtosecond laser filaments in sapphire, Quant. Electron., **42**(2), 125 (2012).

[196] J. Shan, F. Wang, E. Knoesel, M. Bonn, and T. F. Heinz, Measurement of the frequency-dependent conductivity in sapphire, Phys. Rev. Lett., **90**, 247401 (2003).

[197] P. Chernev and V. Petrov, Self-focusing of light pulses in the presence of normal group-velocity dispersion, Opt. Lett., **17**(3), 172–174 (1992).

[198] J.-P. Bérubé, R. Vallée, M. Bernier, O. Kosareva, N. Panov, V. Kandidov, and S. L. Chin, Self and forced periodic arrangement of multiple filaments in glass, Opt. Express, **18**(3), 1801–1819 (2010).

[199] N.T. Nguyen, A. Saliminia, S.L. Chin, and R. Vallée, Control of femtosecond laser written waveguides in silica glass, Appl. Phys. B, **85**(1), 145–148 (2006).

[200] L. Guyon, F. Courvoisier, V. Boutou, R. Nuter, A. Vinçotte, S. Champeaux, L. Bergé, P. Glorieux, and J.-P. Wolf, Self-organized bundle of lasing filaments in dense media, Phys. Rev. A, **73**, 051802 (2006).

[201] L. Guyon, K.M. Hajek, F. Courvoisier, V. Boutou, R. Nuter, A. Vinçotte, S. Champeaux, L. Bergé, and J.-P. Wolf, Control of lasing filament arrays in nonlinear liquid media, Appl. Phys. B, **90**(3-4), 383–390 (2008).

[202] L. Bergé, S. Skupin, F. Lederer, G. Méjean, J. Yu, J. Kasparian, E. Salmon, J. P. Wolf, M. Rodriguez, L. Wöste, R. Bourayou, and R. Sauerbrey, Multiple filamentation of terawatt laser pulses in air, Phys. Rev. Lett., **92**, 225002 (2004).

[203] S. A. Hosseini, Q. Luo, B. Ferland, W. Liu, S. L. Chin, O. G. Kosareva, N. A. Panov, N. Aközbek, and V. P. Kandidov, Competition of multiple filaments during the propagation of intense femtosecond laser pulses, Phys. Rev. A, **70**, 033802 (2004).

[204] S. Skupin, L. Bergé, U. Peschel, F. Lederer, G. Méjean, J. Yu, J. Kasparian, E. Salmon, J. P. Wolf, M. Rodriguez, L. Wöste, R. Bourayou, and R. Sauerbrey, Filamentation of femtosecond light pulses in the air: Turbulent cells versus long-range clusters, Phys. Rev. E, **70**, 046602 (2004).

[205] K. Cook, A. K. Kar, and R. A. Lamb, White-light supercontinuum interference of self-focused filaments in water, Appl. Phys. Lett., **83**(19), 3861–3863 (2003).

[206] D. Faccio, A. Dubietis, G. Tamosauskas, P. Polesana, G. Valiulis, A. Piskarskas, A. Lotti, A. Couairon, and P. Di Trapani, Phase- and group-matched nonlinear interactions mediated by multiple filamentation in Kerr media, Phys. Rev. A, **76**, 055802 (2007).

[207] O.G. Kosareva, T. Nguyen, N.A. Panov, W. Liu, A. Saliminia, V.P. Kandidov, N. Akozbek, M. Scalora, R. Vallee, and S.L. Chin, Array of femtosecond plasma channels in fused silica, Opt. Commun., **267**(2), 511 – 523 (2006).

[208] M. Châeauneuf, S. Payeur, J. Dubois, and J.-C. Kieffer, Microwave guiding in air by a cylindrical filament array waveguide, Appl. Phys. Lett., **92**(9), 091104 (2008).

[209] G. Méchain, A. Couairon, M. Franco, B. Prade, and A. Mysyrowicz, Organizing multiple femtosecond filaments in air, Phys. Rev. Lett., **93**, 035003 (2004).

[210] H. Schroeder, J. Liu, and S. Chin, From random to controlled small-scale filamentation in water, Opt. Express, **12**(20), 4768–4774 (2004).

[211] Z. Jin, J. Zhang, M. H. Xu, X. Lu, Y. T. Li, Z. H. Wang, Z. Y. Wei, X. H. Yuan, and W. Yu, Control of filamentation induced by femtosecond laser pulses propagating in air, Opt. Express, **13**(25), 10424–10430 (2005).

[212] J. Liu, H. Schroeder, S. L. Chin, R. Li, and Z. Xu, Ultrafast control of multiple filamentation by ultrafast laser pulses, Appl. Phys. Lett., **87**(16), 161105 (2005).

[213] V.P. Kandidov, N. Akozbek, M. Scalora, O.G. Kosareva, A.V. Nyakk, Q. Luo, S.A. Hosseini, and S.L. Chin, Towards a control of multiple filamentation by spatial regularization of a high-power femtosecond laser pulse, Appl. Phys. B, **80**(2), 267–275 (2005).

[214] T. Pfeifer, L. Gallmann, M. J. Abel, D. M. Neumark, and S. R. Leone, Circular phase mask for control and stabilization of single optical filaments, Opt. Lett., **31**(15), 2326–2328 (2006).

[215] A. Trisorio and C. P. Hauri, Control and characterization of multiple circularly polarized femtosecond filaments in argon, Opt. Lett., **32**(12), 1650–1652 (2007).

[216] C.P. Hauri, J. Gautier, A. Trisorio, E. Papalazarou, and P. Zeitoun, Two-dimensional organization of a large number of stationary optical filaments by adaptive wave front control, Appl. Phys. B, **90**(3-4), 391–394 (2008).

[217] P. Rohwetter, M. Queißer, K. Stelmaszczyk, M. Fechner, and L. Wöste, Laser multiple filamentation control in air using a smooth phase mask, Phys. Rev. A, **77**, 013812 (2008).

[218] Z.Q. Hao, R. Salamé, N. Lascoux, E. Salmon, P. Maioli, J. Kasparian, and J.-P. Wolf, Multiple filamentation of non-uniformly focused ultrashort laser pulses, Appl. Phys. B, **94**(2), 243–247 (2009).

[219] A. Dubietis, G. Tamošauskas, P. Polesana, G. Valiulis, H. Valtna, D. Faccio, P. Di Trapani, and A. Piskarskas, Highly efficient four-wave parametric amplification in transparent bulk Kerr medium, Opt. Express, **15**(18), 11126–11132 (2007).

[220] A. Dubietis, G. Tamošauskas, G. Fibich, and B. Ilan, Multiple filamentation induced by input-beam ellipticity, Opt. Lett., **29**(10), 1126–1128 (2004).

[221] M. Centurion, Y. Pu, and D. Psaltis, Self-organization of spatial solitons, Opt. Express, **13**(16), 6202–6211 (2005).

[222] T. Grow and A. Gaeta, Dependence of multiple filamentation on beam ellipticity, Opt. Express, **13**(12), 4594–4599 (2005).

[223] V. Kudriasov, E. Gaizauskas, and V. Sirutkaitis, Beam transformation and permanent modification in fused silica induced by femtosecond filaments, J. Opt. Soc. Am. B, **22**(12), 2619–2627 (2005).

[224] A. Dubietis, E. Kucinskas, and G. Tamosauskas, Formation of periodic multifilamentary structures by use of highly elliptic light beams, Lith. J. Phys., **47**, 27 (2007).

[225] G. Fibich, S. Eisenmann, B. Ilan, and A. Zigler, Control of multiple filamentation in air, Opt. Lett., **29**(15), 1772–1774 (2004).

[226] G. Fibich, S. Eisenmann, B. Ilan, Y. Erlich, M. Fraenkel, Z. Henis, A. Gaeta, and A. Zigler, Self-focusing distance of very high power laser pulses, Opt. Express, **13**(15), 5897–5903 (2005).

[227] N. Gavish, G. Fibich, L. T. Vuong, and A. L. Gaeta, Predicting the filamentation of high-power beams and pulses without numerical integration: A nonlinear geometrical optics method, Phys. Rev. A, **78**, 043807 (2008).

[228] R. Malendevich, L. Jankovic, G. Stegeman, and J. S. Aitchison, Spatial modulation instability in a Kerr slab waveguide, Opt. Lett., **26**(23), 1879–1881 (2001).

[229] I. H. Malitson, Interspecimen comparison of the refractive index of fused silica, J. Opt. Soc. Am., **55**(10), 1205–1208 (1965).

[230] D. Milam, Review and assessment of measured values of the nonlinear refractive-index coefficient of fused silica, Appl. Opt., **37**(3), 546–550 (1998).

[231] D. Majus, V. Jukna, G. Valiulis, and A. Dubietis, Generation of periodic filament arrays by self-focusing of highly elliptical ultrashort pulsed laser beams, Phys. Rev. A, **79**, 033843 (2009).

[232] M. Mlejnek, M. Kolesik, J. V. Moloney, and E. M. Wright, Optically turbulent femtosecond light guide in air, Phys. Rev. Lett., **83**, 2938–2941 (1999).

[233] A. Picozzi and M. Haelterman, Hidden coherence along space-time trajectories in parametric wave mixing, Phys. Rev. Lett., **88**, 083901 (2002).

[234] O. Jedrkiewicz, A. Picozzi, M. Clerici, D. Faccio, and P. Di Trapani, Emergence of X-shaped spatiotemporal coherence in optical waves, Phys. Rev. Lett., **97**, 243903 (2006).

[235] O. Jedrkiewicz, M. Clerici, A. Picozzi, D. Faccio, and P. Di Trapani, X-shaped space-time coherence in optical parametric generation, Phys. Rev. A, **76**, 033823 (2007).

[236] I. Blonskyi, V. Kadan, O. Shpotyuk, and I. Dmitruk, Manifestations of sub- and superluminality in filamented femtosecond laser pulse in fused silica, Opt. Commun., **282**(9), 1913 – 1917 (2009).

[237] A. Saliminia, N. T. Nguyen, S. L. Chin, and R. Vallée, Densification of silica glass induced by 0.8 and 1.5 μm intense femtosecond laser pulses, J. Appl. Phys., **99**(9), 093104 (2006).